LONDON'S GLOBAL UNIVERSITY

Investigation of highly selective metal-oxide photocatalysts for glycerol oxidation into value-added chemicals

Lunqiao Xiong

2023.03

A thesis submitted of the partial fulfilment of the requirements for the degree of Doctor of Philosophy at University College London

Department of Chemical Engineering,
University College London,
Torrington Place,
London,
WC1E 7JE

Declaration

I, Lunqiao Xiong, confirm that the work presented in this thesis is my own. Where information has been derived from other sources, I confirm that this has been indicated in the thesis.

Signature:

Date:

I. Acknowledgement

I would like to express my deepest gratitude to my supervisor, Prof. Junwang Tang, for his unwavering support and kindness throughout the 4.5 years of my research project (which was extended by six months due to the Covid-19 pandemic). During the challenging and uncertain times of my research, his timely guidance, insightful vision, and unrelenting determination provided me with the motivation and strength to overcome obstacles. I have gained a wealth of knowledge from him and hope to continue in the future.

I would like to extend special thanks to Prof. Aiqin Wang, my supervisor during my visit to the Dalian Institute of Chemical Physics (DICP). Her dedication to the pursuit of truth, exacting standards for research, and kindness toward students inspired me to continue exploring the frontiers of science and become a better researcher. Additionally, I would like to express my gratitude to Prof. Stefan Guldin for his care, assistance and valuable suggestions that greatly facilitated my research endeavours.

Huge thanks must go to Dr. Leilei Zhang, my tutor in research and companion in life. His insightful ideas, extensive knowledge, and invaluable suggestions have provided me with boundless inspiration. I would also like to thank Dr. Ji Yang, Dr. Jiajia Shi, Dr. Yue Zhang for their support and assistance when I was just joining DICP and kept doing so until they graduated there. Additionally, I would like to extend my appreciation to Prof. Xiaoyan Liu, Dr. Haifeng Qi, Dr. Fei Liu, Ms. Hua Wang, Ms. Xiaoli Pan, Mr. Tingpeng Wang, Mr. Shengxin Zhang, Mr. Yang Su, Mr. Zhounan Yu, Mr. Yuanlong Tan, Ms. Yanan Xing, and Mr. Xingchi Li for their patient discussions and contributions

to XAS, PL, TPD, HPLC, TG, FTIR, and TEM characterisations. I am also grateful to Prof. Xiuli Wang and Ms. Lingcong Zhang for their expertise and contribution to the discussion of ultrafast time-resolved spectroscopies. Thanks to Dr. Guangyi Li, Mr. Fan Bai and Dr. WeiXiang Guan, our lab safety managers, for their diligent efforts in maintaining a clean and safe environment for us to work in on a daily basis.

I am grateful for the kindness of my colleagues in the UK: Dr. Chaoran Jiang, Dr. Qiushi Ruan, Dr. Jijia Xie, Dr. Yiou Wang, Dr. Dan Kong, Dr. Ayoola Shoneye, Dr. Deqiang Zhao, Dr. Hui Wang, Dr. Tina Miao, Dr. Xiyi Li, Mr. Qingning Yang, Mr. Haimiao Jiao, Mr. Chao Wang, Mr. Deyao Li, Mr. Zhe Yuan, Mr. Youxun Xu, Mr. Enqi Chen, Dr. Kiran Vankayala, Dr. Christopher Windle, Dr. Madasamy Thangamuthu and all the others who were not mentioned. Their support and generosity have been invaluable to me over the years.

I am also grateful to my colleagues in my group at DICP: Dr. Shanshan Niu, Dr. Dan Zhou, Mr. An Wang, Mr. Huan Chen, Ms. Chen Cao, Mr. Yichao Wang, Mr. Zhitong Zhou, Ms. Rizheng Jing, Ms. Anqi Li, Mr. Jichao Zhang, Mr. Hongchen Cao, Ms. Haozhen Wang. Their help and camaraderie made my time there unforgettable, and I will always cherish those memorable days.

I would like to extend a special acknowledgment to the Engineering and Physical Sciences Research Council (EPSRC) for providing funding for my PhD. Lastly, I would like to express my heartfelt appreciation to my family, including my mother, father, and girlfriend Dr. Fan Huang, who have supported me unwaveringly through both the highs and lows of my journey. Without their encouragement and belief in me, I would not have come this far.

II. Abstract

Glycerol is an important by-product in biodiesel production and is produced in large quantities, resulting in a huge surplus flooding the market with a very low price (US $0.11 per kg). It is also a highly versatile polyol which can be transformed into a plethora of different value-added chemicals. Despite many research efforts devoted to finding active catalysts to transform glycerol into valuable products, it remains a significant challenge to develop an efficient and highly selective catalyst for the transformation of glycerol into a specific product. Therefore, glycerol transformation is not only of great scientific significance but also of economic interest. Photocatalysis has been recognised as a promising strategy in glycerol conversion under very mild conditions. However, one barrier is that most semiconductor-based photocatalysts are either non-selective (particularly with the presence of water and/or oxygen) or ineffective to activate the C-C or C-O bond because of poor oxidative activity.

To address the above issues, a highly selective catalyst was first synthesised for the transformation of glycerol to the high-value product glycolaldehyde, which is composed of nickel single atoms confined on titanium dioxide. Driven by light, the catalyst operates under ambient conditions using air as a green oxidant. The optimised catalyst shows a selectivity of over 60% to glycolaldehyde, resulting in a 1.06 $mmol \cdot g^{-1} \cdot h^{-1}$ production rate, and nearly 3 times higher turnover number than NiO_x nanoparticle-decorated TiO_2 photocatalyst. Diverse *operando* and *in-situ* spectroscopies unveil the unique function of the Ni single atoms, which can significantly promote oxygen adsorption, work as an electron sink and accelerate the production of

superoxide radicals, thereby improving the selectivity towards glycolaldehyde over other by-products.

Next a two-step co-catalyst modification strategy was applied by loading Au and Ag onto ZnO to significantly promote charge separation/transport, meanwhile generating H_2O_2 and glyceraldehyde simultaneously. Under light irradiation, the optimised catalyst shows a very high glyceraldehyde yield of 3.86 $mmol \cdot g^{-1} \cdot h^{-1}$, nearly 6 times higher than ZnO, with a remarkable 75% selectivity to glyceraldehyde. Furthermore, H_2O_2 yield reaches 4.64 $mmol \cdot g^{-1} \cdot h^{-1}$, 13 times higher than pristine ZnO, leading to a record AQY of 25%. Spectroscopic results and structure analysis unveil that AuAg alloy can effectively act as hole acceptors, improving the charge transfer and facilitating glycerol oxidation. $O_2^{\bullet -}$ radicals are facilely formed over Ag single atoms supported ZnO by photogenerated electrons and further reduced to H_2O_2. In addition, Ag single atoms over the ZnO surface can prevent the H_2O_2 decomposition and thus significantly enhance the H_2O_2 selectivity. As a result, nearly 100% atom economy and high charge utilisation have been achieved.

Finally, two valuable trioses, glyceraldehyde and dihydroxyacetone, are converted from glycerol over $Cu^{\delta+}$-decorated WO_3 photocatalyst with a five-fold enhancement in conversion (14.52 $mmol \cdot g^{-1}$) and a selectivity of 84%. *In-situ* spectroscopies and isotopic analysis confirm the function of Cu^+ species, which efficiently serve as hole acceptors, enhancing charge transfer which in turn improving the photocatalytic activity. Moreover, it is found that the glycerol oxidation over $Cu^{\delta+}$-decorated WO_3 is initiated by the photogenerated holes, followed by coupling with •OH radicals, and finally dehydrated into the target products.

III. Impact Statement

Light-driven organic synthesis under mild conditions is a promising route to upgrade biowastes (e.g., glycerol) and alleviate environmental issues. The development of novel photocatalysts to selectively and efficiently convert these biowastes into valuable chemicals is of great scientific significance and the key to realising profitable applications.

Herein, I have successfully synthesised single-atom-loaded TiO_2 photocatalysts which can highly selectively and efficiently convert glycerol into value-added glycolaldehyde under light irradiation and mild conditions. Through a two-step co-catalyst modification strategy, I realised the simultaneous generation of H_2O_2 and glyceraldehyde over ZnO photocatalyst, achieving nearly 100% atom economy and high charge utilisation. Extending the operating conditions to the visible region represents another achievement in this work, which significantly improves the utilisation efficiency of solar energy. Such discovery, as well as the verified reaction routes, would contribute to the sustainable conversion of biowastes and the mitigation of environmental issues to some extent. Moreover, the unique function of the loaded single atoms has been systematically investigated in this work, which provides insights into heterogeneous single-atom photocatalysis. Meanwhile, these strategies could be extended to the design of photocatalysts for other organic synthesises. Beyond that, the fundamental understanding of single-atom photocatalysts will benefit the research in metal oxide semiconductors, catalysis, organic synthesis, and environmental purification.

IV. Publications and Conferences

i. Publication

(1) **Xiong, L.**; Qi, H.; Zhang, S.; Zhang, L.; Liu, X.; Wang, A.; Tang, J. Highly selective transformation of biomass derivatives to valuable chemicals by single-atom photocatalyst Ni/TiO2. *Advanced Materials* **2023**, *n/a* (n/a), 2209646, https://doi.org/10.1002/adma.202209646.

(2) **Xiong, L.**; Tang, J. Strategies and Challenges on Selectivity of Photocatalytic Oxidation of Organic Substances. *Adv. Energy Mater.* **2021**, *11* (8), 2003216, https://doi.org/10.1002/aenm.202003216.

(3) **Xiong, L.**, Yu, Z., Cao, H., Guan, W., Su, Y., Zhang, L., Liu, X., Wang, A., Tang, J. Converting Glycerol into Valuable Trioses by $Cu^{\delta+}$-Decorated WO_3 under Visible Light. (*Under preparation*)

(4) **Xiong, L.**, Yu, Z., Zhang, L., Jiang, Q., Wang, X., Zhang, L., Liu, X., Wang, A., Tang, J. Multifunction of Ag-Single-Atom Decorated Au/ZnO for Glycerol to Glyceraldehyde and Hydrogen Peroxide. (*Under preparation*)

(5) An, X.; Wei, T.; Ding, P.; Liu, L.-M.; **Xiong, L.**; Tang, J.; Ma, J.; Wang, F.; Liu, H.; Qu, J. Sodium-Directed Photon-Induced Assembly Strategy for Preparing Multisite Catalysts with High Atomic Utilization Efficiency. *Journal of the American Chemical Society* **2023**, *145* (3), 1759-1768. DOI: 10.1021/jacs.2c10690.

(6) Jiao, H.; Wang, C.; **Xiong, L.**; Tang, J. Insights on Carbon Neutrality by Photocatalytic Conversion of Small Molecules into Value-Added Chemicals or

Fuels. *Accounts of Materials Research* **2022**. DOI: 10.1021/accountsmr.2c00095.

(7) Miao, T. J.; Wang, C.; **Xiong, L.**; Li, X.; Xie, J.; Tang, J. In Situ Investigation of Charge Performance in Anatase TiO2 Powder for Methane Conversion by Vis–NIR Spectroscopy. *ACS Catal.* **2021**, *11* (13), 8226-8238. DOI: 10.1021/acscatal.1c01998.

(8) Luo, L.; Wang, K.; Gong, Z.; Zhu, H.; Ma, J.; **Xiong, L.**; Tang, J. Bridging-nitrogen defects modified graphitic carbon nitride nanosheet for boosted photocatalytic hydrogen production. *Int J Hydrogen Energ* **2021**, *46* (53), 27014-27025. DOI: https://doi.org/10.1016/j.ijhydene.2021.05.197.

(9) Luo, L.; Gong, Z.; Ma, J.; Wang, K.; Zhu, H.; Li, K.; **Xiong, L.**; Guo, X.; Tang, J. Ultrathin sulfur-doped holey carbon nitride nanosheets with superior photocatalytic hydrogen production from water. *Applied Catalysis B: Environmental* **2021**, *284*, 119742. DOI: https://doi.org/10.1016/j.apcatb.2020.119742.

(10) Li, J.; **Xiong, L.**; Luo, B.; Jing, D.; Cao, J.; Tang, J. Hollow carbon spheres-modified graphitic carbon nitride for efficient photocatalytic H2 production. *Chemistry – A European Journal* **2021**, *n/a* (n/a), https://doi.org/10.1002/chem.202102330.

(11) Gu, Z.; An, X.; Liu, R.; **Xiong, L.**; Tang, J.; Hu, C.; Liu, H.; Qu, J. Interface-modulated nanojunction and microfluidic platform for photoelectrocatalytic chemicals upgrading. *Applied Catalysis B: Environmental* **2021**, *282*, 119541. DOI: https://doi.org/10.1016/j.apcatb.2020.119541.

(12) Bayazit, M. K.; **Xiong, L.**; Jiang, C.; Moniz, S. J. A.; White, E.; Shaffer, M. S. P.; Tang, J. Defect-Free Single-Layer Graphene by 10 s Microwave Solid Exfoliation and Its Application for Catalytic Water Splitting. *ACS Applied Materials & Interfaces* **2021**. DOI: 10.1021/acsami.1c03906.

(13) Zhang, W.; Ma, J.; **Xiong, L.**; Jiang, H.-Y.; Tang, J. Well-Crystallized α-FeOOH Cocatalysts Modified BiVO4 Photoanodes for Efficient and Stable Photoelectrochemical Water Splitting. *ACS Applied Energy Materials* **2020**, *3* (6), 5927-5936. DOI: 10.1021/acsaem.0c00834.

(14) Windle, C. D.; Wieczorek, A.; **Xiong, L.**; Sachs, M.; Bozal-Ginesta, C.; Cha, H.; Cockcroft, J. K.; Durrant, J.; Tang, J. Covalent grafting of molecular catalysts on C3NxHy as robust, efficient and well-defined photocatalysts for solar fuel synthesis. *Chemical Science* **2020**, 10.1039/D0SC02986F. DOI: 10.1039/D0SC02986F.

(15) Li, C.-B.; Chu, Y.; Xie, P.; **Xiong, L.**; Wang, N.; Wang, H.; Tang, J. Molecular Cobalt Catalysts Grafted onto Polymers for Efficient Hydrogen Generation Cathodes. *Solar RRL* **2020**, *n/a* (n/a). DOI: 10.1002/solr.202000281 (acccessed 2020/08/04).

(16) Jiang, C.; Yang, J.; Zhao, T.; **Xiong, L.**; Guo, Z.-X.; Ren, Y.; Qi, H.; Wang, A.; Tang, J. Co3+-O-V4+ cluster in CoVOx nanorods for efficient and stable electrochemical oxygen evolution. *Applied Catalysis B: Environmental* **2020**, 119571. DOI: https://doi.org/10.1016/j.apcatb.2020.119571.

(17) Han, Q.; Jiao, H.; **Xiong, L.**; Tang, J. Progress and challenges in photocatalytic ammonia synthesis. *Materials Advances* **2020**. DOI: 10.1039/D0MA00590H.

ii) Conferences

(1) Double Carbon Youth Forum by Youth Promotion Association, Dalian, China, Jul. 2022

(2) Joint UK Solar Fuels Network-SuperSolar workshop on Solar Energy Conversion and Storage, London, UK, Dec. 2019

V. Table of Contents

VI. List of Figures

VII. List of Tables

VIII. Nomenclature

Acronyms & initialisms

AC	aberration-corrected
AQY	apparent quantum yield
CB	conduction band
CN	carbon nitride
CNT	carbon nanotube
COF	covalent organic framework
DFT	density functional theory
DI	deionised
DMPO	5,5-dimethyl-1pyrroline-N-oxide
EDX	energy dispersive X-ray spectroscopy
E_f	Fermi level
EPR	electron paramagnetic resonance
ESR	electron spin resonance
EXAFS	extended X-ray absorption fine structure
GC	gas chromatographs
GC-MS	gas chromatographs-mass spectrometry
HAADF	high-angle annual dark-filed
HOMO	highest occupied molecular orbital
ICP-AES	inductively coupled plasma atomic emission spectrometry
IPA	isopropyl alcohol
LMCT	ligand-to-metal charge transfer
LUMO	lowest unoccupied molecular orbital
MOF	metal-organic framework
NHE	normal hydrogen electrode
NP	nanoparticle
OV	oxygen vacancy
rGO	reduced graphene oxide
ROS	reactive oxygen species
SAC	single atom catalyst
SCE	saturated calomel electrode
SEM	scanning electron microscopy
SHE	standard hydrogen electrode
SOD	superoxide dismutase
SP	surface plasmon
SPR	surface plasmon resonance
STEM	scanning transmission electron microscopy
TEM	transmission electron microscopy
TEMP	2,2,6,6-tetramethylpiperidine
TEOA	triethanolamine
TPD	temperature-programmed desorption
UV-Vis	ultraviolet-visible spectroscopy
VB	valence band
XAS	X-ray absorption spectra
XANES	X-ray absorption near-edge structure

XPS	X-ray photoelectron spectroscopy
XRD	X-ray diffraction

1. Introduction

1.1 Background

Since 1828, the year when urea was first synthesised from inorganic ammonium cyanate, organic synthesis has entered the historical arena, gradually forming an important cornerstone in human life.(*3*) Upon nearly 200 years investigation and practice, most of organic chemicals are still synthesised under relatively harsh conditions, eg. high temperature and pressure, also generating large amount of hazardous by-products. In 1990's, with a consensus on the consequences of chemical pollution and increasing resource demand, "green chemistry" was proposed to minimize the use or generation of hazardous substances. Along with more stringent environmental policies, chemical industry has to upgrade traditional processes to "greener" synthesis routes.

Actually, an idea to address this issue has already been put forward by Giacomo Ciamician in *Science* in 1912: using photochemical process to produce value-added organic chemicals.(*4*) He predicted that abundant, renewable solar energy and mild reaction environment would replace harmful reagents and harsh conditions in organic synthesis. This idea was not brought to fruition until the discovery of Honda−Fujishima effect in 1972.(*5*) Titanium dioxide, in the form of thin film or nanoparticles, was found to simultaneously generate electrons and holes under light irradiation, thereafter taking part in a series of redox reactions. Since then heterogeneous photocatalysis by semiconducting materials has drawn tremendous attention and been extensively studied for water splitting(*6, 7*), CO_2 reduction(*8*), environmental

remediation(*9, 10*) and organic synthesis(*11*). In contrast to conventional thermal catalysis, both spontaneous reactions (Gibbs free energy difference $\Delta G_0 < 0$) and non-spontaneous reactions ($\Delta G_0 > 0$) can be initiated by photocatalysts. In spontaneous reactions, photocatalysts utilise light energy to overcome activation barrier, facilitating reactions at an increased rate or under mild conditions. In non-spontaneous reactions, part of the light energy is transferred into the reaction products, storing as chemical energy.

The conception of photocatalysis was first widely applied to environmental purification because a series of photocatalysts could easily decompose various kinds of organic pollutants into water and CO_2 (mineralisation) with light irradiation under benign conditions. As for organic synthesis, despite the feasibility has been proved and great efforts have been made(*12-16*), most semiconductor-involved photocatalytic organic reactions are usually non-selective process, especially in aqueous media.(*11*) To improve selectivity in photocatalytic organic synthesis as a “greener” alternative to energy intensive and environmentally hazardous methods is therefore most sought after.

Behind polymerization, selective oxidation is the second largest industrial process, contributing to ~30% of total production in modern chemical industry.(*17*) Selective oxidation reactions thus play a vital role in organic synthesis and have drawn particular attention. Numerous compounds and intermediates like alcohols, epoxides, aldehydes, ketones, and organic acids, can be prepared by selective oxidation reactions.

Glycerol has many derivatives because of its three OH groups, thus it can be oxidatively transformed into various value-added chemicals and products.

As the dramatically increased production of biodiesel, its by-product glycerol is also produced in large quantities, resulting in a huge surplus flooding the market at a low price. Although many efforts have been devoted to this area, it still remains a great challenge to find active catalysts to transform glycerol into specific products. Therefore, glycerol oxidative transformation is not only of great scientific significance but also a very profitable route to utilise this biowaste.

1.2 Motivation, aim and objectives

As discussed above, selectively converting glycerol into specific value-added chemicals under light irradiation and mild conditions provides a promising route to utilise this biowaste. More importantly, this reaction could be studied as a model reaction, based on which the underlying mechanism of photocatalysis could be revealed and more synthesis routes could be realised. Driven by this, photocatalysts with improved activity and controllable selectivity must be developed.

Metal oxide photocatalysts provide an ideal platform for such reactions due to their superior activity, robust structure, and stable performance. However, considering the high recombination rate of charge carriers in metal oxide photocatalysts, and usually weak adsorption ability to reactants, the modification by loading metal cocatalysts is a critical strategy to improve their photocatalytic performance. Currently, the role of metal nanoparticles that are frequently applied as cocatalysts remains unclear and sometimes controversial due to the involvement of complex factors. Single-atom cocatalysts have offered new opportunities to address the above challenges benefitting from their

uniform geometrical/electronic structure, exotic properties, and maximum atom-utilization efficiency. I am to develop a strategy to effectively load metal cocatalysts, making them atomically dispersed over the substrate photocatalysts. By introducing these single atoms, the formed photocatalysts should selectively convert glycerol into value-added chemicals with high efficiency. Further, I plan to investigate the effects of these single atoms on the charge transfer and adsorption/desorption abilities of photocatalysts. The reaction routes should also be clarified to provide an insightful understanding of photocatalytic organic synthesis.

The key objectives include 1) to develop photocatalysts for selective glycerol oxidation; 2) to systematically investigate the reaction mechanism over these photocatalysts; 3) to extend the glycerol conversion to the visible region, paving the way towards effective solar energy utilisation; 4) to reveal the precise role of the single atom cocatalysts.

1.3 Structure of the thesis

There will be seven chapters in this thesis, focusing on light-driven metal-oxide-based single atom photocatalysts for selective glycerol oxidation. In short, after a brief introduction of Chapter 1, Chapter 2 will review the mechanism of photocatalytic organic oxidation and the reactive oxygen species involved. Then the latest progress in the photocatalytic oxidation of organic compounds and the strategies to control the selectivity will be discussed. In Chapter 3, experiment methods of several characterisations in the following studies will be described. Afterwards, in Chapter 4, a single-atom photocatalyst Ni/TiO_2 will be presented, which can convert glycerol into glycolaldehyde with high selectivity

and turnover number. The mechanism behind such superior performance will be explored. In Chapter 5, I show another highly reactive and selective catalyst for the conversion of glycerol and oxygen to the high-value products glyceraldehyde and hydrogen peroxide simultaneously. Furthermore, following the performance tests, diverse *in-situ* spectroscopy and microscopy results will be discussed to reveal the charge transfer and reaction pathways. Extending the glycerol conversion into the visible region will be shown in Chapter 6, in which two valuable trioses, namely glyceraldehyde and dihydroxyacetone, are produced from glycerol over $Cu^{\delta+}$-decorated WO_3 photocatalyst. The last chapter (Chapter 7) will summarise the key conclusions and propose future work.

2. Literature survey

This project focuses on highly selective photocatalysts for glycerol oxidation into value-added chemicals. Therefore, the following only reviews the recent progress of semiconducting photocatalysts and their applications in selective oxidation of organic substances.

2.1 Heterogeneous oxidation by semiconductor photocatalysis

Typically, semiconductor-based photocatalysis is a process where semiconductors are activated by light, generating energetic electrons and holes to initiate oxidation and reduction reactions. In other words, the incident light with energy higher than the semiconducting bandgap could generate electrons and holes simultaneously, where the electrons can be excited to the conduction band (CB), leaving photoactivated holes in the valence band (VB). Generated electrons and holes could recombine, or immigrate to the surface of the catalyst, then initiating a variety of photoredox reactions. If photocatalysis is conducted in the presence of water under aerobic conditions, involving oxygen and/or water as reaction species, a series of reactive oxygen species (ROS), including superoxide radical ($O_2^{\bullet-}$), hydrogen peroxide (H_2O_2), hydroxyl radical (•OH) and singlet oxygen ($^1O_2$), could be generated from surrounding oxygen molecules, water, or OH groups attached on catalyst's surface. Together with the photogenerated holes, these oxygen species are the key compounds to initiate photocatalytic organic oxidations.

In the well-documented photocatalytic degradation, photoactivated holes and free radical species (especially •OH) are considered to be the main oxidants. They can mineralise organic compounds into CO_2 and water unselectively. Similarly, these strong oxidants are inevitably formed in aqueous media in organic synthesis processes, facilitating nonselective oxidation, and thus reducing the selectivity to the target products. Therefore, careful control on the formation of ROS is vital in selective photocatalytic organic synthesis and the formation processes of these ROS are firstly presented below.

2.2. Reactive oxygen species (ROS)

ROS are generated *via* the interaction of photoactivated charge carriers with the surrounding medium, the type of photocatalysts or a solvent used, therefore plays an important role in a photocatalytic system. Understanding the formation and properties of ROS provides clues to improve catalytic activity and selectivity as these species are the primary oxidants besides photogenerated holes in photooxidation reactions (**Figure 1**).(*18*)

2.2.1 Superoxide radical ($O_2^{\bullet-}$)

Semiconductors with a CB edge more negative than the potential of $O_2/O_2^{\bullet-}$ (sometimes denote O_2^-) could transfer photo-activated electrons to the π* orbitals of oxygen molecules, generating superoxide radicals (reaction 2-1). As a moderate oxidant, $O_2^{\bullet-}$ could either participant in or directly initiate selective oxidation of organic compounds. Moreover, relatively long survival time enables $O_2^{\bullet-}$ to migrate long distance in the reaction media, thus allowing the oxidation reaction taking place beyond the surface of the catalyst.(*19*) Nevertheless, excessive accumulation of $O_2^{\bullet-}$ could overoxidise organic molecules and finally

result in mineralisation.(*20*) In acidic media (pH < 4.8), $O_2^{\bullet-}$ could be easily protonated to hydroperoxyl radical ($^{\bullet}HO_2$) (reaction 2-2) and further disproportionated to H_2O_2 (reaction 2-3).

$$O_2 + e^-_{(CB)} \rightarrow O_2^{\bullet-} \ (E^0 = -0.33 \text{ V } \textit{vs.} \text{ SHE}) \qquad (2\text{-}1)$$

$$O_2^{\bullet-} + H^+ \rightarrow {}^{\bullet}OOH \ (E^0 = -0.046 \text{ V } \textit{vs.} \text{ SHE}) \qquad (2\text{-}2)$$

$$O_2^{\bullet-} + {}^{\bullet}OOH + H_2O \rightarrow H_2O_2 + O_2 + OH^- \qquad (2\text{-}3)$$

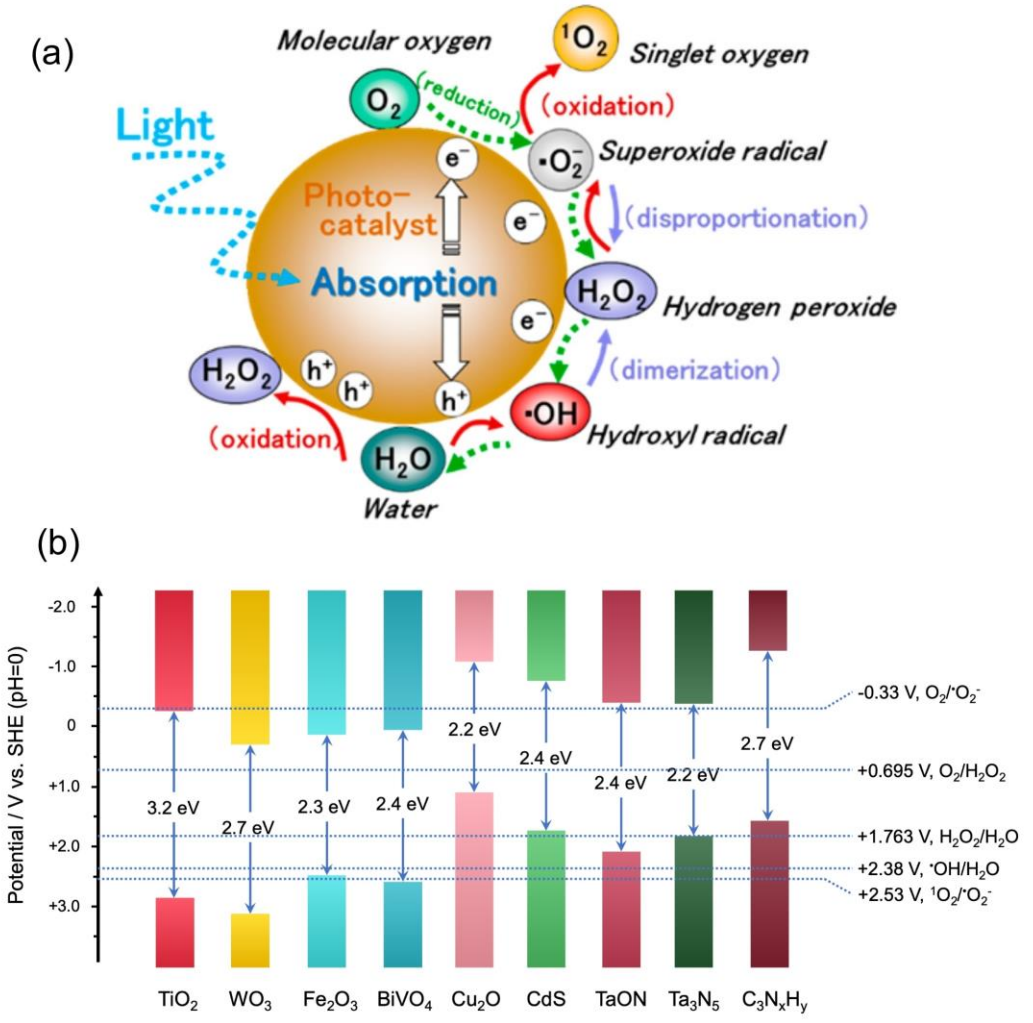

Figure 1. (**a**) Reactive oxygen species generated in the photocatalytic reduction of oxygen and oxidation of water.(*18*) Copyright (2017) American Chemical Society. (**b**) Redox potentials of reactive oxygen species and band edge positions of typical semiconductors for organic oxidation.

2.2.2 Hydrogen peroxide (H_2O_2)

If the conduction band of the semiconductor is not sufficient to reduce O_2 by a single-electron process, two-electron reduction is the only way to activate O_2 by forming H_2O_2 (reaction 2-4). In aqueous media, H_2O_2 could also be generated by two-hole oxidation from H_2O (reaction 2-5). As a stronger oxidant than oxygen, H_2O_2 can directly oxidise organic chemicals. Moreover, H_2O_2 could decompose into hydroxyl radicals (•OH) (reaction 2-6), which can activate strong bonds like unsaturated sp^2 C–H bonds of benzene, followed by the complete mineralisation.(*21*) Thus the decomposition of H_2O_2 is considered a key step in environmental remediation, whether H_2O_2 is added or *in-situ* generated. This also generates another challenge to manipulate the selectivity of the expected organic production.

$$O_2 + 2e^-_{(CB)} + 2H^+ \rightarrow H_2O_2 \ (E^0 = 0.695 \text{ V } \textit{vs.} \text{ SHE}) \qquad (2\text{-}4)$$

$$2H_2O + 2h^+_{(VB)} \rightarrow H_2O_2 + 2H^+ \ (E^0 = 1.763 \text{ V } \textit{vs.} \text{ SHE}) \qquad (2\text{-}5)$$

$$H_2O_2 \rightarrow 2\bullet OH \qquad (2\text{-}6)$$

2.2.3 Hydroxyl radicals (•OH)

With sufficient energy, photogenerated holes could oxidise adsorbed water or surface-attached hydroxyls into hydroxyl radicals (•OH) (reaction 2-7). Though the mechanistic implications are still unclear, •OH are widely regarded as the strongest oxidative species in organic oxidation and thus extensively applied in photocatalytic remediation of organic pollutants. Nevertheless, in selective organic oxidation, •OH can result in the nonselective oxidation of organics into CO_2 and water instead of value-added organic chemicals, therefore great efforts have been made to suppress the formation of •OH in

order to improve selectivity of the reaction.(*22, 23*) It should be noted that, because of a higher diffusion coefficient ($3.0 \pm 0.2 \times 10^{-10}$ m^2/s) compared with H_2O_2 ($1.1 \pm 0.1 \times 10^{-10}$ m^2/s) or $O_2^{\bullet-}$ ($2.9 \pm 0.3 \times 10^{-12}$ m^2/s),(*24*) •OH has a particular influence on the oxidation of organic molecules that have weak affinity to the catalyst surface.

$$H_2O + h^+_{(VB)} \rightarrow \bullet OH + H^+ \ (E^0 = 2.38 \text{ V } \textit{vs.} \text{ SHE}) \qquad (2\text{-}7)$$

2.2.4 Singlet oxygen ($^1O_2$)

Singlet oxygen ($^1O_2$) could be generated by transforming energy from the triplet state of a photosensitizer to a ground state oxygen molecule (reaction 2-8). It has been suggested that the oxidation of $O_2^{\bullet-}$ by photoactivated holes could also yield $^1O_2$ species (reaction 2-9).(*25*) As a moderate oxidant compared with •OH and $O_2^{\bullet-}$, $^1O_2$ can effectively oxidise organic chemicals while avoiding the overoxidation.

$$O_2 + h\nu \rightarrow {}^1O_2 \qquad (2\text{-}8)$$

$$O_2^{\bullet-} + h^+_{(VB)} \rightarrow {}^1O_2 \ (E^0 = 2.53 \text{ V } \textit{vs.} \text{ SHE}) \qquad (2\text{-}9)$$

2.3 Mechanisms of selective photocatalytic oxidation

With the rapid development of materials science, there have been tremendous demand and application of catalytic organic synthesis. Photocatalysis has been applied in the oxidation of various organic chemicals, typically including alcohols, hydrocarbons, aromatics, and amines, which shows distinctive aspects from the conventional approaches, eg. very moderate condition and very benign to the environment. Fundamental understandings on the mechanisms behind these reactions are critical to improve catalyst activity

and selectivity and avoid complete mineralisation of organic substance to CO_2 and water. The following will mention these attractive reactions one by one, and the effect of reaction environment, which will help understand the strategies discussed latter for selectivity control that is paramount in organic synthesis.

2.3.1 Oxidation of alcohols

The selective oxidation of alcohols is a major route to synthesis carbonyl chemicals. Conventional oxidation of alcohols often involves thermal-catalytic processes or strong oxidising agents such as chromate, permanganate, and hypervalent iodine.(*26*) These processes inevitably generate hazardous wastes and inherently suffer from low selectivity towards target high value chemicals due to the harsh conditions used. In contrast, photocatalytic oxidation of alcohols provides a more environmental-friendly alternative for carbonyl compounds synthesis. the basic mechanism of alcohol oxidation is then discussed taking benzyl alcohol oxidation as a model reaction.

A mechanism was proposed based on the direct participation of photoactivated holes and $O_2^{\bullet-}$.(*20*) Benefited from the sufficiently negative CB of mesoporous carbon nitride (CN) polymer, $O_2^{\bullet-}$ could be generated by the reduction of molecular oxygen under visible light. Benzyl alcohol was first reacted with photogenerated holes to deprotonate on the basic surface of CN to form corresponding radical. Recombination of this radical and $O_2^{\bullet-}$ finally formed the ketone molecule. One might see that there were different opinions about the role of $O_2^{\bullet-}$ in benzyl alcohol oxidation. When using $Bi_{12}O_{17}Cl_2$ nanobelts as a photocatalyst, only the photoactivated holes took part in the oxidation of benzyl alcohol. The oxidising capability of the holes, i. e., the VB

position of the photocatalyst, largely affected the selectivity.(*27*) Though the activation of oxygen molecules into $O_2^{\bullet-}$ was important, this process was most regarded to inhibit the recombination of photogenerated charge carries.

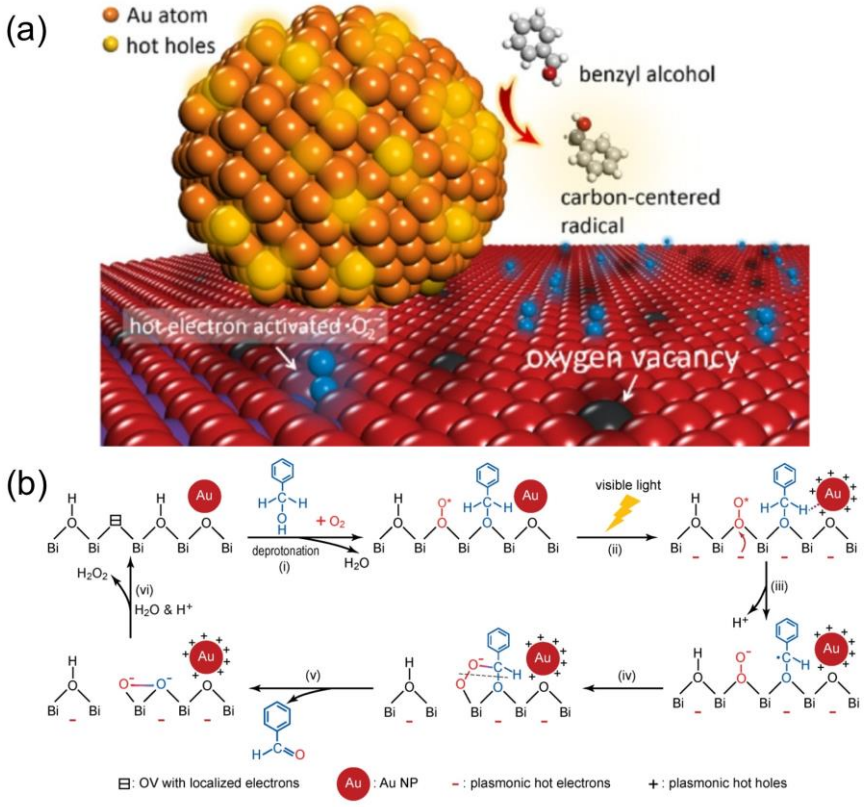

Figure 2. (a) Schematic illustration of the generation of reactive species over Au loaded BiOCl with oxygen vacancies. (b) Proposed mechanism of selective benzene alcohol oxidation.(*28*) Copyright (2017) American Chemical Society.

On the other hand, the subsequent studies supported the radical-$O_2^{\bullet-}$ recombination mechanism and brought some different insights.(*28*) It was reported based on a plasmonic catalyst of Au supported on BiOCl containing oxygen vacancies. Upon the excitation of Au nanoparticles, hot electrons were trapped at oxygen vacancies, while hot holes remained on the Au surface (**Figure 2**). Although the hot electrons and holes were spatially separated, the unique structure of the surface of BiOCl allowed the co-adsorption of O_2 and

benzyl alcohol, ensuring the hot electrons and holes worked cooperatively in benzyl alcohol oxidation. Hot holes on Au nanoparticles efficiently attracted the α-H of benzyl alcohol to form carbon-centered radicals, while hot electrons could easily transfer to adsorbed O_2, generating $O_2^{\bullet-}$ species. Closely located carbon-centered radicals and $O_2^{\bullet-}$ species were prone to combine toward the formation of an oxygen-bridged structure. Concerted bond cleavage of this structure would form benzaldehyde. More recently, it was found that In_2S_3 nanosheets with abundant S vacancies could effectively oxidise benzyl alcohol.(*29*) Although the holes participated in the reaction, experimental results showed that the excellent oxidation ability of In_2S_3 was due to the facilitated $O_2^{\bullet-}$ generation. This study implied that radical-$O_2^{\bullet-}$ recombination could be the main mechanism in photocatalytic alcohols oxidation.

Although the decisive evidence for actual mechanism of alcohol oxidation has yet elucidated, especially the role of $O_2^{\bullet-}$ is debatable, all current results indicate that the primary oxidants should be photoactivated holes and $O_2^{\bullet-}$. Therefore, for a semiconducting photocatalyst, VB position, the electron affinity of the substrate, and the ability to generate $O_2^{\bullet-}$ are all of great significance when applied for selective alcohols oxidation.

2.3.2 Oxidation of saturated C-H bonds

Compared with the selective alcohol oxidation, the selective oxidation of saturated C-H bonds is more difficult due to the higher bond energy. In this field, most researchers have focused on two reactions: toluene to benzaldehyde and cyclohexane to cyclohexanone. Combining most of the literature information,(*30-34*) the mechanism of hydrocarbons photooxidation can be

summarised by the following reactions. Generally, hydrocarbon is first oxidised to alkyl radicals ($^{\bullet}RH$) *via* photogenerated holes:

$$RH_2 + h^+_{(VB)} \rightarrow {}^{\bullet}RH + H^+ \quad (2\text{-}10)$$

This process is widely recognised as a rate-determining step due to the inertness of saturated sp^3 C-H bonds. Molecular O_2 can react with $^{\bullet}RH$ with a diffusion-controlled rate to generate peroxy radicals ($^{\bullet}OORH$):

$$^{\bullet}RH + O_2 \rightarrow {}^{\bullet}OORH \quad (2\text{-}11)$$

Subsequently, resulting $^{\bullet}OORH$ can react with various ROS to generate alcohols and carbonyl compounds:

$$^{\bullet}OORH + e^-_{(CB)} + H^+ \rightarrow RO + H_2O \quad (2\text{-}12)$$

$$^{\bullet}OORH + O_2^{\bullet-} + H^+ \rightarrow RO + O_2 + H_2O \quad (2\text{-}13)$$

$$2\,{}^{\bullet}OORH \rightarrow RO + RHOH + O_2 \quad (2\text{-}14)$$

$$RHOH + 2{\bullet}OH \rightarrow RO + 2H_2O \quad (2\text{-}15)$$

If the reaction media contains excess strong oxidants like •OH, further oxidisation of target products will take place, even up to complete mineralisation:

$$RO + O_2^{\bullet-}/{\bullet}OH/\ h^+_{(VB)} \rightarrow ROOH \rightarrow \text{mineralisation} \quad (2\text{-}16)$$

Therefore, adsorption–desorption equilibria of reactants and reaction intermediates are two important factors determining the final product distribution.

2.3.3 Oxidation of benzene

Phenol is an important organic chemical which could be used in a wide range of applications. Conventionally it could be produced by sulfonation, chlorination or cumene processes.(*35*) All these synthesis methods require harsh conditions and involve hazardous chemicals. Direct hydroxylation of benzene provides a green alternative route and makes it possible to improve selectivity as the benign conditions are used in the process. The direct hydroxylation of benzene means to activate the unsaturated sp^2 C-H bonds, this is similar to the activation of the saturated form: initiated by photoactivated holes with sufficient oxidising ability. The oxidation potential of benzene in acetonitrile was reported to be 2.48 ± 0.03 V (*vs.* SCE),(*36*) thus a photocatalyst with sufficiently positive VB is necessary for this reaction. Subsequently, the formed cationic radical species of benzene are further attacked by various ROS (mainly O_2 or $O_2^{\bullet-}$), finally transformed into phenol molecules (**Figure 3**).(*37*) In the presence of excessive strong oxidant species, phenol could be overoxidised into a variety of phenol derivatives including hydroquinone, benzoquinone, finally CO_2 and H_2O.(*38*)

Oxidisation *via* photogenerated holes requires benzene to contact catalyst surface. For those photocatalyst with poor adsorption ability to benzene, holes react primarily with H_2O molecules, yielding •OH that subsequently attack the benzene ring to produce hydroxycyclohexadienyl radical.(*39, 40*) The release of the proton radicals from the hydroxycyclohexadienyl radical would result in the formation of phenol.

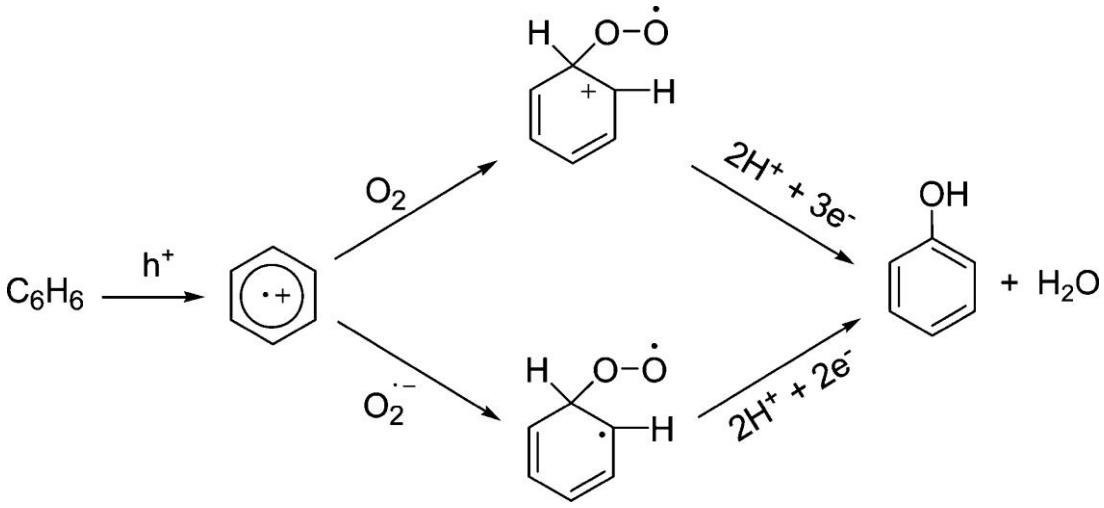

Figure 3. Proposed mechanism for production of phenol from benzene through a hole transfer process using O_2 as the oxygen source.(*37*) Copyright (2010) American Chemical Society.

2.3.4 Oxidation of amines

Imines, a group of chemical compounds containing C=N bonds, are important building blocks for the production of pharmaceuticals, pesticides and other value-added chemicals. Currently they could be prepared by the dehydration of amines and carbonyl compounds such as aldehydes, in which dehydrating agents and Lewis acid catalysts are involved, therefore generating excessive wastewater. In 2011, TiO_2-mediated aerobic oxidation of amines for imines formation was realised under UV light,(*15*) Since then, considerable efforts have been devoted to photocatalytic production of imines. The general mechanism in amines oxidation begins with the generation of hole-electron pairs (**Figure 4**). The holes initiate the deprotonation of amine to form a neutral carbon-centered radical. At the same time, the electrons activate molecular oxygen into $O_2^{\bullet-}$. Then, the two radicals react with each other to generate H_2O_2 and NH-imine intermediates which are further transformed into the desired imines.(*41*)

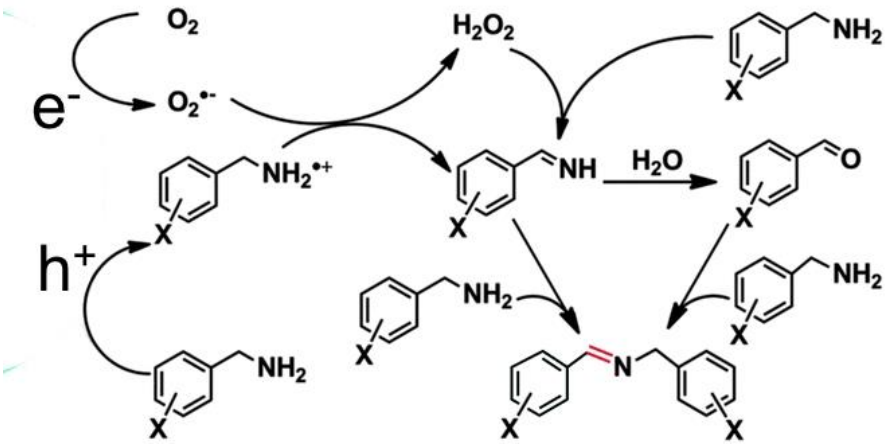

Figure 4. Proposed mechanism for benzylamine aerobic oxidation reaction pathways over layer double hydroxide.(*41*) Copyright (2014) The Royal Society of Chemistry.

So far, the possible mechanisms in the selective photocatalytic oxidation reactions have been briefed, mainly involving the roles of oxidant species. It should be noted that all mechanisms reported in these literatures are very general. The actual reaction routes and final products differ from different photocatalysts, affected by band positions, charge carrier transfer, and the affinity of the photocatalysts to reactants. On the other hand, new photocatalytic reaction routes are emerging quickly in recent years, for example, the epoxidation of alkenes.(*42-45*) Predictably this will intensify the related research area and bring to the forefront of green chemistry.

2.3.5 Reaction environment

Despite intrinsic characteristics of photocatalysts, the reaction environment also plays an important role. For example, the employed solvent can strongly affect the interaction between the photocatalyst surface and the substrate. When using TiO_2 to oxidise cyclohexane in various solvents, selectivity to cyclohexanol and cyclohexanone were found to be dependent on adsorption.(*46*) Selectivity was higher in polar solvents because cyclohexanol

adsorbed on TiO_2 to a lesser extent. In non-polar solvents, cyclohexanol preferentially adsorbed onto TiO_2 thus being completely mineralised.

When water is used as the solvent in photocatalytic oxidation reactions, it could be easily adsorbed on the photocatalyst surface and then oxidised by photoactivated holes, generating highly oxidising hydroxyl radicals. Thus, an organic solvent such as acetonitrile is often used in photocatalytic oxidation reactions. Organic solvents differ in viscosity, polarity, polarisability, and hence they have different abilities to stabilise intermediate species. Solvent choice can therefore provide another methods for controlling selectivity.(*47*)

One of the aims of photocatalytic oxidation is to avoid harsh operating conditions such as high temperature and pressure, which are typically required in conventional industrial routes. Therefore, the majority of photocatalytic oxidation reactions are conducted at room temperature. However, earlier research did investigate the effect of reaction temperature. In the oxidation of liquid cyclohexane using acetonitrile as a solvent, it has been found that the activity was higher in the medium temperature region (295 – 328 K).(*48*) At low temperature (< 295 K), the limiting step became the desorption of the main product while at temperature > 328 K, the limiting step became the adsorption of the reactant.

When establishing a heterogeneous photocatalytic process for organic synthesis by oxidation, the major challenge is the generation of moderate oxidising species, which can avoid the loss of products due to complete mineralisation. Obviously, controlling the formation of ROS is a challenging yet rewarding task. In the next section, various strategies will be presented to

minimise the mineralisation and shift the reaction toward the desired products thus achieving excellent selectivity.

2.4 Improving the selectivity of photocatalytic oxidation

The most important for organic synthesis is to control the selectivity to products, which is also the key challenge for photocatalysis due to the extremely strong oxidative capability of diverse ROS. The following focuses on the proved strategies to overcome the challenge.

2.4.1 Band engineering

One issue with a semiconductor for photocatalytic for selective organic synthesis is the highly oxidative environment due to the deep VB of the semiconductor that can completely mineralise the organic substances. As indicated above, the oxidation of an organic substrate can be initiated either directly by holes, or through an indirect route, in which ROS are generated and then in turn oxidise the organic molecules. Therefore, manipulating the band structure, especially the band positions of a given photocatalyst is an effective strategy to minimise the over-oxidisation of organic substrates in photocatalytic oxidation reactions, thereby tuning selectivity.

Different semiconductors may have significantly different CB and VB potentials, which determine the thermodynamic feasibility of what reactions could proceed, and the potential products. Therefore, while evaluating the thermodynamic driving forces for the reactions of interest, enhanced selectivity could be achieved by appropriate selection of a semiconductor. An example is

the selective photocatalytic oxidation of benzene to phenol in water containing molecular oxygen. Pt nanoparticles (NPs) loaded WO_3 was reported to photocatalytically generate phenol from benzene with high selectivity (e.g. 74% at 69% of benzene conversion), that was much higher than that over TiO_2, which produced CO_2 as the main product.(*39*) The difference in selectivity was attributed to the distinction of CB positions between WO_3 and TiO_2. Photogenerated electrons on Pt/WO_3 tended to initiate two-electron reduction of O_2, generating H_2O_2, which could not over-oxidise produced phenol. In contrast, the electrons at the CB of TiO_2 readily generated oxygen radical species such as $O_2^{\bullet-}$, which led to the successive oxidation of phenol to CO_2, thus reducing the selectivity.

TiO_2 could generate various highly oxidative radical species under UV light, which generally leads to a high degree of mineralisation. Optimising solvents to control lifetime and speciation of radicals could enhance selectivity to some extent. However, cases where a high selectivity was achieved are relatively scarce.(*49*) Altering the electronic properties of TiO_2 to shift the reaction selectivity has been proved to be a feasible way. Through doping Ru into TiO_2 nanotubes, the selectivity of toluene oxidation to benzaldehyde under UV irradiation was largely enhanced.(*50*) The energy levels of introduced Ru ($Ru^{3+/4+}$ states) were located at a more positive position than the CB of TiO_2, with an insufficient potential for single-electron reduction of molecular oxygen. Since the Ru levels tended to trap the photoactivated electrons, the generation of excessive $O_2^{\bullet-}$ was significantly suppressed, thus inhibiting the overoxidation of benzaldehyde to benzoic acid. This strategy was also adopted to alter VB positions, as some experiments indicated that the selectivity of photocatalytic

oxidation could also highly depend on the VB position of semiconductors.(*27*) For example, when the N- and S-doped TiO_2 photocatalysts were under 442 nm light irradiation, a greater amount of $O_2^{\bullet-}$ was generated than that from the pristine TiO_2 (P25) irradiated at 325 nm.(*23*) Moreover, S-doped TiO_2 mainly produced $O_2^{\bullet-}$, while N-doped TiO_2 generated more H_2O_2 under the same condition. This difference was attributed to multivalence property of sulfur atoms which may promote the decomposition of H_2O_2. In another example, by modifying $TiNb_2O_7$ with nitrogen dopants, new N 2p orbitals were formed.(*51*) Combining with the introduction of oxygen vacancy levels, the electronic structure of $TiNb_2O_7$ was modulated to a narrower band gap for more photoabsorption. When the modified photocatalyst was used in the conversion of benzylamine under green light irradiation, the yield and selectivity of N-benzylidenebenzylamine was significantly improved compared to unmodified samples.

In recent years, the rapid development of the metal-organic frameworks (MOFs) has brought new impetus for the study of selective oxidation reactions. MOFs are constructed from metal or metal cluster nodes interconnected with multi-dentated organic linkers, in which the metal nodes serve as semiconductor quantum dots while the organic linkers serve as the antenna to sensitise these quantum dots. In 2008, isoreticular MOFs with a series of organic linkers were demonstrated to oxidise gas-phase propylene under UV irradiation.(*52*) Results showed that the band gap of these MOFs could be altered by changing the organic linker. Moreover, the change in bandgap resulted in different activity and product distribution. Later, the discovery of Ti-containing MIL-125(Ti) represented another breakthrough in photocatalytic

oxidation, though it could only be activated by UV light.(*53*) To expand the light absorption of MIL-125(Ti) to the visible region, the organic linker BDC was substituted on the aromatic ring with amine groups.(*54*) Experimental results showed that only a small amount of -NH_2 motif is sufficient to reduce the bandgap of the monoaminated series of MIL- 125(Ti) analogues. This strategy was successfully applied in the aerobic oxidation of amines under visible light.(*55*) A wide range of amines could be oxidised into imines with yields ranging from 45 to 93% over NH_2-MIL-125(Ti).

Except for substituting organic linkers, the light absorption property of MOFs could also be tuned by doping ions into metal clusters. For example, after incorporating Fe^{3+} ions into a representative MOF, Uio-66, metal-to-cluster charge transfer could be induced, which reduced the bandgap and resulted in the extended visible light response.(*56*) By sharp contrast to the completely inert UiO-66, the unique electron transfer enabled Fe-Uio-66 to oxidise H_2O into •OH and thereafter oxidise hydrocarbons, particularly toluene, under visible light irradiation.

2.4.2 Metal loading

In the pioneering studies on photocatalytic oxidation, titanium dioxide was often used as a photocatalyst as at that time researchers already had some understanding on its role in the decomposition of harmful organic compounds. However, the application of pristine TiO_2 in organic synthesis was unsuccessful because reactions usually lack satisfied selectivity. With its deep VB, TiO_2 normally creates a highly oxidising environment that leads to complete mineralisation, therefore generating unexpected products. Moreover, its large

bandgap confines its photoabsorption in the UV region. Therefore, metal loading, as an effective strategy to tackle this problem, has been extensively applied in relevant studies.

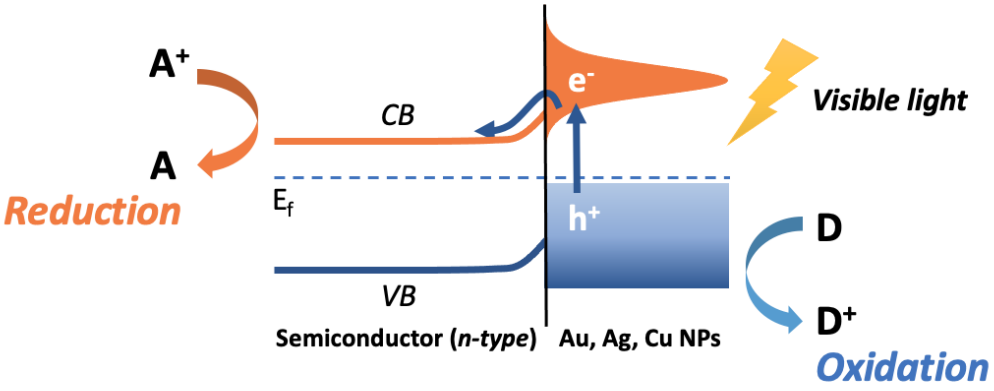

Figure 5. Surface plasmonic metal (Au, Ag, or Cu) NPs for visible light induced reactions.

With regard to the interfacial charge transfer, there are two mechanisms proposed when loading metals on the surface of photocatalysts: the plasmonic effect and the Schottky junction. For plasmonic metals like Au, Ag and Cu, when the frequency of incident photons is close to the natural frequency of surface electrons oscillation against the restoring force of positive nuclei, collective oscillation of electrons will take place, which is called surface plasmon resonance (SPR) (**Figure 5**). Due to the SPR effect, the absorbance spectra of surface plasmon bands generated by Au (25 nm diameter), Ag (38 nm diameter), and Cu (133 nm diameter) spherical nanoparticles (NPs) show strong visible-light absorption. Such absorption maxima, eg. at 530, 400, and 580 nm, vary with the particle size, respectively,(*57*) thus providing a feasible way to tune the redox potential of the active electrons and holes by manipulating the NPs size. When loading plasmonic NPs on semiconducting

photocatalysts like TiO_2, visible light could excite electrons below the Fermi level (E_f) of the plasmonic NPs to the surface plasmon (SP) states, leaving positive charges (h^+) below E_f. Electrons at SP states subsequently transfer into the CB of semiconductors, and ultimately to electron acceptors like O_2, facilitating efficient selective aerobic oxidation. At the meantime, h^+ left in NPs could react with the organic substrate to complete the photocatalytic cycle,(*58*) these holes have a much weaker oxidation potential than those in the VB of TiO_2. The other major mechanism involved here is Schottky junction, a potential energy barrier formed at a metal–semiconductor interface, which stops the electrons transferring back to the NPs across the Schottky junction – this is the reason why Schottky junction enhances charge separation.

Taking Au loaded CeO_2 as an example, it was used for the selective oxidation of benzyl alcohols to corresponding benzaldehydes in aqueous suspension under visible light.(*59*) Electrons in Au NPs was excited and injected into the CB of CeO_2, and the electron depleted Au NPs oxidised organic compounds. The role of hot electrons was further presented in Au loaded BiOCl.(*28*) Under visible light irradiation, plasmonic hot electrons were trapped and transferred to adsorbed O_2, producing $O_2^{\bullet-}$ radicals. Meanwhile, the loss of electrons lowered the Fermi level of Au NPs, endowing with the oxidation ability.(*60*) Therefore, benzyl alcohol was mildly oxidised on the Au surface to corresponding carbon-centered radicals and then combined with $O_2^{\bullet-}$ radicals to form benzaldehyde. When using Au NPs loaded TiO_2, amines were efficiently oxidised to imines without overoxidation, showing the mild oxidation ability of Au NPs.(*61*) All above results suggested that Au NPs could effectively generate

electrons and mild oxidative holes under visible light irradiation, both species are beneficial to the selective oxidation.

Au loaded semiconductors could also be employed in oxidation reactions requiring relatively strong oxidants, for example, benzene to phenol reaction. The oxidation potential of benzene in acetonitrile was reported to be about 2.48 V (*vs.* SCE),(*36*) thus a photocatalyst with sufficiently positive VB is required for this reaction. Holes in Au NPs have a significantly lower oxidation potential, obviously the Au NPs could not directly take part in the benzene oxidation. However, Au loaded $Ti_{0.98}V_{0.02}O_2$ was found to oxidise benzene under UV light.(*62*) Although there was no significant phenol production under visible light on Au loaded $Ti_{0.98}V_{0.02}O_2$, loading Au on the catalyst indeed boosted the production of phenol under UV light. Combined with other results, they argued that the role of Au NPs was mainly for charge separation. Au NPs selectively stored photoexcited electrons and in turn maximized holes utilization on $Ti_{0.98}V_{0.02}O_2$. The reason why electrons transferred from $Ti_{0.98}V_{0.02}O_2$ to Au NPs rather than the opposite was that only UV light could not trigger significant SPR effect in Au NPs due to the mismatch of the absorption maximum of Au NPs with the UV wavelength, causing the electron flow to the Fermi level of Au NPs.(*63*).

Apart from gold, other noble metals, such as Pt and Pd, were also widely used as cocatalysts in selective photocatalytic oxidation. For example, Pt NPs supported on anatase TiO_2 were reported to promote selective alcohol oxidation under visible light irradiation ($\lambda > 450$ nm) at room temperature.(*63*) Visible light excited electrons in Pt NPs, the electrons then transferred to the anatase conduction band. The positively charged Pt particles mildly oxidised

substrates, whereas the electrons in TiO_2 were consumed by the reduction of O_2 - similar to the Au loaded photocatalysts. Further experiments indicated that the activity of this photocatalyst depended on the height of Schottky barrier and the number of perimeter Pt atoms at the Pt/TiO_2 heterojunction, which were affected by the amount and size of Pt NPs. As reported, increasing the amount of metal loaded onto the semiconductor led to a larger Schottky barrier due to the decrease in the Fermi level of the semiconductor,(*64*) which is arguable. Increased Schottky barrier would suppress electron transfer from photoactivated Pt NPs to TiO_2. On the other hand, the electrons of Pt NPs mainly transferred to TiO_2 *via* the peripheral Pt atoms, hence the number of perimeter Pt atoms may affect the transfer efficiency. Therefore, subtly tuning the amount and size of Pt NPs was of great significance in this reaction. Specifically, the catalyst with 2 wt % Pt, containing 3-4 nm Pt nanoparticles showed the highest photocatalytic activity. Later, the same group found Pd loaded TiO_2 in alcohol containing primary amine could efficiently promote N-monoalkylation of amine with alcohol, producing the corresponding secondary amine with almost unity yield under $\lambda > 300$ nm light.(*65*) In this reaction, Pd first oxidised alcohol on the photoactivated TiO_2, then condensation of the formed aldehyde with amine occurred on the TiO_2 surface. Finally, the formed imine was hydrogenated by the surface H atoms on the Pd particles. Calculating the number of surface Pd atoms revealed that the Pd atoms on the triangle site of Pd NPs were the active site for hydrogenation. Meanwhile, larger triangle sites strongly adsorbed alcohols and suppressed imine hydrogenation. Because the rate-determining step was the imine hydrogenation, the photocatalysis selectivity was closely related to the size of the Pd NPs. As a

result, the catalyst containing 0.3 wt % Pd and 2 - 2.5 nm Pd particles showed the highest activity for imine hydrogenation. The above results highlight the importance of the size and amount of metal nanoparticles, both parameters have significant influences on the plasmonic effect and Schottky junction, then affecting charge transfer and oxidation capacity of catalysts while the interpretation is arguable, requiring further investigation.

Considering the high cost of noble metals, researchers have been increasingly interested in non-noble metals loaded catalysts. For instance, Ni clusters were presented having the ability to boost photocatalytic synthesis of imines from amines oxidation *via* the release of hydrogen (H_2).(*66*) By constructing *in-situ* photodeposited Ni clusters on the CdS photocatalyst, imines were formed at a dramatically improved rate under visible light illumination. Mechanistic investigation revealed that the desorption of photogenerated hydrogen atoms during the dehydrogenation of amines was significantly promoted on Ni clusters, thus resulting in the fast formation of C-centered radicals and then the generation of imines.

In some cases, loading monometal on photocatalysts cannot completely solve the problem. For example, TiO_2 in O_2-saturated water can generate H_2O_2 *via* two-electron reduction of O_2 under UV light, provided the presence of electron donor such as alcohols. The problem is that the yield of H_2O_2 is significantly low (<0.2 mM).(*67*) This is because the generated H_2O_2 can react with OH groups on TiO_2 surface and is converted to peroxy species (Ti-OOH), then decomposed by the reduction of electrons. Loading Au NPs can collect and trap electrons from the TiO_2 CB owning to the effect of Schottky junction. This suppresses the reduction of Ti−OOH species. Moreover, two-electron

reduction of O_2 is favoured on the Au NPs, therefore the introduction of Au can boost the efficiency of H_2O_2 production. However, H_2O_2 molecules tend to strongly adsorb onto the Au NPs and be decomposed into •OH and OH^- by the reduction of electrons.(*68*) In this context, TiO_2 loaded with Au−Ag bimetallic alloy particles was demonstrated to efficiently produce H_2O_2 from an O_2-saturated ethanol/water mixture under UV irradiation.(*67*) The introduction of Ag atoms could suppress photocatalytic decomposition of formed H_2O_2 due to the decreased adsorption of H_2O_2 onto the Au atoms. Another example is Au-Pd/$ZnIn_2S_4$ composite, which could selectively oxidise aromatic alcohol under visible light.(*69*) The reason for the introduction of Pd was because Pd NPs possessed superior adsorption and activation ability for O_2. Hot electron excited in Au would inject into Pd NPs to generate $O_2^{\bullet-}$. In another case, visible-light irradiation (λ > 450 nm) of Au–Cu alloy particles supported on TiO_2 was reported to successfully promote aerobic oxidation without catalyst deactivation.(*70*) Compared with Au loaded TiO_2, the Au–Cu alloy loaded catalysts exhibited much higher activity owing to the alloying effect. In the meantime, collective oscillation of electrons in the surface Au atoms could reduce the oxidised Cu atoms and keep the Au–Cu alloying effect (**Figure 6**). Bimetal loading gives photocatalysts novel properties and new possibilities, further studies in this strategy could lead to the discovery of high-performance photocatalysts, which effectively promote the production, separation and utilization of photoexcited carriers in organic synthesis.

Since the first terminology proposed by Zhang et al. in 2011,(*71*) single atom catalysts (SACs), involving the isolated metal atoms stabilised on appropriate supports, have become one of the most innovative and active research frontiers

in the entire field of heterogeneous catalysis. The exclusively high activity and selectivity brought by the unsaturated coordination sites and unique electronic structures of SACs render them promising materials for photocatalytic organic synthesis. In addition, well-defined single-atoms as active sites make the clear identification of reaction mechanisms possible. This has seen success in selective dehalogenation reactions,(*72*) and further progress could be expected in photocatalytic oxidation reactions.(*73*)

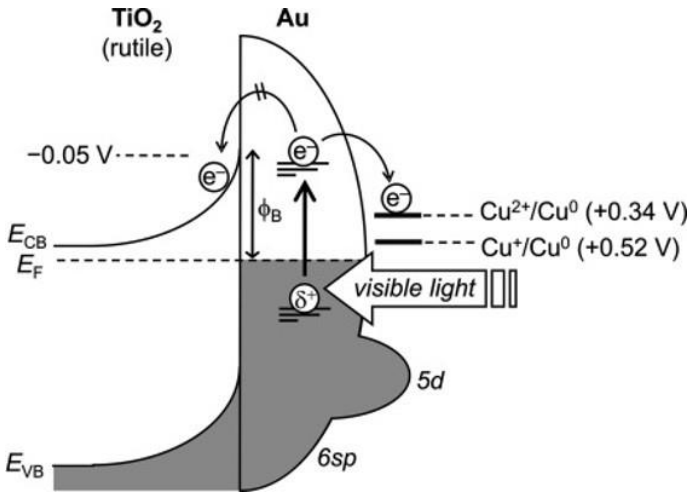

Figure 6. Possible energy diagram (*vs.* NHE) for plasmon-activated AuCu/P25 catalysts under visible-light irradiation.(*70*) Copyright (2013) John Wiley and Sons.

2.4.3 Hybrid materials

Hybridising non-metal components such as carbon-based materials or metal oxides with photocatalysts can take advantage of the unique properties of different materials, providing researchers a powerful toolkit to manipulate the light harvesting, adsorption ability and ultimately the activity and selectivity of photocatalysts. Moreover, the formed internal electric field arising from the suitably matched band structures could promote the transfer of photogenerated charge carriers, facilitating the charge separation.

Like metal loading, the early work encompassing hybrid materials focused on TiO_2-based catalysts. For example, composite catalyst combining multi-walled carbon nanotubes (CNT) and TiO_2 was prepared by means of a modified acid catalysed sol–gel method.(*74*) When applying this catalyst for phenol oxidation, broadened absorption was observed, especially in the visible spectral range. Further investigation indicated that the activation of near-UV to visible light irradiation was due to a synergy effect: CNT acting as a photosensitizer agent instead of an adsorbent or a dispersing agent. In parallel, reduced graphene oxide (rGO) hybridised TiO_2 was found to catalyse photooxidation of cyclohexane to cyclohexanone with enhanced activity and selectivity under UV light ($\lambda > 300$ nm).(*32*) The TiO_2/rGO hybrids generated cyclohexanone two times higher than the amount produced on bare TiO_2, also with a much higher selectivity (> 80%) than that of bare TiO_2 (ca. 60%). Mechanism analysis showed that the photoactivated electrons in TiO_2 CB band could transfer to rGO, facilitating efficient charge separation and enhancing photocatalytic activities (**Figure 7**). The trapped electrons on rGO selectively promoted the activation of O_2 *via* two-electron reduction and suppressed one-electron reduction. This process could largely inhibit the generation of $O_2^{\bullet -}$, which was responsible for the photocatalytic decomposition of formed cyclohexanone. In this way rGO could effectively accelerate selective oxidation of cyclohexane on the hybrid catalyst.

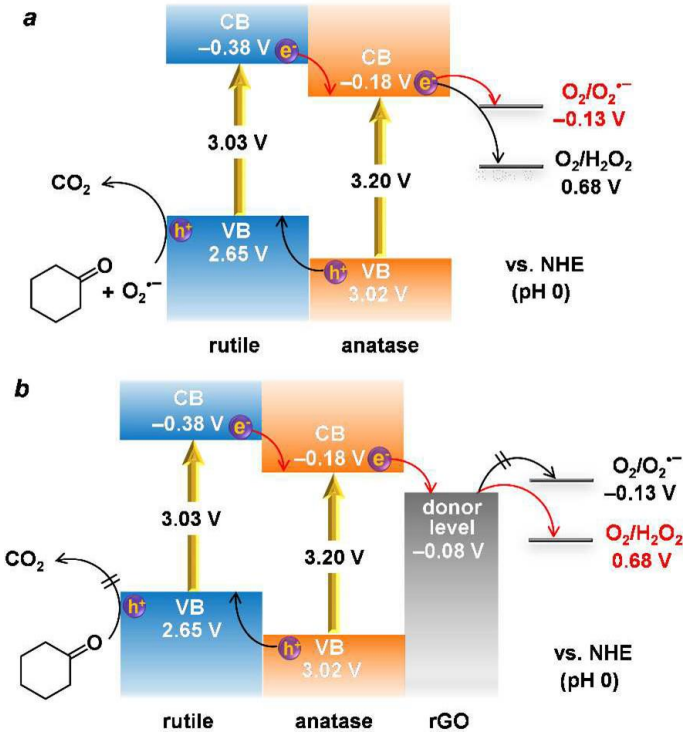

Figure 7. Energy Diagrams for (a) TiO_2 and (b) TiO_2/rGO when used in selective cyclohexane oxidation.(*32*) Copyright (2017) American Chemical Society.

TiO_2 can also be hybridised with other metal oxides, leading to the adaptation of a semiconductor junction architecture. For example, TiO_2 particles loaded with WO_3 were used for alcohol oxidation in water in the presence of O_2 and $\lambda > 350$ nm light.(*75*) The WO_3/TiO_2 hybrid catalyst could selectively oxidise alcohols into aldehydes at a higher catalytic activity and selectivity than bare TiO_2. The enhanced selectivity to aldehyde was attributed to the inhibition of photocatalytic decomposition of the formed aldehyde on the catalyst. When partially coating TiO_2 by WO_3, the adsorption ability of aldehyde by TiO_2 was weakened, thus suppressing subsequent photocatalytic decomposition of aldehyde on the TiO_2 surface, and thus achieving high selectivity.

Rapid development of controllable fabrication of nanocomposites has brought new light in highly active photocatalyst fabrication. Among them, the core-shell nanocomposites are particularly interesting due to their novel properties. TiO_2 nanofibers with a single-crystal TiO_2(B) core and a shell of anatase nanocrystals were produced and then applied to the alcohol oxidation.(*76*) Meanwhile, Ce^{3+} ions were introduced into the (110) lattice planes of the TiO_2(B), in which the redox potential of Ce^{3+}/Ce^{4+} couple (1.715 V *vs.* NHE) was more negative than the VB of TiO_2(B). Therefore, the doped Ce^{3+} ions could collect photogenerated holes, leaving electrons in anatase shell and leading to a highly efficiency charge separation. This may increase the chance for the activation of O_2 molecules adsorbed on the anatase surface, thereby improving the photoactivity. Moreover, these doped ions can effectively trap the highly oxidative holes, thereby overoxidation of the alcohol could be avoided.

In addition to the extensively studied TiO_2, CdS, a semiconductor with a narrower bandgap, has also been widely used as a component in hybrid photocatalyst for organic oxidation. Taking core-shell structured CdS@CeO_2 composite (with CeO_2 as the shell layer) as an example, this hybrid photocatalyst was used in the oxidation of benzyl alcohol.(*77*) Apart from the enhanced charge separation, the redox couple Ce^{4+} /Ce^{3+} in CeO_2 shell could also transfer the electrons from the inner layer of CeO_2 shell to its outer layer. The holes were employed for the oxidation of alkoxide species, while the $O_2^{\bullet-}$ radicals facilitate the dissociation of the methylene C-H bond, thus forming benzaldehyde and hydro-peroxide species. As the photoactivation of CdS core was also very important, the transmittance and charge transferring capacity to

the outer component was quite important for core-shell photocatalysts. Another successful case is porous $Cd_3(C_3N_3S_3)_2$ and CdS composite, which was employed for selective oxidation of toluene under visible light ($\lambda > 420$ nm).(*78*) The high selectivity was closely related to the proper band position of the two components: the CB of CdS was sufficiently negative to reduce O_2 and the VB of $Cd_3(C_3N_3S_3)_2$ was inadequate to oxidise OH group to •OH radicals. Meanwhile, the heterojunction structure could promote charge separation and boost the yield of benzaldehyde.

In 2018, photochromic Bi_2WO_{6-x}/amorphous BiOCl (*p*-BWO) nanosheets has been discovered to be an efficient material for oxidation of benzylic C-H bonds in toluene.(*33*) The hybrid nanosheets could become blue under visible light irradiation and be bleached by atmospheric oxygen. Further investigation revealed that photoactivated electrons could reduce $W_{(VI)}$ into $W_{(V)}$, and $W_{(V)}$ could be oxidised by O_2 to regenerate $W_{(VI)}$. Therefore, the introduction of amorphous BiOCl provided abundant $W_{(VI)}O_{6-x}$ units, which could serve as the centres for the fast and continuous consumption of photogenerated electrons, thereby effectively promoting the separation of charge carriers.

More recently, MXenes, a new family of two-dimensional (2D) transition metal carbides, carbonitrides or nitrides, have become a promising material to construct hybrid photocatalysts. Their strong light absorption ability, low Fermi level, and electrical conductivity render them an ideal cocatalyst to broaden light absorption and collect electrons in composite catalyst. In organic synthesis, a low-temperature wet chemistry process was proposed to fabricate uniformly distributed CdS NPs on the 2D platform of $Ti_3C_2T_x$ MXene nanosheets.(*79*) The composites showed a significant enhancement in the aqueous photoredox

conversion of furfural alcohol to furfural and H_2 by simultaneously utilizing photogenerated holes and electrons. Here, MXene nanosheets acted as an “electron sink”, facilitating the separation and transport of electrons activated in CdS NPs. Electrons accumulated in MXene nanosheets then initiated the H_2 generation reaction. Meanwhile, the photoactivated holes in CdS NPs oxidised furfural alcohol into value-added furfural, thereby completing the catalytic cycle.

Covalent organic frameworks (COFs), in which building blocks are connected through covalent bonding, have emerged as an exciting class of crystalline porous polymers and been successfully applied in photocatalytic reactions.(*80*) For example, highly hydrophilic COF material TFPT-BMTH, with high crystallinity and good chemical stability, exhibited significant catalytic activity in photocatalytic oxidation of benzylamine in water under visible light.(*81*) However, the rapid recombination of photoactivated charge carriers is a main inhibiting factor for COFs to display excellent catalytic performance. Taking advantage of their large surface area and abundant functional groups, MOFs could be ideal platforms to hybridise with COFs, forming heterostructures and thus improving the photocatalytic ability. A successful case is the covalent-connected NH_2-MIL-125@TAPB-PDA nanocomposite.(*82*) The results showed that hybridising MOF and COF through covalent bonding could effectively extend the light absorption band and reduce the recombination rate of photogenerated charge carriers. When testing for benzyl alcohol oxidation, the hybrid showed a 15.5-time improvement in conversion compared with bare TAPB-PDA and remained stable after 5 cycles. Thus, hybrid strategy has shown tremendous potential in the optimisation of MOF and COF materials as photocatalysts.

2.4.4 Defect engineering

Defects can naturally exist or be artificially created in materials. The defects in semiconducting photocatalysts can change band gaps to improve light absorption, serve as active sites to separate photoactivated electron-hole pairs, and participate in molecular chemisorption with significantly reduced energy barrier. By virtue of the progress in material preparation methods and newly developed characterization technologies (especially aberration-corrected high-angle annular dark-field imaging scanning transmission electron microscopy (HAADF-STEM) and X-ray absorption spectroscopy), the past decade has seen a huge leap in the defects engineering for photocatalytic materials. Various kinds of defects, including vacancies, dislocations, and structural distortions, have been introduced and proved to be an effective strategy for enhancing the efficiency and selectivity of photocatalytic oxidation reactions.

It is well-known that the chemisorption plays a critical role in photocatalysis, which not only facilitates the transfer of photoactivated charge carriers to reactants, but also changes the formation of ROS to achieve an excellent selectivity. To promote the chemisorption of O_2 molecules on surface of a photocatalyst, defect-rich WO_3 nanosheets were investigated for aerobic oxidation of amines to corresponding imines.(*83*) HAADF-STEM images revealed that the sample surface contained numerous small dots. Concomitant with these dots, lattice disorders and dislocations were found inside of the nanosheets. These dots were considered as the defect sites, which could enhance the chemisorption of molecular O_2 to WO_3 surface. Moreover, they favoured the transmission of photoexcited electrons to adsorbed O_2, forming superoxide radicals in a chemisorbed state ($*O_2^-$). The $*O_2^-$ radicals possessed

identical oxidative capacity to free $O_2^{\bullet-}$, meaning they could react with the hole-activated substrate molecules located at the neighboured O atoms. In this way, photoexcited electrons and holes could be well-separated at different sites. Because the energy to create $*O_2^-$ was relatively lower than $O_2^{\bullet-}$, a small photon energy could be utilised. Therefore, the aerobic oxidation of amines to corresponding imines at room temperature could efficiently proceed under visible-near-infrared illumination.

While optimisations of chemisorption and charge separations have been regarded as the most effective strategies for the regulation of charge carrier generation in photocatalysts, some researchers devoted to the excitonic aspects of photocatalysts. An exciton, widely exists in semiconductors, is a bound state of electron−hole pair attracted by the electrostatic Coulomb force. Therefore, the dissociation of excitons into free charges would be a promising strategy for charge carrier utilisation in photocatalysis. Because excitons are preferentially to dissociate into hot electrons and hole at the area with a disordered energy landscape, introducing disordered region should improve the utilization efficiency of the excited charges. From this point, carbon nitrides with abundant order−disorder interfaces have been thoroughly investigated in which the enhanced hot-carrier generation was observed.(*84*) Density functional theory **(**DFT) simulations revealed lower highest occupied molecular orbital (HOMO) and lowest unoccupied molecular orbital (LUMO) energy levels of ordered domains compared with the energy levels of disordered domains (**Figure 8**). This means hot electrons could be injected into ordered chains and holes could be blocked in disordered chains. Benefiting from this unique

structure, the sample exhibited largely enhanced $O_2^{\bullet-}$ radical generation and improved selective alcohol oxidation.

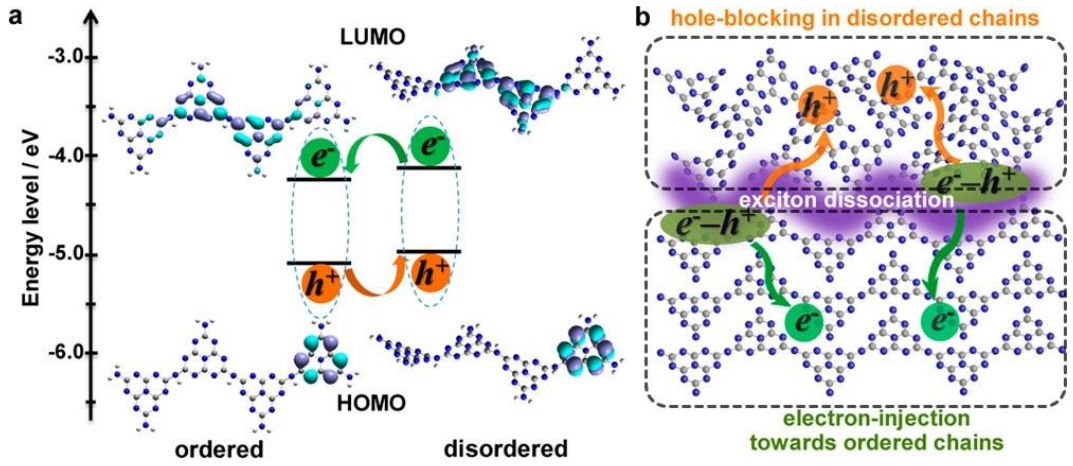

Figure 8. (a) DFT simulations of ordered and disordered heptazine-based chains. Inset: corresponding charge-carrier transfer behaviours (blue balls, nitrogen atoms; gray balls, carbon atoms). (b) Schematic illustration of exciton dissociation and charge transfer in semicrystal-line heptazine-based melon.(*84*) Copyright (2017) American Chemical Society.

If above mentioned dots and disordered interfaces could be regarded as volume defects, point defects, including various kinds of vacancies, are frequently introduced in selective oxidation reactions. It is worth noting that under certain conditions, point defects may act as recombination centres for electron-hole pairs during photocatalytic processes.(*85*) However, there is ample research that utilizes point defects to suppress charge recombination. For example, introducing oxygen vacancies (OVs) into Au loaded BiOCl would trap hot electrons generated in plasmonic Au NPs.(*28*) Moreover, OVs can enhance the adsorption ability to O_2 molecules, reducing them into $O_2^{\bullet-}$ radicals. Together with the mild oxidative ability of hot holes, this photocatalyst highly favoured the generation of benzaldehyde along with an exceptional oxygen atom transfer from O_2 to the product. Likewise, in another case, cubic indium sulfide (β-In_2S_3) was chosen as a model system and introduced surface S

vacancies.(*29*) DFT calculations revealed an obvious increased density of states at the VB maximum in In_2S_3 after the introduction of S vacancies (**Figure 9**). This means the electrons could be photoexcited to the CB and transferred to defective surface more efficiently, thus suppressing electron-hole recombination. Moreover, S vacancy site had a negative adsorption energy of -0.31 eV with molecular O_2, while pristine In_2S_3 showed no obvious interactions. These properties made In_2S_3 with S vacancies an ideal material to efficiently generate $O_2^{\bullet-}$ radicals. Together with the photoactivated holes, this catalyst showed excellent performance for photocatalytic benzylic alcohols oxidation reactions under visible-light irradiation.

Except for bulk materials, vacancies could even be introduced in some 2D materials. Although this is far more challenging because of the ion/defect migration. Interestingly, unit-cell Bi_2WO_6 monolayer was reported to provide a suitable model for this task as W-site defects in the interior WO_4 layer were relatively stable. In this context, interior W vacancies rich Bi_2WO_6 monolayers were prepared and found to be an efficient photocatalyst for benzylic alcohols oxidation.(*86*) Under illumination, photoactivated holes in the $[BiO]^+$ surface layers could oxidise benzyl alcohol while electrons in the $[WO_4]^{2-}$ layer experienced a long migration toward the edge of catalyst to reduce O_2. W vacancies introduced mid-gap states into the defect Bi_2WO_6, making electrons more easily excited by low-energy photons. This explained the enhanced visible absorption and higher photoconversion efficiencies.

With suitable introduction of vacancies, some polymer materials could also be applied in selective alcohol oxidation. For example, nitrogen vacancies were introduced into the framework of carbon nitrides by a high-temperature thermal

condensation method.(*87*) In the resultant material, the nitrogen vacancies were grafted on the uncondensed terminal NH_x lattice sites, which led to the improvement of the photogenerated charge carrier separation. When used in photocatalytic selective oxidation of aromatic alcohols, the catalyst achieved 68.3% benzyl alcohol conversion and almost 100% selectivity under simulated sunlight irradiation.

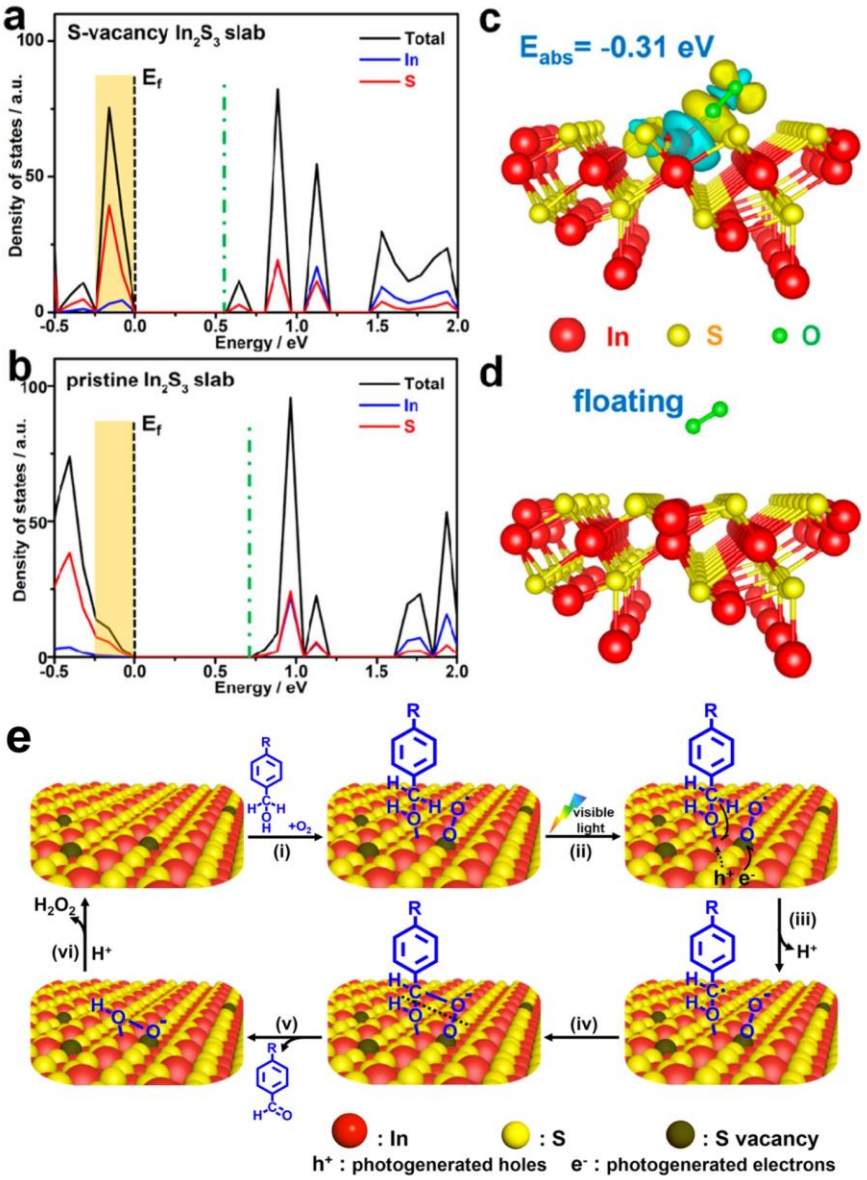

Figure 9. Calculated DOS of (a) S-vacancy and (b) pristine In_2S_3 slabs (E_f = Fermi level; orange shading marks the increased DOS around the VBM). (c) O_2 interacts with the S vacancy in the defective In_2S_3 slab. (d) O_2 floating on the surface of the pristine In_2S_3 slab. (e) Proposed mechanism of

photooxidation of benzyl alcohol to benzaldehyde over defective In_2S_3.(*29*) Copyright (2019) American Chemical Society.

Studies on benzene and amine oxidation also explored the potential benefits of the vacancies in photocatalysts. Zn_2Ti-layered double hydroxide was used for selective oxidation of benzene to phenol in water.(*88*) The abundance of oxygen vacancies improved charge separation and $O_2^{\bullet-}$ generation, resulting in the excellent catalytic performance under Xe lamp irradiation. When using ultrathin HNb_3O_8 nanosheets with abundant oxygen vacancies in the photocatalytic oxidative coupling reaction of benzylamine, enhanced performance under visible light irradiation was observed.(*89*) Benzylamine was preferentially adsorbed on the O vacancies on HNb_3O_8, forming a surface complex. It has been proved that this surface complex could reduce the bandgap of HNb_3O_8, making the material responsive to the visible light. Under irradiation, photogenerated holes reacted with adsorbed benzylamines to form the corresponding nitrogen-centered radicals. Simultaneously, photogenerated electrons activated O_2 into $O_2^{\bullet-}$ at the same site. After a series of reactions, the resultant intermediates could be converted into imines. In another paper, Bi_2WO_6 containing Au NPs and oxygen vacancies was applied for the same reaction.(*90*) The role of O vacancies for efficient adsorption−activation of molecular O_2 has been verified in this work. Moreover, the existence of Au NPs further boosted the generation of hot electrons, therefore resulting in the enhanced photocatalysis.

2.4.5 Morphology and crystallisation control

Through manipulating the morphology of photocatalysts, the selectivity could be promoted in organic oxidation reactions. As described in Section 2.3.3,

benzene could be oxidised by the •OH radicals formed on the photoexcited semiconductors surface. The formed phenol is, however, subsequently attacked by •OH radicals, leading to a low phenol selectivity. This problem could be solved by using mesoporous TiO_2 particles (*m*TiO_2) prepared through surfactant-templating method or particle aggregation method.(*91*) Because benzene are less polar molecules, they tended to adsorb on the less polar inner surface of *m*TiO_2. After they were converted into polar phenol, they were hardly adsorbed onto the *m*TiO_2 surface. It has been claimed that the photogenerated •OH radicals within the pores of *m*TiO_2 were transformed into inactive surface OH groups at a near-diffusion controlled rate. However, there is no direct evidence to support this claim. •OH radicals could react with adsorbed benzene and leave phenol intact, resulting into highly selective oxidation (81 % selectivity). Soon after this, the same group further verified this adsorption-driven photocatalysis strategy by employing microporous titanosilicate ETS-10 (Engelhard Titanosilicate Structure 10) for the same reaction.(*92*)

Modifying morphologies can not only alter the adsorption behaviour of substrates, separation of photogenerated charge carriers could also be promoted in some cases. Sheet structured semiconductor CdS with a cubic phase was demonstrated to selectively oxidise C-H bonds under visible light irradiation in toluene.(*93*) Although the authors could not give a plausible explaination for the enhanced activity and selectivity of resultant catalyst, they showed that crystalline phase, surface area and particularly morphology all had important impact on photocatalytic activity. These factors would result in different geometric and electronic structures in catalysts, thus endowing them with excellent photocatalytic performance. Similar phenomenon was also

observed in single-crystalline BiOCl ultrathin nanosheets with a square morphology.(*94*) Additionally, distinctive from the nanoplates prepared by hydrothermal route, BiOCl ultrathin nanosheets featured the hydrophobic surface, which could be beneficial to the selective oxidation of amines.

The rapid development in the synthesis of advanced low-dimensional materials has brought more remarkable semiconducting materials as photocatalysts. Sometimes these newly developed photocatalysts demonstrate intriguing properties. For instance, Ultrathin black phosphorus (BP) nanosheets exhibited an excitation-energy-dependent effect in photocatalytic ROS formation.(*95*) Interestingly, $^1O_2$ and •OH could be almost exclusively generated under visible- and UV-light irritations, respectively. In-depth analysis revealed that there were two different subband systems in the ultrathin BP nanosheets, making it feasible for the energy-transfer and charge-transfer processes proceed in different subband structures (**Figure 10**). Subband structures, resulting from giant electron−electron interactions and specific band dispersions, had mainly been observed in one-dimensional materials including single-wall carbon nanotubes. Under visible-light irradiation, the resonance energy transfer from the excited excitons of BP in its inner subband system to the ground-state oxygen promoted generation of $^1O_2$. When irradiated with UV light, photogenerated holes in the outer subband system oxidised water into •OH radicals. This novel optically switchable property has shed new light on the photocatalysis research and could be potentially applied in the selective oxidation reactions because of controllable ROS generation.

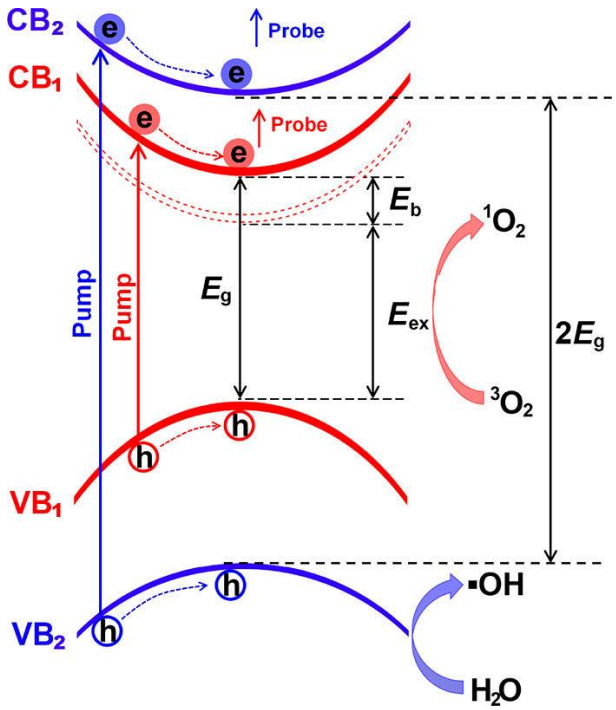

Figure 10. Schematic illustration of the subband structure of ultrathin BP nanosheet as well as the photoexcitation and photocatalytic processes occurring therein. The optically switchable ROS generation of $^1O_2$ and •OH are depicted corresponding to the internal and external band systems, respectively. CB_n and VB_n (n = 1, 2) denote the n-th conduction band and valence band, respectively. E_{ex} and E_b stand for the excitonic energy level and exciton binding energy, respectively.(*95*) Copyright (2018) American Chemical Society.

Besides the manipulating of morphologies, subtly tuning the crystallisations of photocatalysts could be an alternative way to increase photocatalytic efficiency. This is particularly important for polymer materials, because extended π-conjugated system and strong van der-Waals interactions between interlayers both benefit to the charge transport.(*96*) For inorganic materials, pioneering researchers extensively studied the different phases of TiO_2, providing rich understandings for its application in selective oxidation. For example, anatase TiO_2 exhibited excellent activity for oxidation, though the desorption of target chemicals is sluggish.(*37*) In most cases, higher degree of crystallization means more efficient separation of charge carriers. However,

less-crystalline rutile TiO_2 exhibited a higher selectivity in alcohol oxidation.(*97*) The enhanced selectivity was attributed to the facilitated charge recombination, and consequently the restricted generation of strong oxidative •OH radicals. Additionally, OH groups formed from deactivated •OH radicals were favoured to adsorb on less-crystalline catalyst, forming a more hydrophilic surface. Desorption of resultant aldehydes were therefore improved, so was their selectivity.

In recent years, lead-free halide perovskites with ABX3 stoichiometry (where A = monovalent cation, B = In^{3+}, Bi^{3+}, Sb^{3+} or Sn^{3+}, X = halide anion) have been demonstrated to be promising photocatalysts because of their appropriate bandgap and remarkable charge transfer properties. Modification of X-site and B-site ions can alter their band positions therefore control the light absorption and redox abilities. Although A-site ions are not involved in the formation of band gaps, they can cause octahedron distortions in the perovskite structure. This effect has been proved by using $Cs_3Sb_2Br_9$ NPs in photocatalytic toluene oxidation to benzaldehyde.(*34*) The results showed the octahedron distortion induced by A-site cations led to the enhanced ability of hole transfer from Br sites to toluene molecules. Together with the generation of $O_2^{\bullet-}$ radicals, benzaldehyde molecules were efficiently formed at a high selectivity. Because Br atoms on the surface were responsible for the formation of holes, and the octahedron distortion significantly affected its electronic properties, modification of A-site cations had a prominent effect on the photocatalytic efficiency in C(sp^3)-H bond oxidation.

2.4.6 Surface states manipulation

In photocatalytic reactions, the adsorption and oxidation of reactants, and the desorption of target chemicals all occur on the surface of photocatalysts. Therefore, the surface states largely affect the performance of the catalysts. Up to date, various surface states modification methods have been developed to tailor the surface characters. For example, the effect of silylation on the photocatalytic activity of anatase TiO_2 catalyst was investigated in selective cyclohexane oxidation.(*98*) The yield of cyclohexanone was closely related to the desorption rate of cyclohexanone and the abundance of surface active OH sites. Silylation to an appropriate extent could improve the desorption of cyclohexanone thereby the selectivity was increased. Also due to the facilitated desorption rate, the formation of surface deactivating carbonate and carboxylate species on TiO_2 was suppressed. Meanwhile, another strategy to modify anatase TiO_2 has been proved to be feasible: clean the catalyst surface to expose active OH sites as many as possible.(*99*) This could be achieved though pretreating anatase with different Brønsted acids. Surface modification of TiO_2 with both inorganic and organic acids significantly accelerated the oxidation of alcohols under irradiation of UV light at room temperature, without any compromise of selectivity compared to the untreated TiO_2. This unique proton cleaning effect was attributed to the promotion of decomposition of the surface Ti/peroxide species and regeneration of Ti sites in the selective oxidation of alcohols. Similar cleaning strategy has also been applied in Nb_2O_5 photocatalysts for the oxidation of aromatic hydrocarbons - the treatment even broadened the photocatalytic absorption to the visible region.(*100*) It turned out that the vacuum heat treatment enhanced the electron transfer between the

aromatic ring and Nb_2O_5 surface, which served as an electron donor and an electron acceptor, respectively. This could initiate the absorption of visible light (λ > 390 nm) due to the ligand-to-metal charge transfer **(**LMCT) transition (**Figure 11**). Selective photooxidation of aromatic hydrocarbons to corresponding carbonyls could therefore be effectively facilitated under visible light irradiation. Interestingly, similar treatment did not lead to the same phenomenon on TiO_2, which might result from the weaker electron-accepting ability of TiO_2.

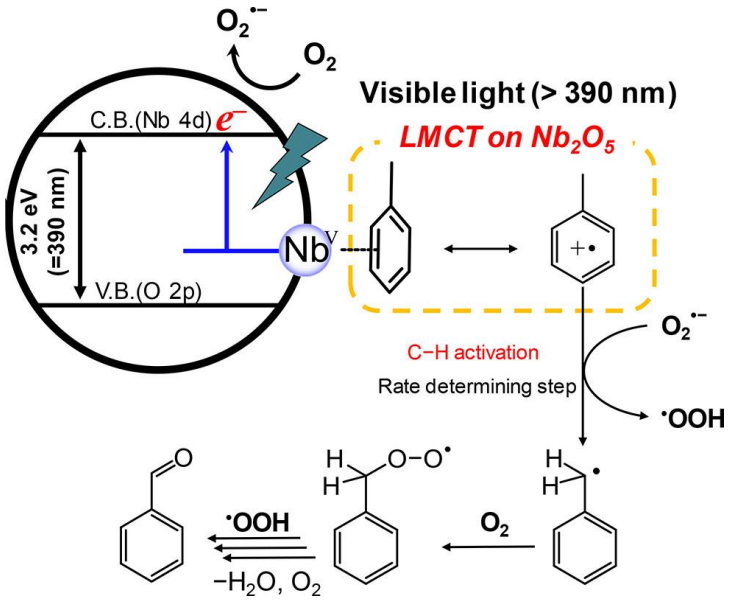

Figure 11. Proposed mechanism of visible-light photooxidation of aromatic hydrocarbons via a ligand-to-metal charge transfer (LMCT) transition on the surface of Nb_2O_5 after vacuum heat treatment.(*100*) Copyright (2017) American Chemical Society.

Compared with inorganic materials, the polymer photocatalysts has brought great opportunities to graft various functional groups on the surface and therefore potentially achieving optimal performance. For example, the oxidised carbon nitride was reported to significantly boost generation of triplet-exciton.(*101*) While enhancing the generation of $^1O_2$, the production of other

ROS was concomitantly suppressed, rendering it an excellent material in $^1O_2$-demanding organic synthesis. The remarkable difference in ROS generation properties between oxidised CN and untreated one was due to their distinct excitonic behaviours. Electron spin resonance (ESR) measurements revealed that oxidising CN incorporated abundant carbonyl groups, which could synergistically promote spin–orbit coupling and reduce singlet–triplet energy gap of the matrix (**Figure 12**). Therefore, an efficient inter-system crossing process was initiated, in which the excitons could readily transform from singlet excited state to lower-energy triplet excited states, further transferring energy to ground-state oxygen molecules to generate $^1O_2$. In another case, cyano groups were introduced onto the surface of CN nanosheets *via* a facile thermal post-treatment, which constructed a homojunction-like structure.(*102*) This structure could efficiently facilitate the generation of charge carriers, thus promoting the formation of $O_2^{\bullet-}$ radicals. This photocatalyst was employed in oxidative coupling of diverse amines to corresponding imines under λ > 420 nm light and achieved 2.4 times higher activity than pristine CN.

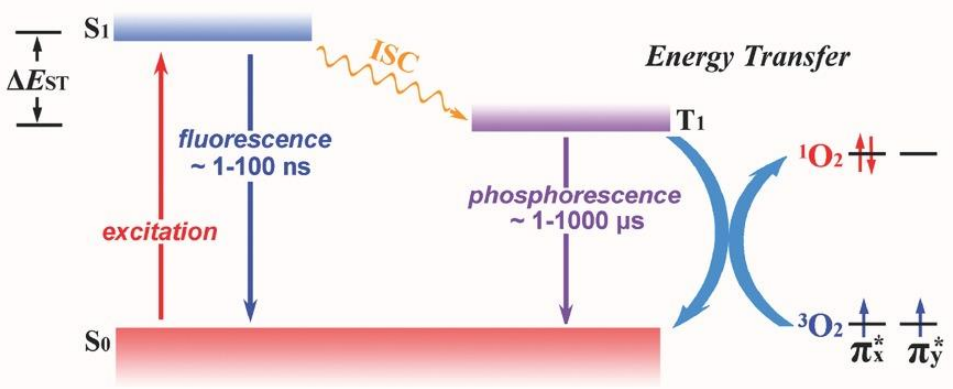

Figure 12. Illustration of the typical excitonic processes in the conjugated structure and the energy transfer process for $^1O_2$ generation.(*101*) Copyright (2016) John Wiley and Sons.

2.5 Summary

Although it is environmentally friendly, operated under very mild conditions and sustainable, the application of selective photocatalytic oxidation presents far more difficulties and challenges compared with other applications such as complete decomposition of the organics in the environmental protection. The key issue in the selective oxidation is the control of ROS and adsorption-desorption behaviour. The past few decades have seen substantial progress in the development of photocatalytic oxidations. In this chapter, besides the basic mechanism of photocatalysis and several typical oxidation reactions are briefed, key strategies to improve the selectivity are detailed. In general, these strategies show positive effects on photocatalytic organic oxidations, such as broadening the region of light absorption, facilitating charge carrier separation and transport, and promoting reactant adsorption and activation processes, all of which are crucial steps in photocatalytic processes as detailed in the above sessions.

As mentioned at the beginning, synthesis of organic chemicals has been developed for almost 200 years with many landmark achievements. Most of the industrial production of these organic chemicals are conducted at high temperature and under elevated pressures, resulting in significant energy consumption and adverse environmental impacts. Organic synthesis triggered by light irradiation, might be under sunlight, and in a benign environment has been proved to be a feasible approach while still requiring vigorous and substantial investigation.

3. Experimental

This chapter will describe the facilities and methods used to characterise materials prepared in the project.

3.1 X-ray diffraction (XRD)

XRD patterns were recorded on a PANalytical X' pert diffractometer with a Cu–Kα radiation source (40 kV and 40 mA). A continuous mode was used to record data in the 2θ range from 10° to 90°. When irradiating a beam of X-rays onto a crystal with an angle of θ, it would be reflected off atomic planes in the crystal with the same angle θ. The X-rays reflecting off two different planes would interfere either constructively to form an interference pattern, or destructively to form no pattern. To interfere constructively, the difference in path length between the two atomic planes must be a whole number (n) of wavelengths (λ), or nλ. Therefore, X-ray diffraction pattern would occur when Bragg's equation (3-1) is satisfied, in which d is the spacing between different planes. By analysing the diffraction, the crystalline structure of the crystal can be determined.

$$2d \sin \theta = n\lambda \qquad (3\text{-}1)$$

3.2 Microscopies

Transmission electron microscopy (TEM) and energy-dispersive X-ray spectroscopy (EDX) mapping experiments were performed on a JEOL JEM-2100F microscope operated at 200 kV, equipped with an Oxford Instruments ISIS/INCA energy-dispersive X-ray spectroscopy system with an Oxford Pentafet ultrathin window detector. The aberration-corrected high-angle annual

dark-filed scanning transmission electron microscopy (AC-HAADF-STEM) was performed on a JEOL JEM-ARM200F equipped with a CEOS probe corrector, with a guaranteed resolution of 0.08 nm. The EDX elemental analysis was obtained on JEOL JEM-2100F with the accelerating voltage of 200 kV. Before microscopy examination, 1 mg sample was ultrasonically dispersed in 3 ml ethanol for 20 min, and then 1-2 droplets of the suspension were dripped onto a copper TEM grid coated with a thin carbon film.

3.3 X-ray photoelectron spectroscopy (XPS)

XPS measurements were conducted on a Thermo ESCALAB 250Xi spectrometer equipped with an Al anode (Al Kα = 1846.6 eV), operated at 15 kV and 10.8 mA. *In-situ* XPS measurements were carried out on the same instrument, using a Xe-lamp as the light source if denoted otherwise. Survey scans were collected in the range 0–1,350 eV (binding energy) at the pass energy of 150 eV. CasaXPS software was used to process XPS data.

3.4 Ultraviolet–visible spectroscopy (UV-vis)

UV-Vis absorption spectra were obtained on a PerkinElmer Lambda 950 UV-Vis-NIR spectrophotometer fitted with an integrating holder. Reflectance measurements were performed on powdered samples using the standard barium sulphate powder as a reference. The reflection measurements were converted to the absorption spectra using Kubelka–Mulk transformation.

3.5 X-ray absorption spectra (XAS)

The X-ray absorption spectra (XAS) including X-ray absorption near-edge structure (XANES) and extended X-ray absorption fine structure (EXAFS) at Ni

K-edge of the samples were measured at the beamline 11B of Shanghai Synchrotron Radiation Facility. The output beam was selected by Si(311) monochromator, and the energy was calibrated by the corresponding metal foil. The data were collected at room temperature under transmission mode. Athena software package was employed to process the XAS data.(*103*)

3.6 Electron paramagnetic resonance (EPR)

EPR was conducted on a Bruker A200 electron spin resonance spectrometer at ambient temperature (288 K). Samples (~20 mg) were weighed and transferred into quartz tubes. A high-pressure mercury-vapour lamp (500 W) was used as the light source. As for the $^1O_2$ electron spin resonance (ESR) trapping measurements, 100 μL of aqueous suspension of samples (4 g L^{-1}) was mixed with 100 μL of 2,2,6,6-tetramethylpiperidine (TEMP, 50 mM) solution. After being illuminated for 2 min, the mixture was characterized using a Bruker A200 electron spin resonance spectrometer. The $O_2^{\cdot-}$ and ·OH trapping-ESR tests were performed in methanol and deionised water as described above, using 5,5-dimethyl-1pyrroline-N-oxide (DMPO, 50 mM) as the spin-trapping agent.

4. Selective transformation of glycerol to glycolaldehyde by single-atom photocatalyst Ni/TiO_2

This chapter mainly discusses the single-atom photocatalyst Ni/TiO_2 which was synthesised *via* a molten-salt method and is composed of nickel single atoms confined on titanium dioxide. Driven by light, the catalyst can convert glycerol into glycolaldehyde under ambient conditions using air as a green oxidant, resulting in the selectivity of over 60% to glycolaldehyde and nearly 3 times higher turnover number than NiO_x nanoparticle-decorated TiO_2 photocatalyst.

4.1 Introduction

Biomass resources are produced by the photosynthesis of CO_2 and water using solar energy and are widely available in the natural environment. Driven by the sustainable and environmentally sound use of natural resources, transforming biomass and biomass derivatives into value-added products has gained increasing significance. One of the most important strategies is the C-C bond cleavage of biomass-derived polyols for the synthesis of valuable carbonyl compounds such as aldehydes, acetic acid and ketone derivatives.(*104-106*) Because the C-C bond cleavage is thermodynamically unfavourable due to the relatively high stability of the C-C bond (90 kcal mol^{-1}), the developed C-C bond cleavage processes, most of which are thermocatalytic reactions driven by energy- and cost-intensive systems, heavily depend upon toxic/expensive oxidants, noble metal catalysts, and often require

harsh conditions.(*107*) Selective C-C bond cleavage under mild conditions is therefore much sought after as a valuable tool to upgrade biomass-derived polyols.

Glycerol is such a highly versatile polyol which is regarded as a biowaste but also an important platform molecule for the production of high-value chemicals.(*108*) With this potential, substantial efforts have been devoted to exploring an efficient catalyst to achieve high conversion and high selectivity to the targeted products. Photocatalysis has been recognised as a promising strategy in C-C bond cleavage reactions under very mild conditions.(*109*) Several pioneering and insightful works have been dedicated to this area. For example, TiO_2 photocatalysts with different dominant facets were used to selectively convert glycerol to glycolaldehyde in an aqueous solution and inert atmosphere. The product selectivity was verified to be strongly dependent on the facets of TiO_2,(*110*) while the production rate was rather moderate (e.g. 83.8 $\mu mol \cdot g^{-1} \cdot h^{-1}$ of glycolaldehyde). Later, a mechanistic picture at the molecular level of photocatalytic C-C bond cleavage of ethylene glycol was developed by coupling *in-situ* surface science study on rutile (110) surface with *in-situ* vibrational-mass spectrometry study on TiO_2 nanoparticles in an ultra-high vacuum condition.(*111*) The C-C bond cleavage was found to be the only pathway in ethylene glycol photo-conversion under deaerated conditions, leading to the formation of formaldehyde and hydrogen. The rate-determining step in this process is the desorption of the surface adsorbed hydrogen, making pristine TiO_2 a poor photocatalyst that only catalyses the ethylene glycol conversion at very low surface coverages. Recent work introduced oxygen into this process, revealing that the presence of oxygen could readily convert

organic products into CO_2 *via* complete oxidation by oxygen, or into paraformaldehyde by polymerisation with water.(*112*) With this attractive progress so far, the relatively low selectivity in the presence of O_2 requires the rational design of photocatalysts. One barrier is that most semiconductor-based photocatalysts are either non-selective (particularly with the presence of water and/or oxygen) or ineffective to break down the C-C bond because of poor oxidative activity.(*113, 114*) This is because once oxygen and/or water are involved as reactants, a series of strong reactive oxygen species (ROS) could be generated, unselectively mineralising organic compounds into CO_2 and water.(*18*) Moreover, the oxidants and products often encounter diffusion limitations while approaching or leaving the active sites on catalysts, resulting in poor interfacial contact that constrains the catalytic reactions. More importantly, the role of metal (or metal oxide) nanoparticles that are frequently applied as promoters remains unclear and sometimes controversial due to the involvement of complex factors including diverse particle sizes, exposed facets, and chemical states. Single-atom photocatalysts have provided an ideal platform to address the above challenges benefitting from their uniform geometrical/electronic structure, exotic properties, and maximum atom-utilization efficiency.(*73*) For example, according to DFT simulation, when anchoring Ni single atoms on the anatase TiO_2 surface, new vacant levels are generated near the conduction band minimum.(*2*) The excited electrons in the anatase conduction band can be readily transferred to the surface levels of the Ni species, thus achieving effective charge separation. These well-defined active sites may open up the possibility of regulating the generation of ROS,

tailoring adsorption/desorption properties, and understanding structure-activity relationships.(*115*)

Up to now, highly selective photocatalysts for aerobic C-C cleavage of glycerol to synthesise valuable chemicals are so challenging with few studies reported. In this chapter, earth-abundant Ni single atoms were precisely anchored on TiO_2 by a novel molten-salt method. The photocatalyst can highly selectively cleave C-C bond of glycerol in the presence of air at room temperature and under atmospheric pressure. Furthermore, diverse *in-situ* and *operando* spectroscopies clarify Ni single atoms as both the oxygen adsorption sites and the acceptor of photogenerated electrons. This bifunction of Ni single atoms efficiently generates superoxide radicals, resulting in over 60% selectivity towards glycolaldehyde, together with high efficiency and long-term stability.

4.2 Experimental

4.2.1 Photocatalyst synthesis

The single Ni atom decorated TiO_2 (Ni/TiO_2-MS) was prepared by a molten-salt method. 0.9 g of LiCl, 1.1 g of KCl, 1 g of TiO_2 nanoparticles, and x mg of $NiCl_2 \cdot 6H_2O$ (x= 2, 8, 20 and 40, equal to w.t. 0.05, 0.2, 0.5, and 1.0% to TiO_2) were pestled in a mortar for 0.5 h to make a homogeneous mixture. The mixture was then transferred into an alumina crucible and calcined at 500 °C for 2 hours under a N_2 atmosphere (heating rate: 8 °C/min) in a tube furnace. After naturally cooling down to room temperature, the mixture was washed with water thoroughly by vacuum filtration to remove the salts (LiCl & KCl). The obtained Ni/TiO_2 was dried in a vacuum oven at 60 °C. When using HCl solution to wash

Ni/TiO_2-MS, the 20 mg sample was dispersed in 20 ml 1 M HCl aqueous solution and stirred for 2 h. The same procedure was conducted for the preparation of Cu/TiO_2-MS, except a certain amount of $CuCl_2 \cdot 2H_2O$ instead of $NiCl_2 \cdot 6H_2O$ was used. For Ag/TiO_2-MS and Au/TiO_2-MS, the TiO_2 was first mixed with a certain amount of $AgNO_3$ or $HAuCl_4 \cdot 3H_2O$ aqueous solution. After stirring at ambient temperature overnight, the obtained solid was then mixed with LiCl and KCl to conduct molten-salt preparation method.

For a comparison, NiO nanoparticles loaded TiO_2 (Ni/TiO_2-IM) was prepared through an impregnation method. 20 mg of $NiCl_2 \cdot 6H_2O$ was first dissolved in 1 ml of deionized water, then added dropwise into 1 g of TiO_2 with vigorous stirring. After all the water had evaporated from the semi-solid mixture, it was then transferred into a capped alumina crucible, placed inside a muffle furnace in the air. The mixture was heated at a ramping rate of 5 °C min^{-1} and held at 400 °C for 4 h. After naturally cooling down to room temperature, the sample was then washed with water thoroughly by vacuum filtration. The same procedure was conducted for the preparation of Cu/TiO_2-IM, Ag/TiO_2-IM and Au/TiO_2-IM, except a certain amount of $CuCl_2 \cdot 2H_2O$, $AgNO_3$ or $HAuCl_4 \cdot 3H_2O$ aqueous solution was used.

4.2.2 Material characterisation

The Ni loading amount was determined with ICP-AES on an IRIS Intrepid II XSP instrument (Thermo Electron Corp.). Temperature-programmed desorption of oxygen (O_2-TPD) patterns were collected using a chemisorption analyser (Micromeritics AutoChem II). Dried samples were loaded in a plug flow reactor with a quartz tube 1/8" in diameter and pre-treated in helium (He) at

400 °C for 60 min. After being cooled to 50 °C, oxygen adsorption was performed by flowing O_2 (20 mL/min) for 60 min. The physically adsorbed oxygen was then removed by purging with He for 30 min. For desorption, the temperature was increased from 50 °C to 600 °C at a ramping rate of 10 °C/min. The desorbed oxygen was carried out by a flow of He (20 mL/min) and analysed by the GC.

4.2.3 Photocatalytic activity test

The photocatalytic activity measurements of glycerol oxidation were carried out in a Perfectlight PCX50A Discover multichannel system with 5W 365 nm light sources (light intensity ≈ 20 mW/cm^2). The reaction temperature was controlled to about 25 °C using a cooling fan. A magnetic stirrer was used to facilitate the mass transfer between the reactants and photocatalysts. In a typical test, 15 mg photocatalyst was first added into 30 ml 25 mM glycerol aqueous solution. The mixture was sealed in a 50 ml reactor and then sonicated to form a homogeneous suspension. After the reaction, the photocatalyst was removed by filtration, and the aqueous solution was analysed by a high-performance liquid chromatography (HPLC, Shimadzu LC-20AB) equipped with a Rezex ROA-Organic Acid H+ (8%) column, a diode array detector (Shimadzu SPD-M20A), and a refractive index detector (Shimadzu RID-20A), using a 5 mM H_2SO_4 aqueous solution as the mobile phase. The gaseous products were analysed by a GC (Panna A91Plus) with a flame ionisation detector, using a 13X molecular sieve and a Porapak Q column. He gas was used as the GC carrier gas. All products were analysed by the retention times and absorption spectra, using the commercially available standard compounds as references. All products in the reaction mixture were quantified with an

external calibration method. Error bars were estimated based on the standard deviation according to three independent experiments. The apparent quantum yield (AQY) is calculated using AQY = $N_{glycolaldehyde}/N_p$, where $N_{glycolaldehyde}$ is the number of produced glycolaldehyde molecules assuming one glycolaldehyde requires one charge and N_p is the number of incident photons. The conversion of glycerol and the selectivity of glycolaldehyde are defined as follows:

$$\text{Conversion} = \frac{C_{r0} - C_r}{C_{r0}} \times 100\%$$

$$\text{Selectivity} = \frac{0.667C_p}{C_{r0} - C_r} \times 100\%$$

C_{r0} : the initial concentration of the glycerol; C_r : the concentration of the glycerol after the reaction; C_p: the concentration of glycolaldehyde during the reaction.

Scavenger tests were performed by the same procedure with a certain amount of scavengers (e.g. carotene, 4 mg; IPA, 300 mM, 500 μL; SOD, 3 kU/mL, 500 μL; TEOA, 300 mM, 500 μL).

4.3 Results and discussions

4.3.1 Photocatalytic performance

The Ni single atoms decorated TiO_2 was synthesised *via* a modified molten-salt method, in which Ni single atoms were loaded onto the TiO_2 surface in metal salts at an elevated temperature.(*116*) Afterwards, the mixture was washed with a large amount of water to remove the salt residues, which was confirmed by the XPS results (**Figure 13**). Ni single atoms decorated TiO_2 synthesised using the above method is denoted as 0.5Ni/TiO_2-MS (0.5 stands

for the weight percentage of loaded Ni species). As a comparison, the same amount of Ni species was loaded on the TiO_2 surface by a typical impregnation method, which is denoted as 0.5Ni/TiO_2-IM.

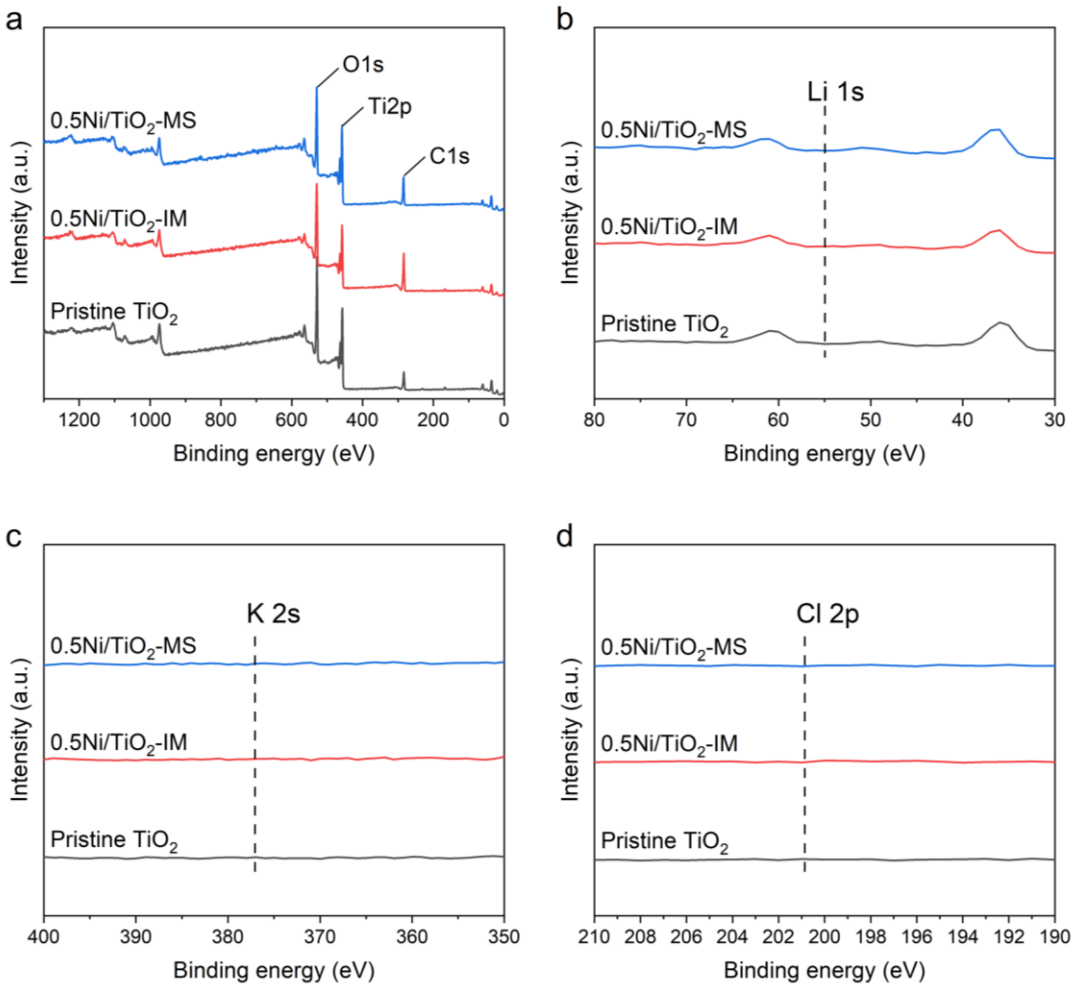

Figure 13. (**a**) XPS survey scan, (**b**) Li 1s, (**c**) K 2s and (**d**) Cl 2p of TiO_2, 0.5Ni/TiO_2-IM and 0.5Ni/TiO_2-MS.

When using these two photocatalysts and pristine TiO_2 for glycerol oxidation under atmospheric air and 365 nm irradiation, a distinctive difference in the glycolaldehyde yield can be observed (**Figure 14a**). Pristine TiO_2 shows a glycolaldehyde evolution rate of 529 $\mu mol \cdot g^{-1} \cdot h^{-1}$, with a small selectivity of 23.9%. It should be noted that the selectivity here is calculated based on the carbon balance instead of the molar amount of produced glycolaldehyde. Since

the glycerol to glycolaldehyde is a C3-to-C2 reaction, its theoretical maximum selectivity is 66.7%. The introduction of Ni species by the impregnation method

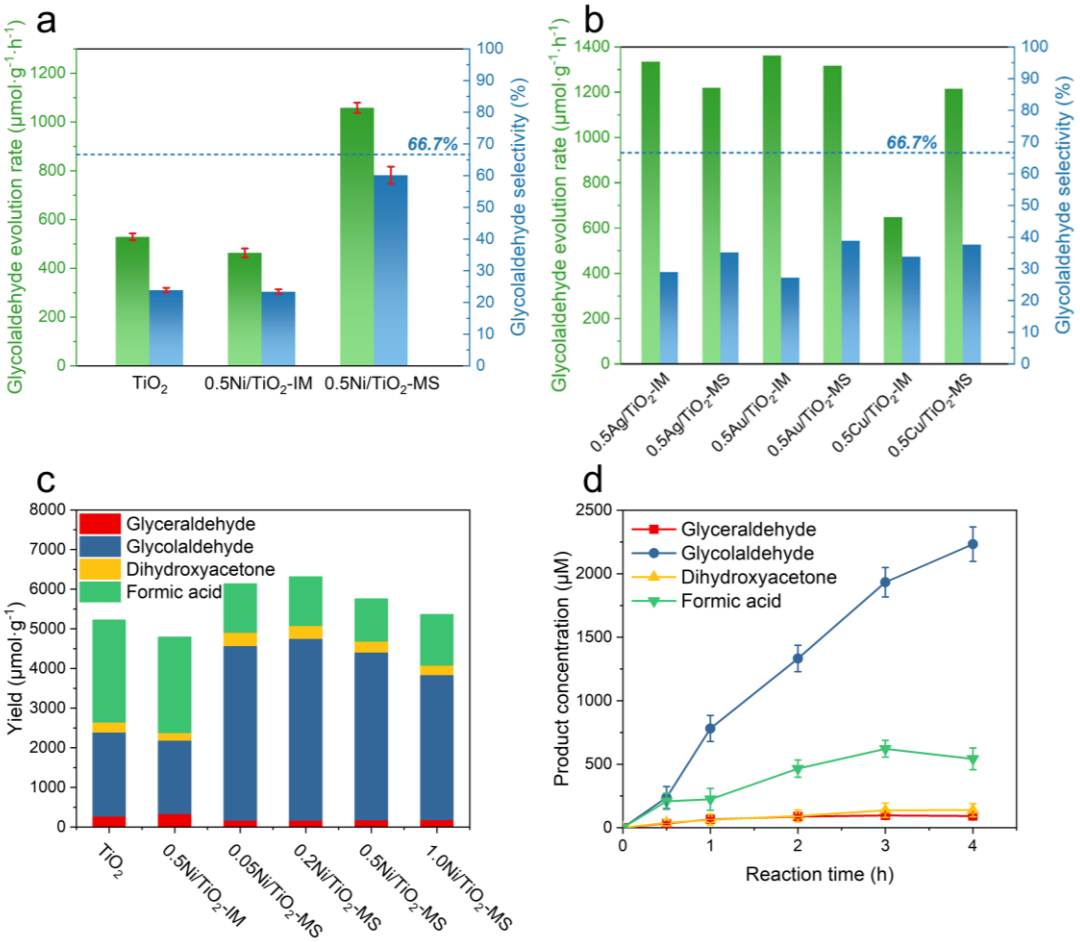

Figure 14. (**a**) The evolution rate and selectivity of glycolaldehyde over TiO_2, 0.5Ni/TiO_2-IM and 0.5Ni/TiO_2-MS. (**b**) The evolution rate and selectivity of glycolaldehyde over metal loaded TiO_2 by impregnation method (IM) or molten-salt method (MS). (**c**) The product distribution over different catalysts. (**d**) The temporal synthesis of different products over 0.5Ni/TiO_2-MS. Reaction conditions: 15 mg catalyst, 30 mL of 25 mM glycerol aqueous solution, 25 °C, air at atmospheric pressure, 365 nm light irradiation, 4h reaction time unless specifically stated otherwise.

has little impact on the selectivity (23.4%), and even somewhat decreases the glycolaldehyde evolution rate (463 $\mu mol \cdot g^{-1} \cdot h^{-1}$). When dispersing Ni species over TiO_2 by the novel molten-salt method, the catalyst presents a 2-fold increase in glycolaldehyde evolution rate (1058 $\mu mol \cdot g^{-1} \cdot h^{-1}$), resulting into an apparent quantum yield of 10.3%, again, two time higher than that achieved on

TiO_2 (AQY = 5.2%). More importantly *c.a.* 2-fold enhancement in selectivity (60.1%) has been achieved on 0.5Ni/TiO_2-MS compared with pristine TiO_2. By

comparison, transition metal species, including Ag, Au and Cu were also loaded on TiO_2 *via* the impregnation method and molten-salt method. Evaluation of the evolution rate and more importantly the selectivity under identical conditions (**Figure 14b**) suggests that Ni can represent the highest selectivity of 60.1%, which is close to the maximum theoretical selectivity (66.7%) to glycolaldehyde, nearly doubling the selectivity achieved on noble metal loaded TiO_2.

The effect of the Ni species loading amount on the catalytic performance was thus further investigated. The metal loading was confirmed by inductively coupled plasma atomic emission spectrometry (ICP-AES) measurements (**Table 1**). Both pristine TiO_2 and 0.5Ni/TiO_2-IM tend to unselectively oxidise glycerol into various products, including formic acid, glycolaldehyde, dihydroxyacetone, and glyceraldehyde (**Figure 14c**), consistent with the previous reports.(*110*) Among them, formic acid accounts for the largest yield, indicating the unselective nature to high value chemicals. When using 0.5Ni/TiO_2-MS, the yield towards glycolaldehyde is greatly enhanced. More importantly, the selectivity to glycolaldehyde increases with the Ni loading amount until 0.5%, such as from 38.6% on 0.05Ni/TiO_2-MS to 60.1% on 0.5Ni/TiO_2-MS. These results indicate that the Ni species loaded by the molten-salt approach play an important role in oxidative C-C bond cleavage of glycerol. Further increasing the loading amount to 1.0% leads to a decreased selectivity to glycolaldehyde (39.1%), which could be owing to the new states formed above the TiO_2 valence band (VB). This shifts the oxidation potential of the

composite system to a higher position compared to the bare surface, weakening the oxidation power of the holes, and thus decreasing the activity.(*2*)

Table 1. Results of ICP-AES analysis on different TiO_2 samples.

Sample	Nominal amount (wt %)	Actual amount (wt %)
0.05Ni/TiO_2-MS	0.05	0.05
0.2Ni/TiO_2-MS	0.2	0.20
0.5Ni/TiO_2-MS	0.5	0.43
1.0Ni/TiO_2-MS	1.0	0.63
0.5Ni/TiO_2-IM	0.5	0.49
0.5Ni/TiO_2-MS-used	0.5	0.38

The temporal production of different products over 0.5Ni/TiO_2-MS was then monitored to understand the oxidation process (**Figure 14d**). Dihydroxyacetone and glyceraldehyde, two C3 products, remain at a low concentration during the whole process likely due to the high conversion to C2 products and formic acid etc (**Figure 15**). They both reach a steady-state concentration after about 3 h reaction, indicating the consumption by consecutive reactions as reported before.(*105*) The yield ratio of glycolaldehyde and formic acid is 1:1 after 0.5 h reaction. However, the subsequent increase of formic acid becomes very slow while glycolaldehyde production keeps its momentum, likely due to the further oxidation of formic acid into CO_2 (**Table 2**). Pristine TiO_2 and 0.5Ni/TiO_2-IM almost show identical product distribution when oxidising glycerol: generating formic acid and glycolaldehyde at a similar rate (**Figure 16a**). Considering the oxidation of formic acid into CO_2 is quite fast over the TiO_2 surface,(*105*) a relatively large amount of CO_2 is detected during this process (**Table 2**).

Meanwhile glycolaldehyde can also be oxidised to CO_2 on TiO_2 or 0.5Ni/TiO_2-IM, while the overoxidation of glycolaldehyde is avoided on 0.5Ni/TiO_2-MS, which induces the large difference on the selectivity.

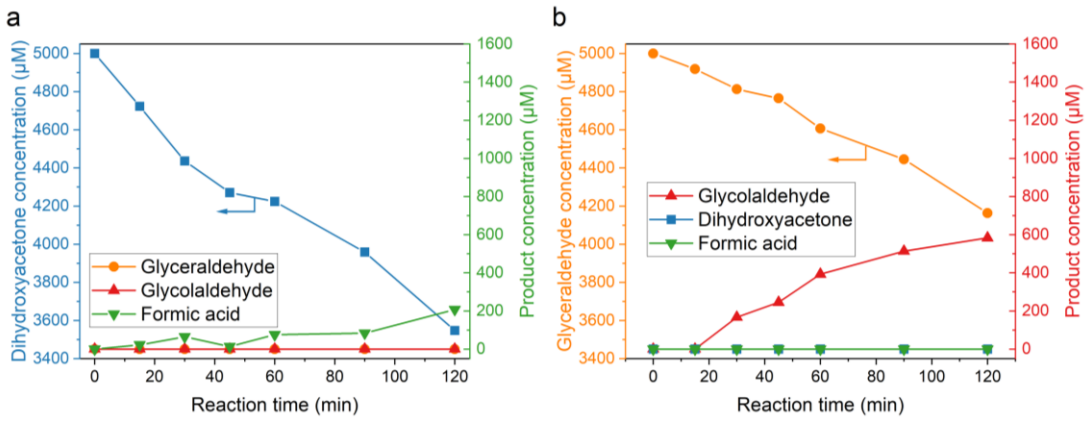

Figure 15. The temporal synthesis of different liquid products over 0.5Ni/TiO_2-MS using (**a**) dihydroxyacetone and (**b**) glyceraldehyde as the substrate. Reaction conditions: 15 mg catalyst, 30 mL of 5 mM dihydroxyacetone or glyceraldehyde aqueous solution, 25 °C, air at atmospheric pressure, 365 nm light irradiation.

Table 2. Results of CO_2 production on different samples.

Sample	CO_2 amount (mmol)
TiO_2	0.106
0.5Ni/TiO_2-IM	0.072
0.5Ni/TiO_2-MS	0.039

Control experiments were then carried out and the results are presented in **Figure 16b**. First, without the presence of air, the 0.5Ni/TiO_2-MS catalyst shows sharply decreased glycolaldehyde yield, highlighting the importance of oxygen in the air for the reaction. Under dark conditions or without a catalyst, no oxidation products can be detected. Hence, it could be confirmed that all the

glycolaldehyde is generated from glycerol oxidation in the presence of light and oxygen over 0.5Ni/TiO_2-MS. In other words, it is unambiguous that the photocatalysis process over 0.5Ni/TiO_2-MS is the only contributor to glycerol oxidation. **Figure 16c** presents the stability of the best 0.5Ni/TiO_2-MS catalyst. The catalyst shows a similar glycolaldehyde yield and selectivity across eight 4h-runs, indicating the excellent stability of the catalyst during the C-C cleavage reaction.

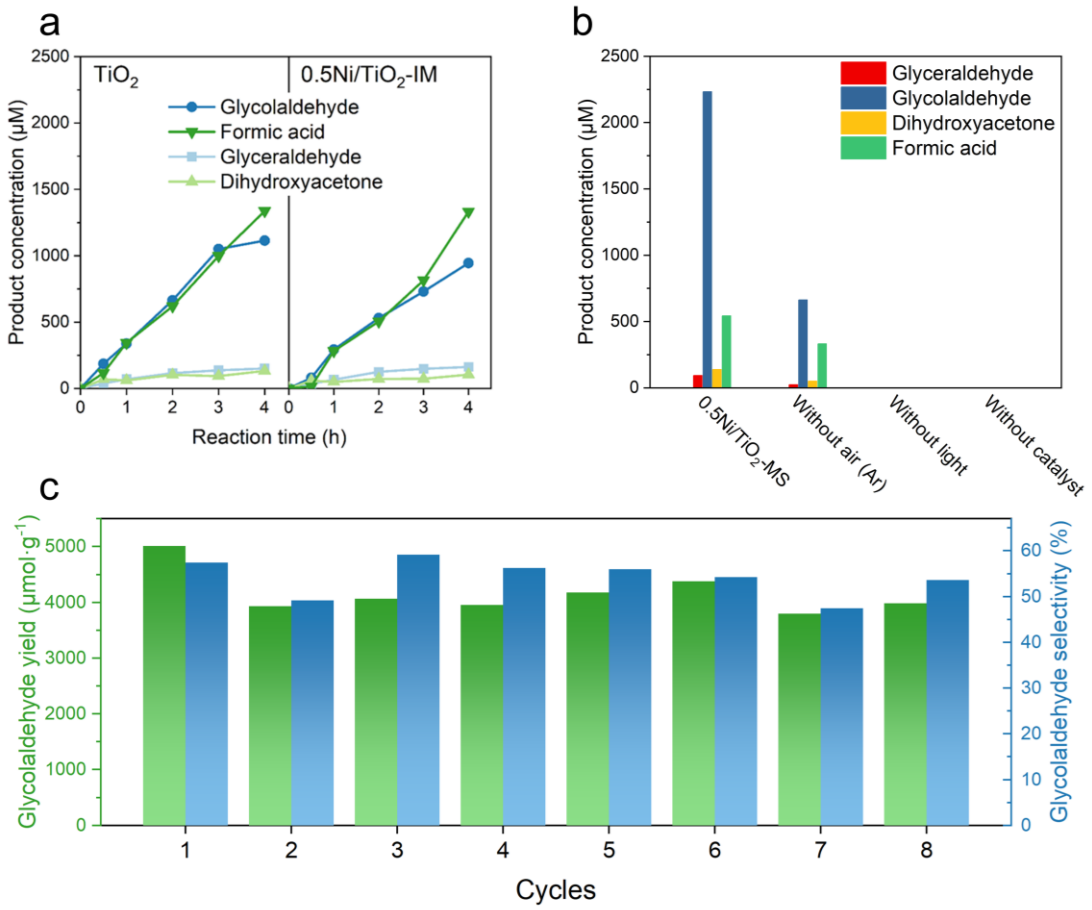

Figure 16. (**a**) The corresponding production profile on TiO_2 and 0.5Ni/TiO_2-IM catalysts. (**b**) Product yields from a series of control experiments. (**c**) Stability test of 0.5Ni/TiO_2-MS for 8 cycles reaction.

4.3.2 Photocatalyst characterisation

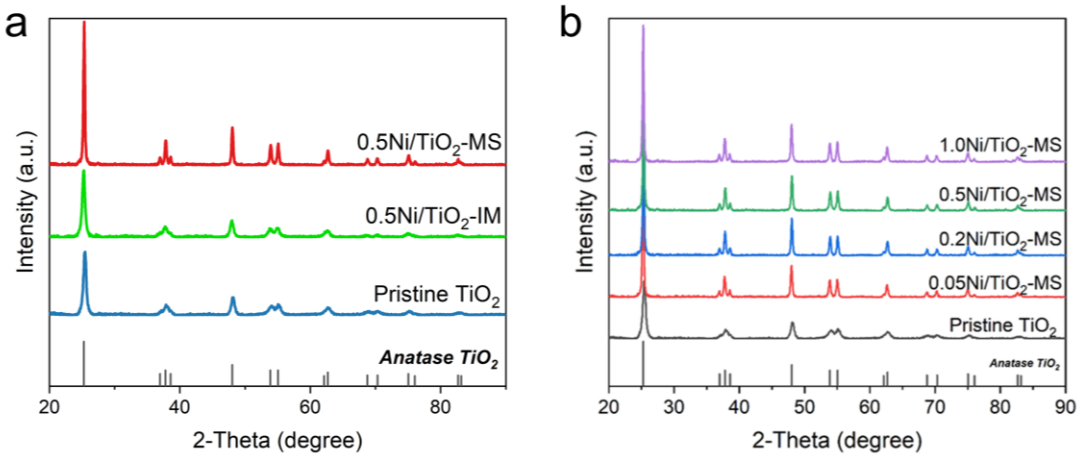

Figure 17. (**a**) XRD patterns of TiO_2, 0.5Ni/TiO_2-IM and 0.5Ni/TiO_2-MS. (**b**) XRD results of Ni/TiO_2-MS with different Ni loading amount.

To reveal the mechanism behind the high selectivity to glycolaldehyde over 0.5Ni/TiO_2-MS, the crystal structure, morphology, and light-harvesting property of these samples were studied. XRD patterns of 0.5Ni/TiO_2-IM show little difference compared with pristine TiO_2, and no new peak appears after the impregnation of Ni species due to its low loading amount (**Figure 17a**). For 0.5Ni/TiO_2-MS the sharpened XRD peaks indicate that an enhanced crystallinity of TiO_2 is achieved during the molten-salt treatment. This is because a higher temperature (500 °C) was used in the molten-salt method compared with 400 °C in the impregnation method.(*116*) To rule out the effect of crystallinity on the product distribution, 0.5Ni/TiO_2-IM was also annealed at 500 °C under argon atmosphere for two hours, no obvious catalytic performance change is observed (**Table 3**). Thus, the enhanced selectivity to glycolaldehyde is not because of the improved crystallinity. XRD patterns of molten-salt prepared samples do not show any reflections of metallic or oxide Ni species even increasing the loading amount to 1.0%, indicating that the

metal species are highly dispersed over the surface of TiO_2 by this novel method (**Figure 17b**).

Table 3. Oxidation products comparation between 0.5Ni/TiO_2-IM and the sample after annealing at 500 °C for 2 hours (0.5Ni/TiO_2-IM-A500).

Sample	Glyceraldehyde (μM)	Glycolaldehyde (μM)	Dihydroxyacetone (μM)	Formic acid (μM)
0.5Ni/TiO_2-IM	160	950	100	1330
0.5Ni/TiO_2-IM-A500	130	940	110	1310

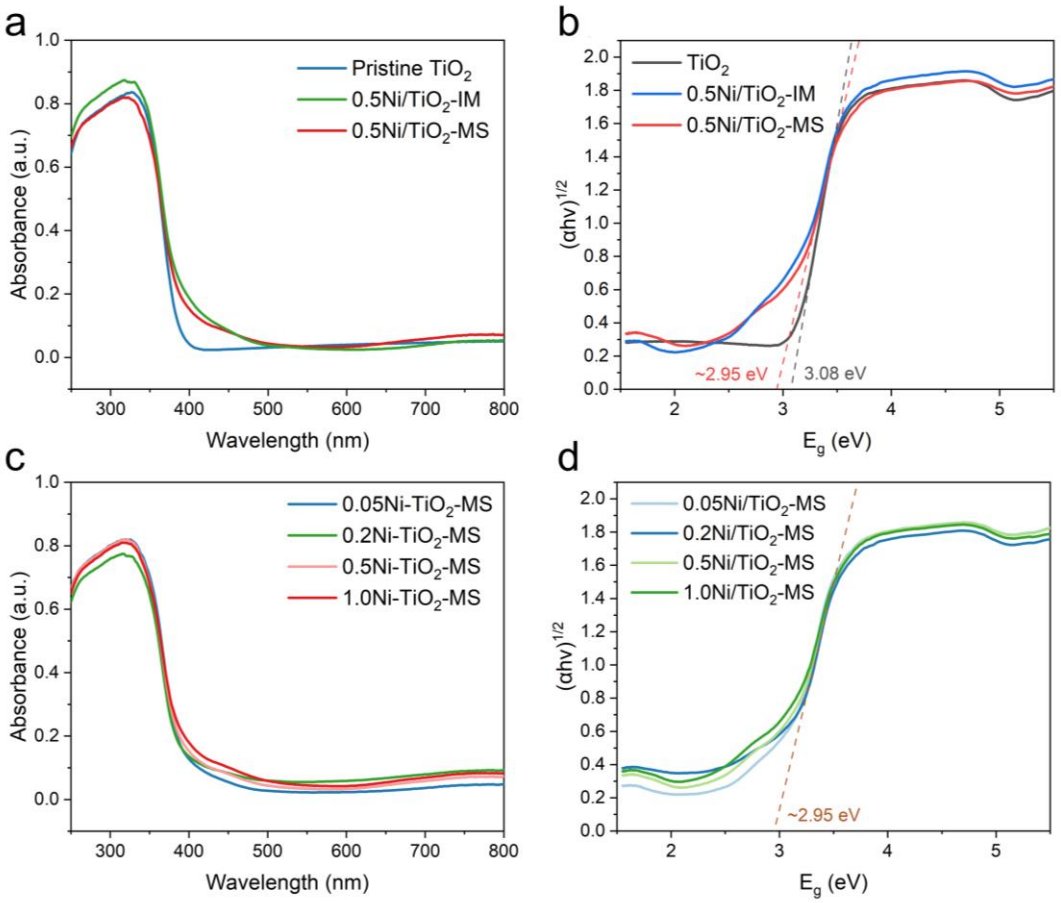

Figure 18. (**a**) UV-Vis spectra and (**b**) Tauc-Plot curves of TiO_2, 0.5Ni/TiO_2-IM and 0.5Ni/TiO_2-MS. (**c**) UV-Vis spectra and (**d**) Tauc-Plot curves of Ni/TiO_2-MS with different Ni loading amounts.

The UV−vis spectra (**Figure 18a**) of the prepared samples present the characteristic absorption band with an onset edge at around 366 nm, indicating a bandgap of about 3 eV, consistent with the widely reported value (**Figure 18b**).(*117*) The loading of Ni species by impregnation or molten-salt method has no obvious effect on the onset edge of the samples, besides leading to a slight absorption in the visible-light region (**Figure 18a** and **Figure 18c, d**), which should not affect the photocatalytic activity due to a 365 nm light source being used for excitation. Combining with the XPS valence band spectra (**Figure 19**), in which all samples show a similar valence band of 2.7 eV, loading Ni either by impregnation or molten-salt method does not change the band edge positions of photocatalysts.

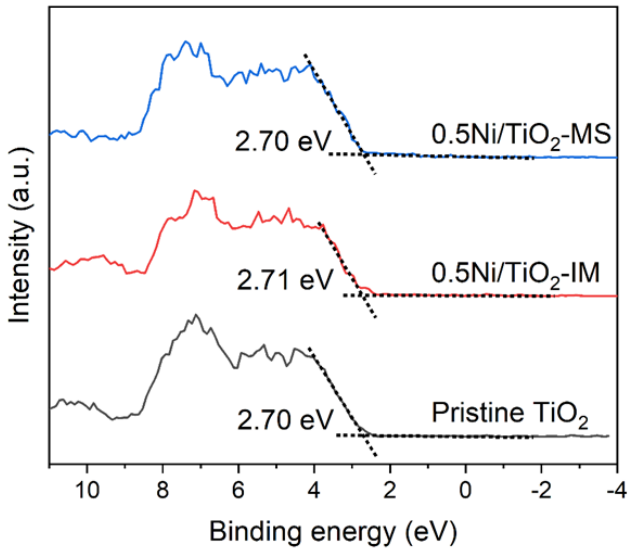

Figure 19. XPS valence band spectra of TiO_2, 0.5Ni/TiO_2-IM and 0.5Ni/TiO_2-MS.

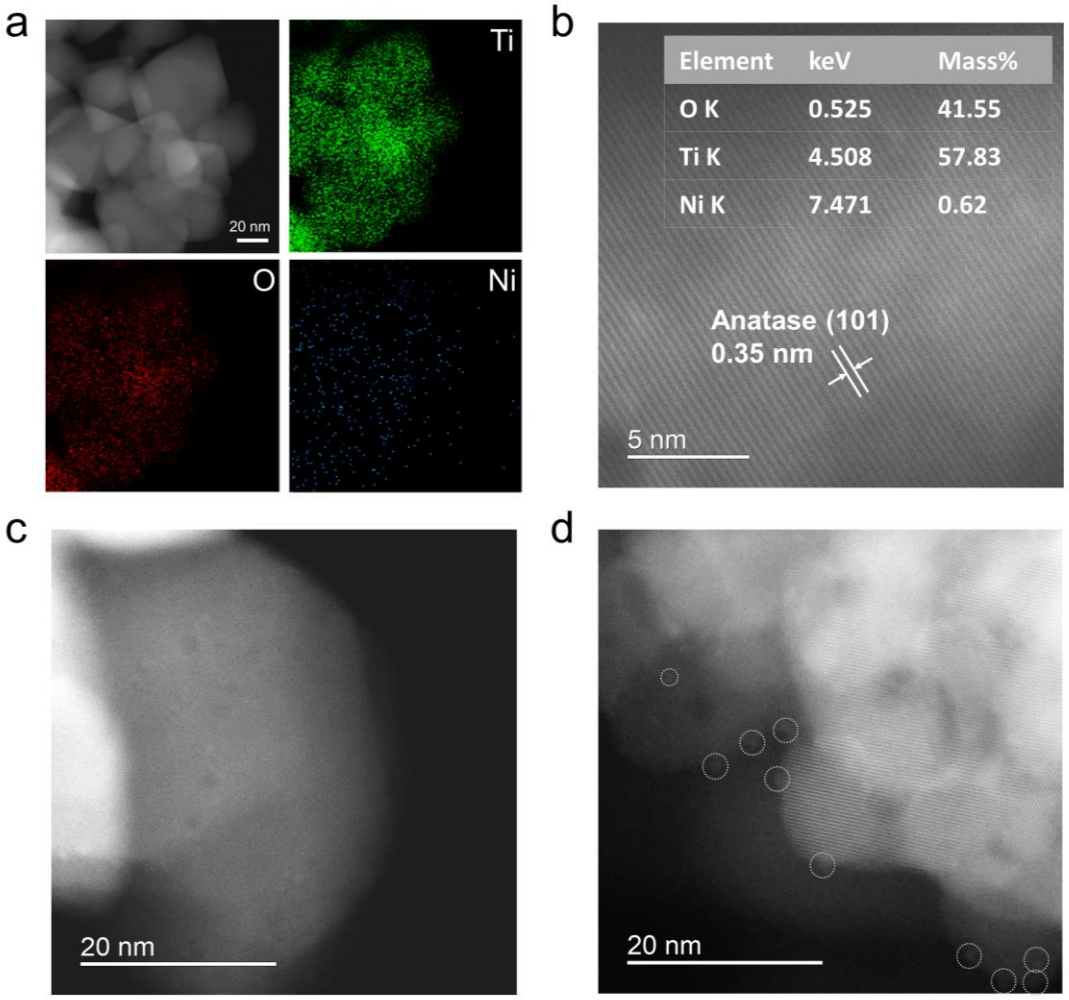

Figure 20. (**a**) TEM image of 0.5Ni/TiO_2-MS and the corresponding EDX elemental mapping. (**b**) HAADF-AC-STEM images of 0.5Ni/TiO_2-MS and the corresponding EDX results. (**c**) HAADF-AC-STEM images of 0.5Ni/TiO_2-MS and (**d**) 0.5Ni/TiO_2-IM. The NiO_x nanoparticles over 0.5Ni/TiO_2-IM are marked by grey dotted circles.

The morphology of 0.5Ni/TiO_2-MS was first investigated by transmission electron microscopy (TEM), as shown in **Figure 20a**. The TiO_2 nanoparticles have an average diameter of around 60 nm. There are no obvious particles on 0.5Ni/TiO_2-MS, while EDX mapping shows a homogeneous distribution of nickel species. This indicates that Ni species may atomically disperse on the TiO_2 surface. To confirm this hypothesis, sub-Ångström-resolution high-angle annular dark-field scanning transmission electron microscopy (HAADF-STEM)

technique was then employed to probe the highly dispersed Ni-containing species (**Figure 20b**), no clusters or nanoparticles can be seen on 0.5Ni/TiO_2-MS sample. Though no bright dots could be distinguished from the STEM image due to low contrast between Ni and Ti,(*116, 118*) EDX scanning shows 0.62% of nickel on the scanned area, which is close to the actual amount (0.43%). This strongly suggests the presence of atomically dispersed Ni atoms on the surface of TiO_2. On the contrary, nanoparticles (likely NiO) with an average diameter of cal. 1.2 nm are formed when using the impregnation method to load Ni species (**Figure 20c, d**).

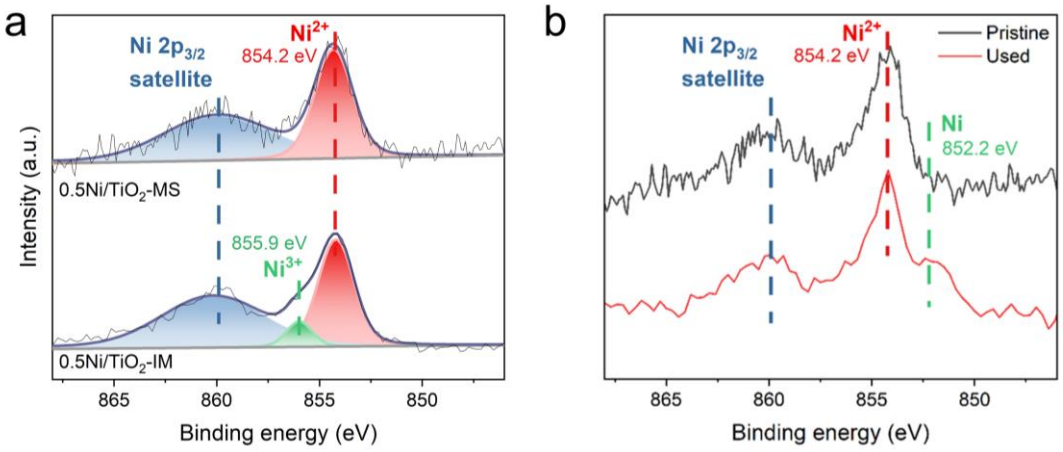

Figure 21. (**a**) Ni $2p_{3/2}$ XPS spectra of 0.5Ni/TiO_2-IM and 0.5Ni/TiO_2-MS. (**b**) Ni $2p_{3/2}$ XPS spectra of pristine 0.5Ni/TiO_2-MS and 0.5Ni/TiO_2-MS after eight 4h-runs.

For a deeper understanding of the mechanism behind the high selectivity to glycolaldehyde over 0.5Ni/TiO_2-MS, the chemical states of nickel species were characterised by XPS (**Figure 21a**). The peak located at around 854 eV is associated with the nickel $2p_{3/2}$,(*119*) and the typical Ni $2p_{3/2}$ satellite peak is present.(*120*) In 0.5Ni/TiO_2-IM, Ni $2p_{3/2}$ is dominated by the peak at 854.2 eV, which corresponds to Ni^{2+}, and there is a minor peak at 855.9 eV, which is

ascribed to Ni^{3+}. The formation of Ni^{3+} on 0.5Ni/TiO_2-IM is likely due to the oxidative environment in air under 400 °C during the impregnation process. Thus, the nanoparticles on 0.5Ni/TiO_2-IM could be identified as NiO_x (mixing Ni^{2+} and Ni^{3+}). For 0.5Ni/TiO_2-MS, the Ni $2p_{3/2}$ peak indicates that the chemical state of Ni species is mainly +2 (854.2 eV), which is well-maintained even after the 32 h run (**Figure 21b**).(*121*) Therefore, it could be confirmed that different loading methods lead to different Ni species: the novel molten salt method forms single atoms Ni^{2+} while the impregnation method generates NiO_x nanoparticles on the TiO_2 surface.

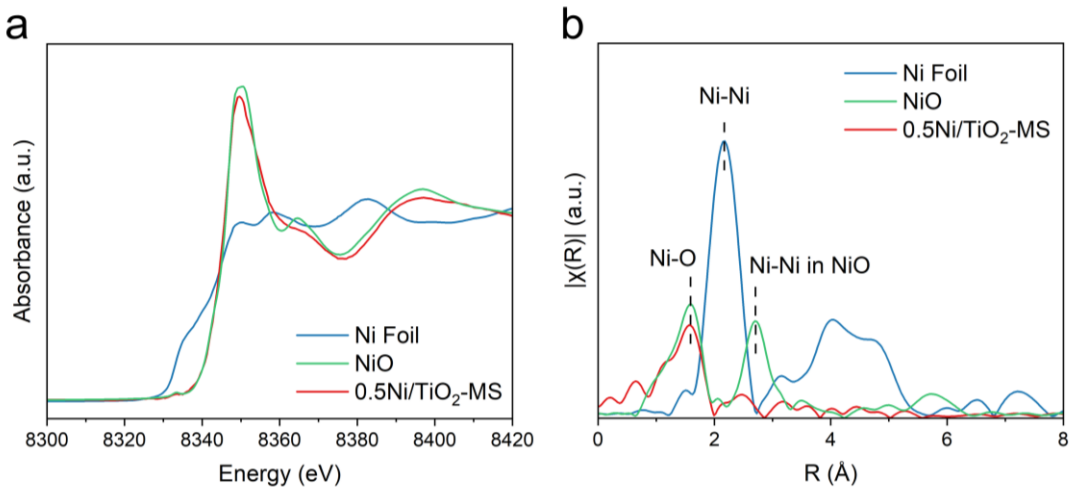

Figure 22. (**a**) Nickel K-edge XANES results of nickel (metal), NiO 0.5Ni/TiO_2-IM, and 0.5Ni/TiO_2-MS. (**b**) Fitting details for nickel K-edge EXAFS spectra of 0.5Ni/TiO_2-MS.

The chemical state of the nickel species over 0.5Ni/TiO_2-MS was further confirmed by X-ray absorption near-edge structure (XANES) spectroscopies (**Figure 22a**). The E_0 for 0.5Ni/TiO_2-MS is close to that of NiO, suggesting Ni atoms carry positive charges of +2. The coordination environment of Ni single atoms is determined by the extended X-ray absorption fine structure spectra (EXAFS). As shown in the Fourier-transformed k^2 weighted EXAFS spectra at

the Ni K-edge (**Figure 22b**), in contrast to the reference samples of Ni foil and NiO, the 0.5Ni/TiO_2-MS catalyst does not show any prominent peaks at the positions of either Ni–Ni shell (2.2 Å) or Ni–O–Ni (2.7 Å) shell, excluding the existence of metallic Ni or NiO_x nanoparticles.(*116*)

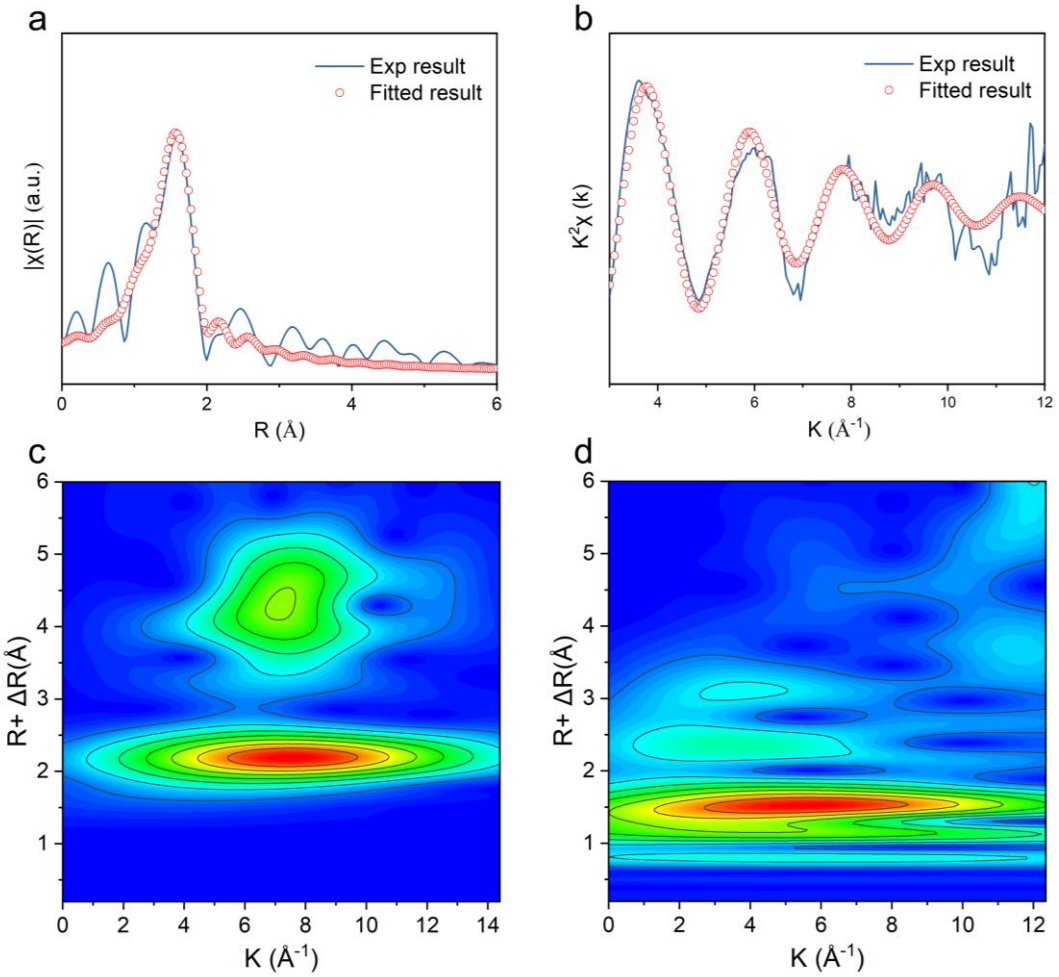

Figure 23. (**a**) EXAFS fitting curve for the nickel K-edge EXAFS spectra of 0.5Ni/TiO_2-MS in the region of 0-6.0 Å, shown in k^2 weighted *R*-space. (**b**) Ni K-edge EXAFS fit for the nickel K-edge EXAFS spectra of 0.5Ni/TiO_2-MS in the region of 3.0-12.0 $Å^{-1}$, shown in k^2 weighted *k*-space. Wavelet Transformation for the k^2-weighted EXAFS signal of (**c**) Ni foil and (**d**) 0.5Ni/TiO_2-MS.

The absence of Ni–Ni scattering is further verified by the wavelet transform (WT) technique. As shown in **Figure 23**, the absence of the lobe at high k value in 0.5Ni/TiO_2-MS indicates the central Ni does not bind to any heavy atoms (e.g.

Ni). On the contrary, there is a lobe at low k value (1.5 Å, 5.5 $Å^{-1}$), which can be ascribed to the Ni–O coordination.(*122, 123*) The EXAFS data-fitting results (**Table 4**) show that the Ni–O coordination number is 5.2, suggesting the NiO_5 entities are selectively fabricated. Combining with these XANES data, it could be confirmed the oxidised state of Ni species are atomically dispersed over TiO_2, consistent with the HAADF-AC-STEM images. To rule out the contribution of the possibly-existed tiny NiO nanoparticles to the catalytic performance, 0.5Ni/TiO_2-MS sample was washed with 1 M HCl solution.(*124*) There is little performance change for 0.5Ni/TiO_2-MS, indicating the contribution of NiO nanoparticles is insignificant during the glycerol oxidation (**Figure 24**).

Table 4. The best-fitted Nickel K-edge EXAFS results of 0.5Ni/TiO_2-MS.

Sample	Shell	CN	R (Å)	σ^2 (10^{-2} $Å^2$)	ΔE_0 (eV)	r-factor (%)
Ni foil	Ni-Ni	12	2.48	0.5	4.7	0.07
0.5Ni/TiO_2-MS	Ni-O	5.2	2.05	0.6	-7.2	0.7

CN is the coordination number for the absorber-back scatterer pair, R is the average absorber-back scatterer distance, σ^2 is the Debye-Waller factor, and ΔE_0 is the inner potential correction. The accuracies of the above parameters are estimated as CN, ±20%; R, ±1%; σ^2, ± 20%; ΔE_0, ±20%. The data range used for data fitting in k-space (Δk) and R-space (ΔR) are 3.0-11.0 $Å^{-1}$ and 1.0-2.0 Å, respectively.

To further elaborate the selectivity difference caused by NiO_x nanoparticles and Ni single atoms on the photocatalyst, high-resolution O 1s XPS spectra were then recorded (**Figure 25**). There are two peaks in the O 1s core-level: one peak at 529.5 eV is assigned to the lattice oxygen (O_L) from Ti-O-Ti, while the other one located at 531.3 eV should be attributed to oxygen vacancy (O_V).(*125*) The O_V/O_L ratio in 0.5Ni/TiO_2-IM is 46/54, which is higher than that

in pristine TiO_2 (34/66). On the contrary, 0.5Ni/TiO_2-MS sample shows a decreased content of oxygen vacancies (23/77). This is likely because of the rearrangement of atoms during molten-salt treatment and is consistent with the enhanced crystallinity evidenced by XRD patterns.

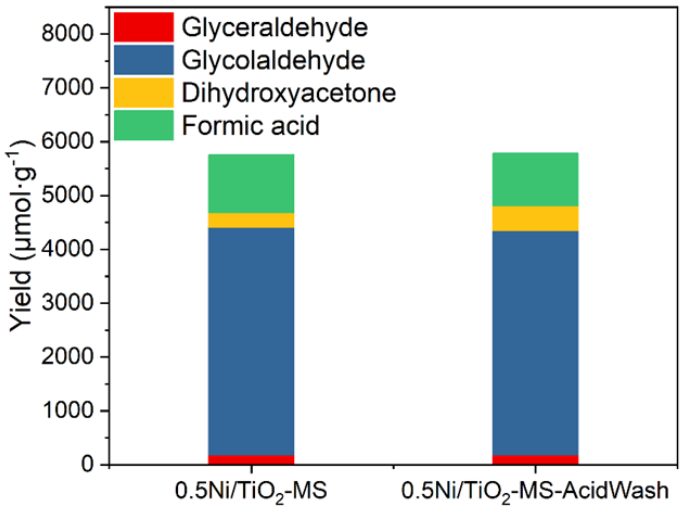

Figure 24. The product distribution over 0.5Ni/TiO_2-MS and 0.5Ni/TiO_2-MS after acid washing.

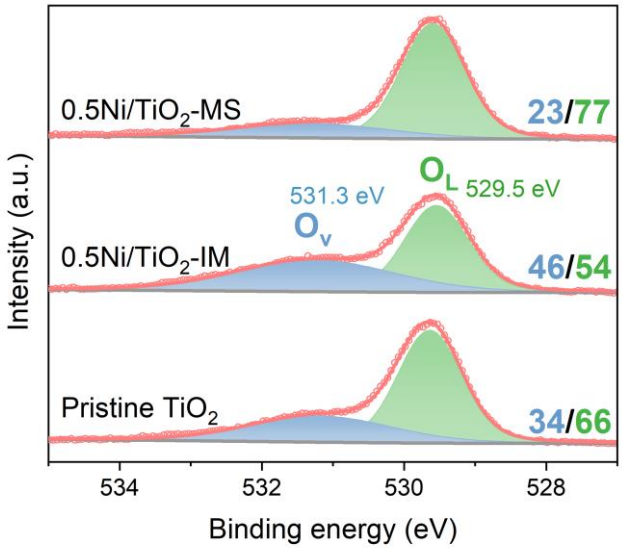

Figure 25. O1s XPS results of TiO_2, 0.5Ni/TiO_2-IM and 0.5Ni/TiO_2-MS.

4.3.3 Mechanism analysis

Heterogeneous photocatalytic reactions involve three consecutive steps, beginning with the adsorption of the reactants, then the charge generation and transfer, and lastly the surface reaction and product desorption. Next is to attempt to explore these steps to clarify the function of Ni single atoms. Control experiments prove that oxygen is the major oxidant in glycerol C-C cleavage reaction, it is thus of vital importance to clarify the oxygen adsorption behaviour over different catalysts. **Figure 26** presents the patterns of temperature-programmed desorption of oxygen (O_2-TPD) recorded on these samples. Two desorption peaks are observed in pristine TiO_2: the first one is located at 70 °C, which can be assigned to physically-adsorbed O_2, and the second one is around 150-250 °C, corresponding to chemically-bonded molecular oxygen on oxygen vacancies.(*126*) O_2-TPD pattern of 0.5Ni/TiO_2-IM presents a similar peak at 150-250 °C with a larger peak area of 1.387 compared with that of pristine TiO_2 (1.154). This trend is consistent with the increased oxygen vacancy amount evidenced by XPS results. As no new peak appears on the 0.5Ni/TiO_2-IM O_2-TPD patterns, it is reasonable to deduce that NiO_x nanoparticles are not able to serve as O_2 adsorption sites, which is consistent with previous reports.(*127*) For 0.5Ni/TiO_2-MS, the major desorption peak shifts to a lower temperature (70-200°C), suggesting the emergence of different oxygen adsorption sites formed on the surface. Considering the decreased oxygen vacancy amount, the only feasible adsorption sites of oxygen on the surface of 0.5Ni/TiO_2-MS are the single Ni atoms.(*128*) The left-shifted desorption peak suggests a lower oxygen adsorption energy of single Ni atoms compared with that of oxygen vacancies, such a trend is in agreement with

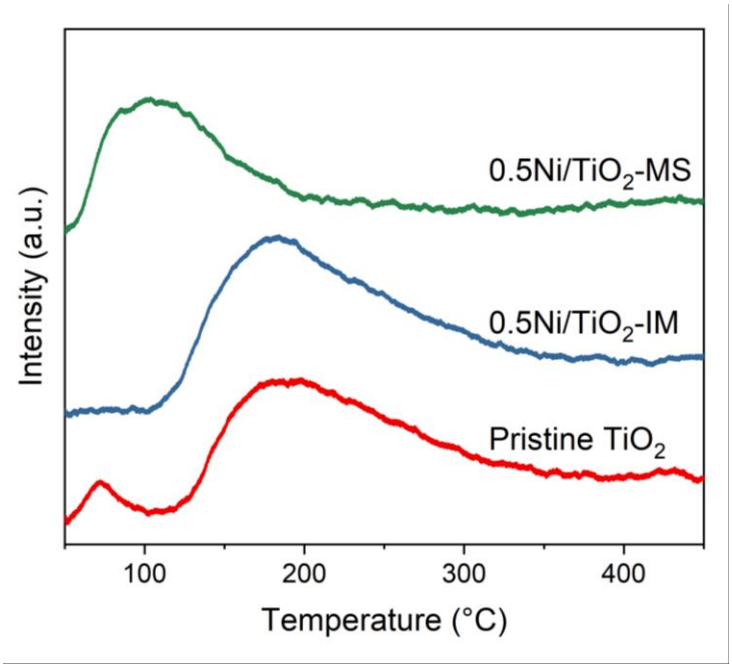

Figure 26. O_2-TPD of TiO_2, 0.5Ni/TiO_2-IM and 0.5Ni/TiO_2-MS.

reported values (20 meV for Ni single atoms and 47 meV for oxygen vacancies over TiO_2).(*129, 130*)

Following O_2 adsorption, the next vital step for glycerol oxidation is the charge transfer and activation of O_2. To this end, high-resolution *in-situ* Ti 2p XPS spectra of 0.5Ni/TiO_2-MS were measured under dark and UV light conditions (**Figure 27**). The unchanged Ti 2p spectra indicate that the chemical states of Ti species in the TiO_2 support remain unchanged under UV irradiation. Then, Ni K-edge XANES spectra were performed under *operando* conditions to clarify the transport path of photogenerated electrons (**Figure 28a**). By using such *operando* conditions, the possible misinformation caused by the reductive environment on such a tiny amount of Ni created by high-vacuum circumstances when conducting XPS measurement could be avoided.

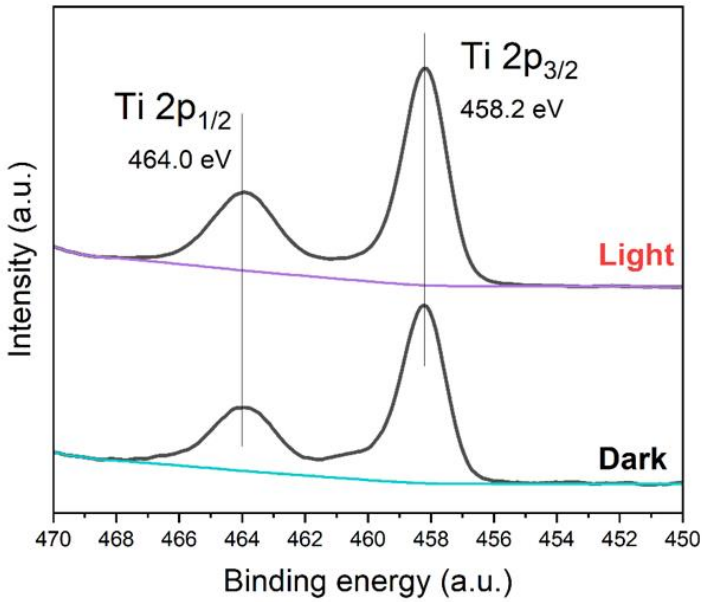

Figure 27. High-resolution *in-situ* Ti 2p XPS spectra of 0.5Ni/TiO_2-MS under dark and UV light conditions. Ti 2p XPS signals are observed at 458.2 and 464.0 eV, assigned to Ti $2p_{3/2}$ and Ti $2p_{1/2}$ respectively, which well correspond to the Ti^{4+} species in TiO_2.(*131*) Switching on the UV irradiation does not lead to any change in the Ti 2p spectra, consistent with the previous studies.(*132*)

When the incident X-ray has an energy equal to that of the binding energy of a Ni core-level electron, there would be a sharp rise in absorption: an absorption edge corresponding to the promotion of this core level to the continuum. The position of this absorption edge can be reliably used to determine oxidation states. The more left the absorption edge, the lower the oxidation state (**Figure 28b**). For a clearer presentation of this position change, **Figure 28c** displays the derivative *operando* Ni K-edge XANES spectra. As shown, there is no change in the spectrum of 0.5Ni/TiO_2-IM whether the light irradiation is on or not. This means the electron states of NiO_x species do not change during the whole process. For 0.5Ni/TiO_2-MS under the dark condition, in either air atmosphere or glycerol it shows the same position of the Ni K-edge, while approximately 0.5 eV shift to the lower energy is observed under light

condition. Once the light irradiation stops, the Ni K-edge returns to its original state. This indicates a decrease in the Ni oxidation state, which ought to result from the acceptation of the photogenerated electrons from the TiO_2 support.

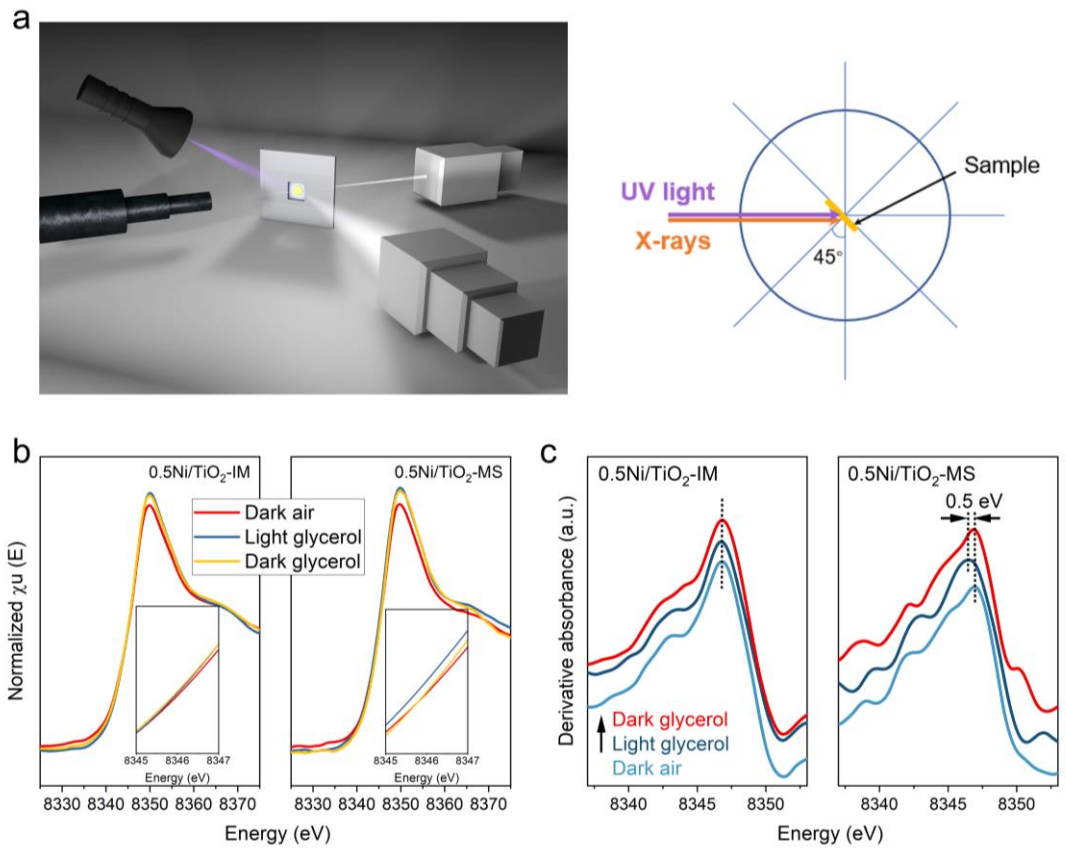

Figure 28. (**a**) Schematic illustration of *operando* XANES setup. The photocatalyst was fixed in the centre of a reaction cell and immersed in the glycerol solution. Both ends of the cell were sealed up by X-ray transparent tape, so the dynamic change of the catalyst under its actual working condition could be observed. (**b**) *Operando* XANES results of 0.5Ni/TiO_2-IM and 0.5Ni/TiO_2-MS under different conditions. (**c**) Derivative data of *operando* Ni K-edge XANES results of 0.5Ni/TiO_2-IM and 0.5Ni/TiO_2-MS under different conditions.

The above result shows that the NiO_x nanoparticles on 0.5Ni/TiO_2-IM cannot either receive or donate electrons under light irradiation, while the Ni single atoms can serve as electron acceptors. This is rather understandable because for 0.5Ni/TiO_2-IM, as a part of the Ni^{2+} ions are oxidised to Ni^{3+}, some Ni^{2+} ions

diffuse to the surface to maintain the charge balance, thus leaving holes inside of NiO_x and making it a p-type semiconductor.(*133*) Since TiO_2 is a typical n-type semiconductor, a p-n junction can be formed on the interface between NiO_x and TiO_2. Electrons cannot pass through this junction from TiO_2 to NiO_x due to their band alignment (**Figure 29**), so NiO_x cannot act as an electron acceptor.(*134*) Furthermore, when using UV light to excite NiO_x-loaded TiO_2, little light can be harvested by NiO_x due to the large light absorption coefficient of TiO_2 in the UV region and the small amount of NiO_x loaded.(*135*) Therefore there is no Ni K-edge shift observed. On the contrary, Ni single atoms form energy levels other than a band. DFT simulations have revealed the special electronic structures when loading Ni single atoms on anatase TiO_2. Such new energy levels are composed of vacant levels generated near the conduction band minimum of TiO_2.(*2*) The excited electrons in the TiO_2 conduction band

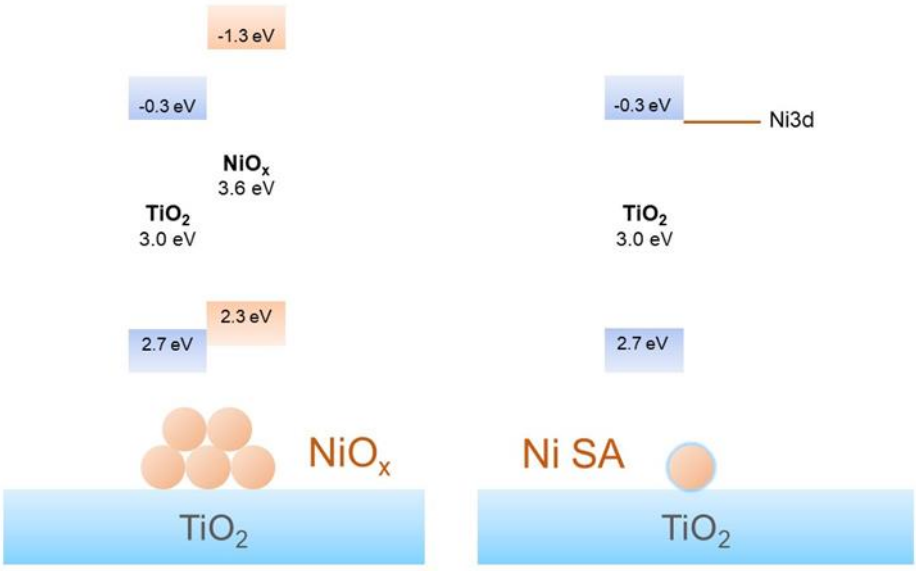

Figure 29. Energy band diagrams for Ni species modified anatase TiO_2 (left: 0.5Ni/TiO_2-IM; right: 0.5Ni/TiO_2-MS.(*1, 2*) NiO_x is a p-type semiconductor while Ni single atom (Ni SA) only forms an energy level other than a band.

can be transferred to the vacant energy level in Ni single atoms, which are further transferred to adsorbed O_2.(*136*) The chemically adsorbed O_2 molecules on Ni single atoms indicated by O_2-TPD observation can then be reduced by the electrons, forming reactive $O_2^{\bullet-}$ to involve in the subsequent reaction as discussed below.

As one of the most direct inspection techniques, electron spin resonance (ESR) spectroscopy was further employed to detect the generated ROS ($^1O_2$, $O_2^{\bullet-}$ and •OH) over different catalysts. Two trapping agents, 2,2,6,6-tetramethylpiperidine (TEMP) and 5,5-dimethyl-1-pyrroline-N-oxide (DMPO), were selected for $^1O_2$ and •OH and $O_2^{\bullet-}$ detection. As illustrated in **Figure 30a**, weak 1:1:1 triplet signals are observed under light illumination over both 0.5Ni/TiO_2-IM and 0.5Ni/TiO_2-MS, in accordance with that of 2,2,6,6-tetramethylpiperidine-N-oxyl (TEMPO), which verifies a small amount generation of $^1O_2$. In the presence of DMPO in methanol, no obvious signal could be detected over 0.5Ni/TiO_2-IM, while a signal associated with DMPO−OOH, a spin derivative of DMPO−$O_2^{\bullet-}$, is observed on 0.5Ni/TiO_2-MS, confirming that a large amount of $O_2^{\bullet-}$ is generated (**Figure 30b**). In the presence of DMPO in water, a weak 1:2:2:1 quartet signal assigned to DMPO-OH is detected over 0.5Ni/TiO_2-IM, while a strong signal is observed over 0.5Ni/TiO_2-MS under light irradiation, suggesting the facile generation of •OH (**Figure 30c**). In conclusion, the enhanced separation and transfer processes of charge carriers, together with the facile oxygen adsorption over single Ni atoms, lead to high-efficiency $O_2^{\bullet-}$ generation, accompanied by •OH radicals due to the reaction between photoholes and water.

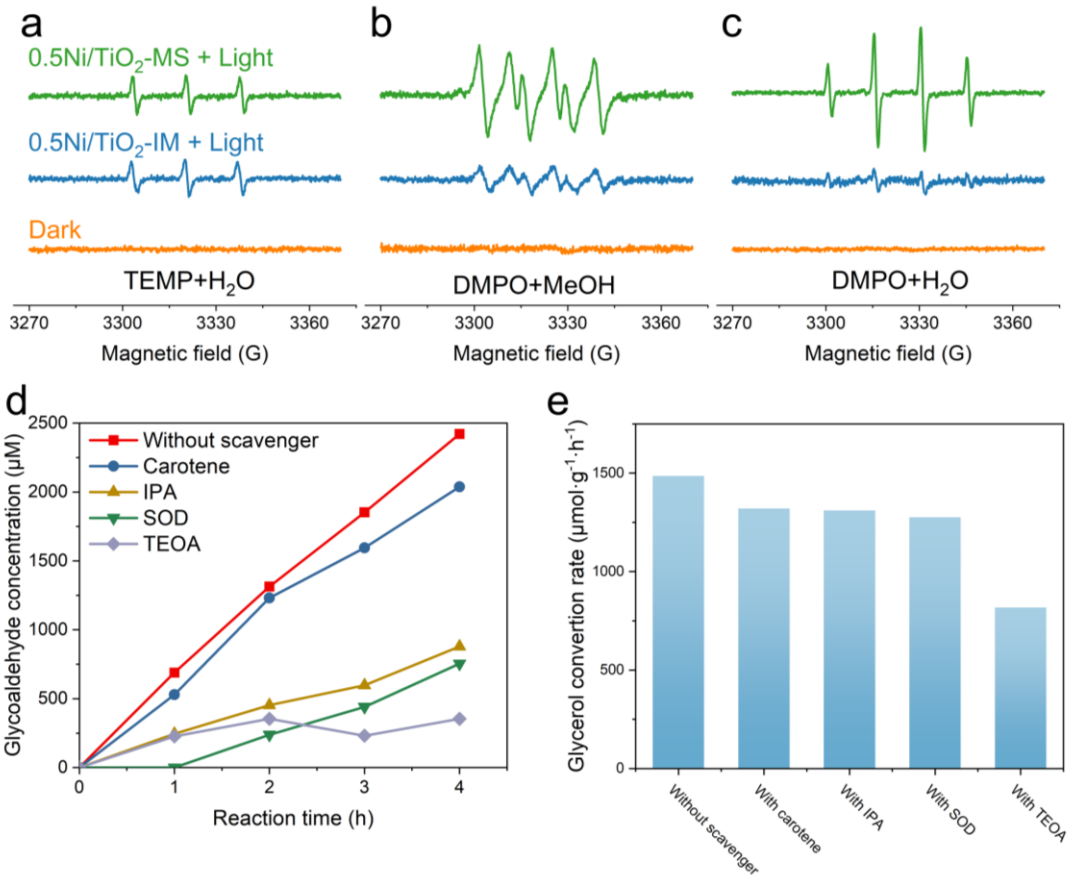

Figure 30. (**a**) ESR spectra for the detection of $^1O_2$ on 0.5Ni/TiO_2-IM and 0.5Ni/TiO_2-MS under air in 2,2,6,6-tetramethylpiperidine (TEMP) aqueous solution. (**b**) ESR spectra under air for the detection of $O_2^{\bullet-}$ on 0.5Ni/TiO_2-IM and 0.5Ni/TiO_2-MS. (**c**) ESR spectra under air for the detection of •OH on 0.5Ni/TiO_2-IM and 0.5Ni/TiO_2-MS. (**d**) Glycolaldehyde yield of glycerol oxidation on 0.5Ni/TiO_2-MS with different scavengers. (**e**) Effect of different scavengers on glycerol conversion rate on 0.5Ni/TiO_2-IM.

Given that several reactive species, including photogenerated holes (h^+), superoxide ($O_2^{\bullet-}$), hydroxyl radicals (•OH), and singlet oxygen ($^1O_2$), could be involved in the glycerol oxidation process, identifying the function of each reactive species is crucial. To this end, triethanolamine (TEOA), superoxide dismutase (SOD), isopropyl alcohol (IPA), and carotene were selected as the scavengers for h^+, $O_2^{\bullet-}$, •OH, and $^1O_2$, respectively. As shown in **Figure 30d**, TEOA, SOD, and IPA are found to effectively inhibit glycolaldehyde generation, whereas carotene turns out little effect on the oxidation rate. Considering the

generation of •OH relies on photogenerated holes, the formation of glycolaldehyde should be completed by the cooperative work of superoxide radicals ($O_2^{\bullet-}$) and hydroxyl radicals (•OH). For the sample prepared by the impregnation method, only TEOA relatively decreases its conversion rate (**Figure 30e**), thus the unselective oxidation of glycerol over 0.5Ni/TiO_2-IM should be attributed to the photogenerated holes. On the other hand, a similar $^1O_2$ species amount exists on both samples (**Figure 30a**) while it does not have a significant effect on the reaction rate. All these results highlight the importance of the cooperation between superoxide radicals and hydroxyl radicals during glycerol selective C-C cleavage reaction, which can only be enhanced by Ni single atoms for the selective production of glycolaldehyde.

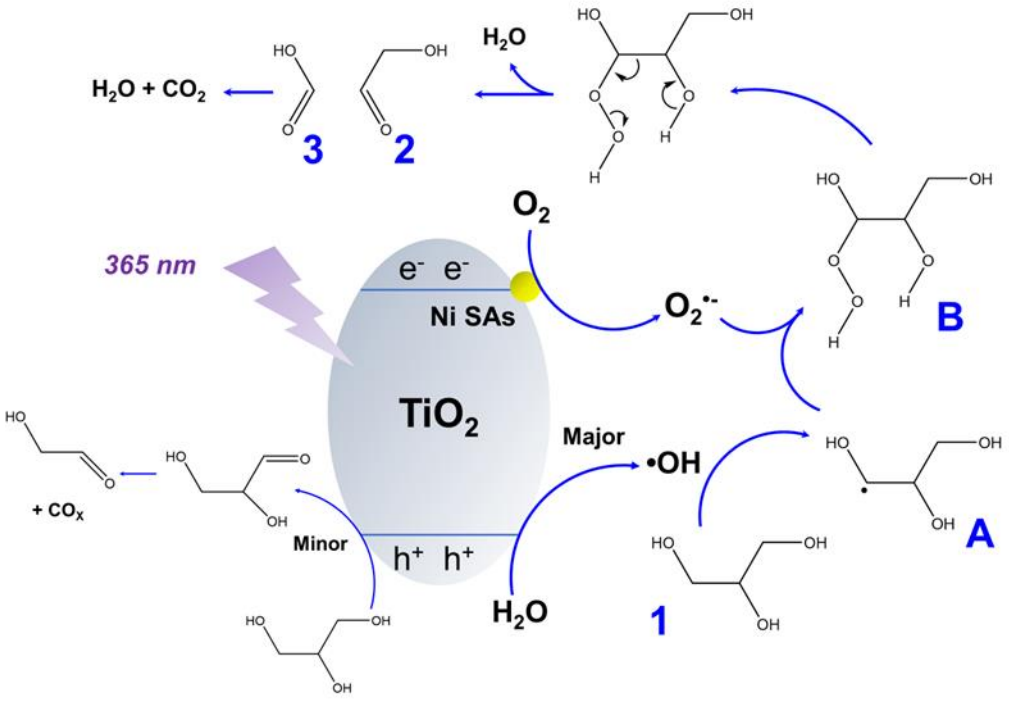

Figure 31. Proposed reaction mechanism of glycerol oxidation on Ni single atom decorated TiO_2.

Based on the above results, a tentative mechanism of photocatalytic selective C-C cleavage of glycerol is proposed (**Figure 31**). Upon light irradiation, electrons are excited to the conduction band and holes are settled on the valence band of the TiO_2 photocatalysts. The next crucial step is that electrons transfer to Ni single atoms, as evidenced by *operando* XANES. The electron-rich Ni single atom then transfers the electron to the adsorbed O_2, forming the reactive $O_2^{\bullet-}$ radicals, as proved by O_2-TPD and ESR experiments. The decreased oxygen adsorption energy of single Ni atoms makes $O_2^{\bullet-}$ radicals desorb more easily from generation sites. Compared with other ROS, the relatively long survival time of $O_2^{\bullet-}$ radicals enables them to migrate long distances in the reaction media, thus allowing the oxidation reaction to take place beyond the surface of the catalyst.(*19*) In parallel, the hole transfers to water to generate •OH radicals. The formed •OH radicals next activate glycerol (**1**) to the corresponding carbon-centred radicals (**A**), accordingly •OH radicals return to H_2O. The radicals formed by the above reduction and oxidation reactions couple to form (**B**), following cleavage of C-C, forming glycolaldehyde (**2**) and other by-products (**3**). Based on the adsorption energy reported (**Table 5**), the formed glycolaldehyde would diffuse into the solution due to the small adsorption energy with TiO_2, thus avoiding the overoxidation by •OH on the surface of the photocatalyst, which has a strong oxidising ability but a short lifetime.(*19*) As dihydroxyacetone could not serve as an intermediate to generate glycolaldehyde, while glyceraldehyde can work (without yielding formic acid, shown in **Figure 15**), the detected glyceraldehyde during the reaction indicates the possible co-existence of a route to generate glycolaldehyde *via* glyceraldehyde, but the simultaneous formation of formic

acid suggests this is not the major path (**Figure 14d**). Thus, it could be concluded that the glycolaldehyde is mainly generated by the direct cleavage of glycerol, with the involvement of glyceraldehyde oxidation as a minor route as shown in **Figure 31**. In summary, the selectivity of the desired glycolaldehyde product is tuned through the Ni single atoms loaded, where the formation of $O_2^{\bullet-}$ radicals is the key, which is promoted through efficient charge transfer and O_2 adsorption.

Table 5. Adsorption energies of glycerol and glycolaldehyde on TiO_2 anatase surface.

Chemical	Adsorption energy
glycerol	-30.9 kcal/mol(*137*)
glycolaldehyde	-14.4 kcal/mol(*138*)

4.4 Conclusion

In summary, an effective strategy has been presented for the highly selective C-C cleavage of biowaste glycerol to produce valuable product glycolaldehyde under ambient conditions driven by light irradiation. Atomically dispersed Ni species, anchored by the novel molten-salt method, present distinctively catalytic performance compared with nickel oxide nanoparticles loaded by the impregnation method. Unlike little catalysis observed on NiO_x/TiO_2, the optimised single atom photocatalyst $0.5Ni/TiO_2$-MS results in a 2-fold increase in glycolaldehyde evolution rate (1058 $\mu mol \cdot g^{-1} \cdot h^{-1}$) and more importantly a *c.a*. 2-fold enhancement in selectivity (60.1%) compared with NiO_x/TiO_2, leading to a turnover number of 50 moles of glycolaldehyde per mole

of Ni single atoms. Recycling tests indicate the excellent stability of the nickel species-decorated photocatalysts. Through *operando* XANES, the facile electron flow from TiO_2 to Ni single atoms under light illumination has been clearly observed, overshadowing NiO_x nanoparticles which cannot either receive or donate electrons. Based on structural analysis and spectroscopic measurements, the superior activity of the catalyst towards selective C-C cleavage of glycerol under ambient conditions can be ascribed to the weakly chemical adsorption of oxygen and effective electron transfer over Ni single atoms, thus efficient generation of superoxide radicals that would shift selectivity to glycolaldehyde. Such properties provide insights into heterogeneous single-atom photocatalysis and could be generally applied as design principles for photocatalytic organic synthesis with improved activity and controlled selectivity.

5. Multifunction of Ag-Single-Atom Decorated Au/ZnO for Glycerol to Glyceraldehyde and Hydrogen Peroxide

Based on the success of the previous chapter, this chapter concentrates on the production of both glyceraldehyde and hydrogen peroxide (H_2O_2) simultaneously by a highly reactive and selective catalyst using glycerol and oxygen as the feedstock. This catalyst is composed of Ag single atoms homogeneously anchored on Au-nanoparticle-decorated zinc oxide (ZnO). The optimised photocatalyst shows a very high glyceraldehyde yield of 3.86 $mmol \cdot g^{-1} \cdot h^{-1}$, nearly 6 times higher than ZnO, with a remarkable 75% selectivity to glyceraldehyde. Furthermore, H_2O_2 yield reaches 4.64 $mmol \cdot g^{-1} \cdot h^{-1}$, 13 times higher than pristine ZnO, leading to a record AQY of 25 %. The reaction mechanism has also been fully investigated.

5.1 Introduction

Glycerol, with three hydroxyl groups, has many oxidation derivatives, among which glyceraldehyde is one of the most valuable chemicals.(*104*) It can be used in the cosmetic, pharmaceutical industries, and the preparation of polyesters and adhesives. The selective conversion of glycerol to glyceraldehyde could be realised through thermocatalytic or electrochemical oxidations. Although a high yield could be achieved, conventional thermocatalytic approaches are facing various obstacles including the use of exogenous oxidants (e.g., O_2) and high-pH conditions.(*139-144*) The photocatalytic method provides a sustainable strategy for organic compound

oxidations, which can convert glycerol into value-added chemicals under light irradiation and more importantly mild conditions.(*145-147*) The exploration of the photocatalytic glycerol oxidation into glyceraldehyde can be tracked back to 2008 when fluorination was used to block strong adsorbing active sites of TiO_2 and thus avoid unselective C-C cleavage.(*148*) Later, different kinds of bare TiO_2 and C-doped TiO_2 were investigated, in which the highest selectivity of the glyceraldehyde was achieved over C-doped TiO_2 (15%).(*113, 149*) In a recent study, WO_3-based photocatalysts were prepared and used for glycerol oxidation.(*150*) The enhanced acidity on WO_3 resulted in the selective activation of glycerol C-O bonds and facilitated the desorption of glyceraldehyde to the liquid phase, thus improving the selectivity toward glyceraldehyde to 29%. These studies, together with other insightful work, have found that photocatalytic selective oxidation of C-O bonds in alcohols relies on the participation of photogenerated holes and $O_2^{\bullet-}$ radicals.(*109*) Some work indicated that photogenerated holes first deprotonated alcohols to form corresponding radicals, which recombined with $O_2^{\bullet-}$ and finally yielded the ketone molecules,(*20, 28, 29*) while others found that only the photoactivated holes took part in the oxidation of alcohol, the role of $O_2^{\bullet-}$ radicals was mainly for inhibiting the recombination of charge carriers.(*27*) For the latter case, if the formed $O_2^{\bullet-}$ radicals could be used for the construction of another value-added chemical, the high atom economy of selective glycerol oxidation could be achieved, and in the meantime, the photogenerated charge carriers could be effectively separated and fully utilised.

On the other hand, $O_2^{\bullet-}$ radicals are normally generated via the one-electron reduction of dioxygen, further reducing an $O_2^{\bullet-}$ radical by another electron and

coupling with two protons could yield hydrogen peroxide (H_2O_2), a valuable chemical widely used in various industries including organic synthesis, wastewater treatment and pulp bleaching.(*151*) Conventionally, H_2O_2 is produced by the anthraquinone method, an energy-consuming and environmentally unfriendly process. Artificial photosynthesis of H_2O_2 from the above-mentioned stepwise single-electron oxygen reduction route ($O_2 + e^- \rightarrow O_2^{\bullet-}$; $O_2^{\bullet-} + 2H^+ + e^- \rightarrow H_2O_2$) provides a safe, energy-saving, and green method for H_2O_2 production. Taking the efficient Au/TiO_2 as an example, UV irradiation on the photocatalyst in an O_2-saturated ethanol/water mixture could yield H_2O_2 at a millimolar level.(*152*) However, the introduction of Au particles also promoted the decomposition of H_2O_2 - H_2O_2 molecules are strongly adsorbed on the Au surface and decomposed by the further reduction of electrons ($H_2O_2 + e^- \rightarrow \bullet OH + OH^-$).(*153, 154*) Therefore, integrating H_2O_2 production with the selective photocatalytic glycerol oxidation to glyceraldehyde could achieve 100% of atom economy, as following:

$$C_3H_8O_3 + O_2 \rightarrow C_3H_6O_3 + H_2O_2 \qquad (1)$$

Realising such a reaction pathway requires the sophisticated design of photocatalyst, in which three targets must be simultaneously met: 1). selective oxidation of the terminal OH group of glycerol, 2). effective generation of $O_2^{\bullet-}$ radicals, and 3). suppressing H_2O_2 decomposition.

Among various photocatalysts, zinc oxide (ZnO) is of exceptional importance for the photocatalytic generation of H_2O_2.(*155*) Compared to the extensively studied TiO_2, the adsorption energy of H_2O_2 over ZnO is lower, resulting into higher production of H_2O_2.(*156*) Several strategies, including facet

engineering,(*157*) morphology control,(*158*) and heterojunction construction(*159, 160*) have been explored to explore the potential of ZnO as the H_2O_2 generation photocatalyst, in which a maximum H_2O_2 evolution rate of 2.44 $mmol \cdot g^{-1} \cdot h^{-1}$ was achieved over COF-based ZnO/TpPa-Cl composite.(*161*) More importantly, unlike other metal oxides with a strong oxidising ability (e.g. TiO_2) that generate more C-C cleavage products when used for glycerol photocatalytic oxidation, zinc oxide (ZnO) tends to preserve the carbon chain, showing higher selectivity toward valuable products, eg.dihydroxyacetone.(*162*) These potentials of ZnO indicate an ideal candidate for the simultaneous generation of glyceraldehyde and H_2O_2. In this chapter, a novel catalyst with excellent performance is presented, in which Ag single atoms are homogeneously anchored on Au-nanoparticle-loaded ZnO. The photocatalyst can simultaneously and stoichiometrically generate glyceraldehyde and H_2O_2 from glycerol and oxygen at room temperature and under atmospheric pressure with high activity and selectivity. Diverse *in-situ* spectroscopies and microscopies find that Ag-decorated Au nanoparticles can act as hole acceptors, improving charge transfer and facilitating glycerol oxidation. In the meantime, stepwise single-electron oxygen reduction is readily realised over Ag-decorated ZnO for H_2O_2 production. In addition, Ag single atoms can effectively prevent the H_2O_2 decomposition and thus improve the H_2O_2 yield. AuAg co-modified ZnO thus presents nearly 6 times higher glyceraldehyde yield and 13 times higher H_2O_2 yield than pristine ZnO, together with the high selectivity and a long-term stability.

5.2 Experimental

5.2.1 Photocatalyst synthesis

The Au species decorated ZnO (Au/ZnO) was prepared by a molten-salt method. 1 g ZnO was first homogeneously mixed with 2 ml $HAuCl_4 \cdot 3H_2O$ aqueous solution (containing 2.0, 6.0, 10.0, 20.0 mg $HAuCl_4 \cdot 3H_2O$ for 0.1Au/ZnO, 0.3Au/ZnO, 0.5Au/ZnO, 1.0Au/ZnO, respectively). After stirring and drying at ambient temperature overnight, the obtained solid was then ground and mixed with 1.1g KCl and 0.9 g LiCl by pestling in a mortar for 0.5 h. The mixture was then transferred into an alumina crucible and calcined at a certain temperature (400 °C, 500 °C, 600 °C) in a tube furnace for 2 hours under a N_2 atmosphere (heating rate: 8 °C/min). After naturally cooling down to ambient temperature, the mixture was washed with about 1 L water by vacuum filtration to remove the salt residuals. The obtained Au/ZnO was dried in a vacuum oven at 60 °C and denoted as xAu/ZnO-y, in which x represents the weight content of Au to ZnO and y represents the calcination temperature. The calcination temperature is 500 °C if denoted otherwise. Ag species were then loaded by a photodeposition method. Typically, 30 mg Au/ZnO photocatalyst with a certain amount of cocatalyst (using $AgNO_3$ precursor, 0.047 mg – 0.189 mg) was dispersed in an aqueous solution with 10% methanol as the hole scavenger. The mixture was sealed in a 50 ml reactor and purged with Ar gas for 30 min, then irradiated using Perfectlight PCX50A Discover multichannel system with 5W 365 nm light sources (light intensity ≈ 20 mW/cm2) for 1 h. The resulting mixture was washed with water by vacuum filtration and dried in a vacuum oven at 60 °C overnight.

5.2.2 Material characterisation

Powder X-ray diffraction (PXRD) characterisation was conducted on a PANalytical X' pert diffractometer with a Cu–Kα radiation source (40 kV and 40 mA). A continuous mode was used to record data in the 2θ range from 30° to 80°. XPS spectra were recorded on a Thermo ESCALAB 250Xi spectrometer equipped with an Al anode (Al Kα = 1846.6 eV), operated at 15 kV and 10.8 mA. *In-situ* XPS measurements were carried out on the same instrument, using a Xe-lamp as the light source. Survey scans were collected in the range of 0–1,350 eV (binding energy) at the pass energy of 150 eV. The Au and Ag loading amounts were determined with ICP-AES on an IRIS Intrepid II XSP instrument (Thermo Electron Corp.). CasaXPS software was used to process XPS data.

For morphology observation, 1 mg sample was ultrasonically dispersed in 3 ml ethanol for 20 min, and then 1-2 droplets of the suspension were dripped on a copper TEM grid coated with a thin carbon film. The aberration-corrected high-angle annual dark-filed scanning transmission electron microscopy (AC-HAADF-STEM) and energy-dispersive X-ray spectroscopy (EDS) mapping experiment were performed on a JEOL JEM-ARM200F equipped with a CEOS probe corrector, with a guaranteed resolution of 0.08 nm. EDS elemental analysis was taken with the accelerating voltage of 200 kV.

UV-Vis absorption spectra were gained on a PerkinElmer Lambda 950 UV-Vis-NIR spectrophotometer fitted with an integrating holder. Reflection measurements were conducted on powdered samples using a standard barium sulphate powder as the reference. The results were converted to the absorption spectra using Kubelka–Mulk transformation.

Electron paramagnetic resonance (EPR) was conducted on a Bruker A200 electron spin resonance spectrometer at ambient temperature (288 K). Samples (~20 mg) were weighed and transferred into quartz tubes. A high-pressure mercury-vapour lamp (500 W) was used as the light source. For the $O_2^{\cdot-}$ electron spin resonance (ESR) trapping experiments, 100 μL of 5,5-dimethyl-1pyrroline-N-oxide (DMPO, 50 mM) methanol solution was added to 100 μL of methanol suspension of tested samples (4 g L^{-1}). After being irradiated for 2 min, the mixture was characterised using the same electron spin resonance spectrometer.

5.2.3 Photocatalytic performance test

The photocatalytic activity tests of glycerol oxidation were carried out in a Perfectlight PCX50A Discover multichannel system with 5W 365 nm light sources (light intensity 20 mW/cm^2). The reaction temperature was controlled to about 25 °C using a cooling fan. In a typical test, 10 mg photocatalyst was first dispersed into 30 ml 25 mM glycerol aqueous solution. The mixture was sealed in a 50 ml reactor and then sonicated for 3 min. Afterwards, oxygen gas was introduced into the sealed reactor and purged for 30 min. After the reaction, the photocatalyst was removed by filtration, and the liquid products (including H_2O_2) were analysed by high-performance liquid chromatography (HPLC, Shimadzu LC-20AB) equipped with a Rezex ROA-Organic Acid H+ (8%) column, a diode array detector (Shimadzu SPD-M20A), and a refractive index detector (Shimadzu RID-20A). All products were measured by the retention times and absorption spectra, using the commercially available standard compounds as references. Error bars were estimated based on the standard deviation according to three independent experiments. All products in the

reaction mixture were quantified with an external calibration method. The apparent quantum yield (AQY) is calculated using AQY = $2N_{H2O2}/N_p$, where N_{H2O2} is the number of produced hydrogen peroxide molecules assuming one hydrogen peroxide requires two charges and N_p is the number of incident photons. When determining the AQY, the light density was 5.1 mW/cm^2. For the photocatalytic reaction, 10 mg photocatalyst was dispersed into 30 ml 25 mM glycerol aqueous solution. After 1 h irradiation, the amount of H_2O_2 was 0.021 mmol. The irradiation area of the reactor was ~3 cm^2. Thus, the IQYs at 365 nm is c.a. 25.0%.

Scavenger tests were performed by the same procedure with a certain amount of scavengers (e.g. carotene, 4 mg; IPA, 300 mM, 500 μL; SOD, 3 kU/mL, 500 μL; TEOA, 300 mM, 500 μL).

5.3 Results and discussions

5.3.1 Photocatalyst performance

Photocatalytic glycerol oxidation of pristine ZnO was first used in a bottom-irradiation batch reactor where 10 mg of photocatalyst was suspended in 30 mL of 25 mM glycerol aqueous solution at 25 °C for 3 h irradiation in 1 bar O_2. Several oxidation products, including glyceraldehyde, dihydroxyacetone, glycolaldehyde, and formic acid could be detected after 3h-reaction. (**Figure 32a**). It is known that glycolaldehyde production (equation 2) is competitive to glyceraldehyde production (equation 1), while glyceraldehyde accounts for the largest portion (0.68 mM or selectivity of 78.9%) on pure ZnO.

$$C_3H_8O_3 + O_2 \rightarrow C_2H_4O_2 + CH_2O_2 + H_2O \qquad (2)$$

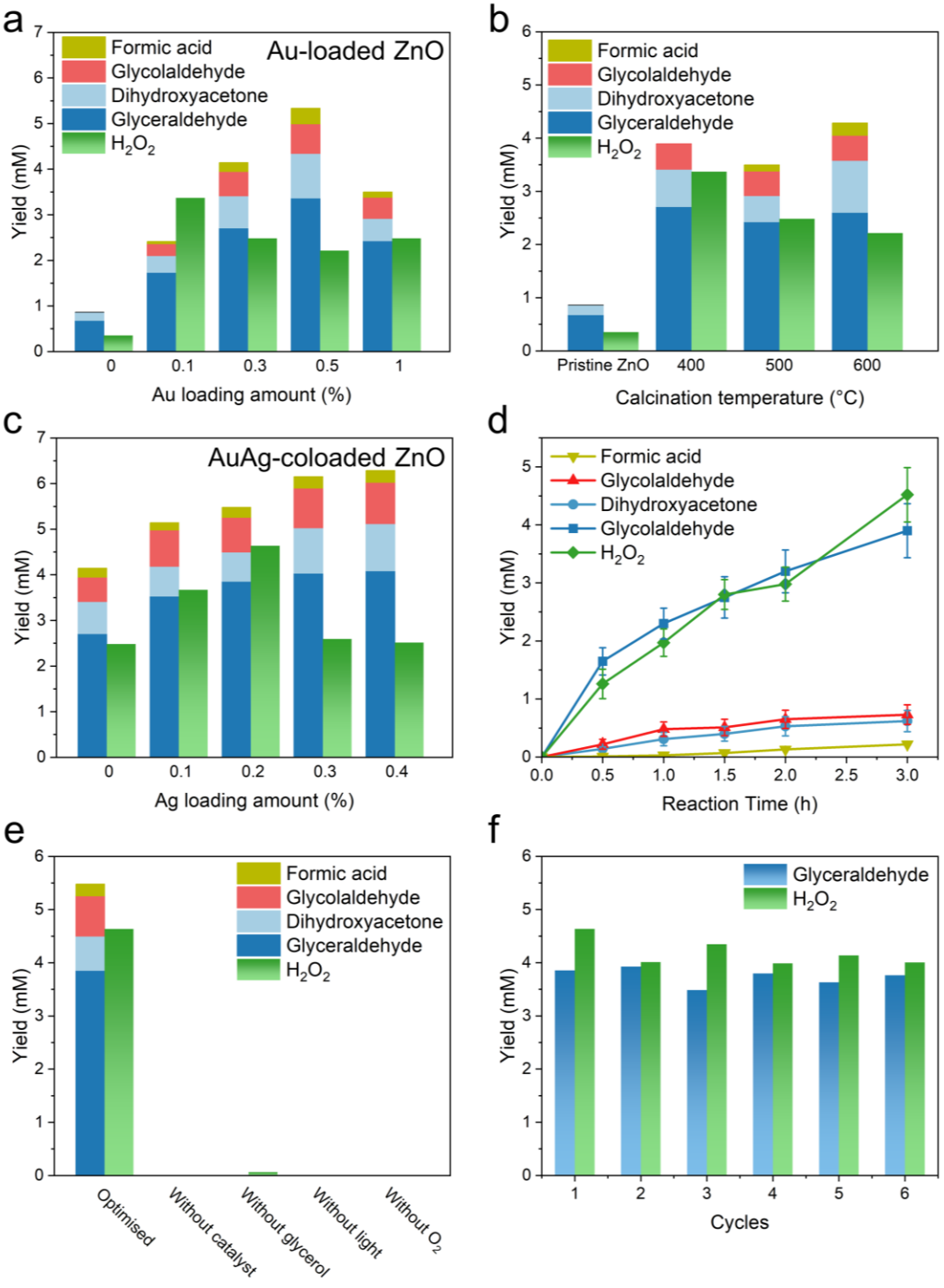

Figure 32. (**a**) The product distribution over Au-loaded ZnO with different Au loading amounts. (**b**) The product distribution over pristine ZnO and 1.0Au/ZnO prepared under different temperatures. (**c**) The product distribution over Ag-loaded 0.3Au/ZnO with different Ag loading amounts. (**d**) The temporal synthesis of different products over 0.3Au0.2Ag/ ZnO. (**e**) Product yields from a series of control experiments. (**f**) Stability test of 0.3Au0.2Ag/ZnO for 6 cycles reaction. Reaction conditions: 10 mg catalyst,

30 mL of 25 mM glycerol aqueous solution, 25 °C, O_2 at atmospheric pressure, 365 nm light irradiation, 3h reaction time.

Notably, 0.35 mM H_2O_2 is also generated during this process, such a result well agrees with the reported values.(*162, 163*) This limited activity is mainly attributed to the prompt charge recombination in the ZnO photocatalyst.(*164*) To restrain the charge recombination and thereby enhance the activity, ZnO photocatalyst was modified by Au species (Au/ZnO) *via* a modified molten-salt method.(*116*) Typically, ZnO nanoparticles were first mixed with $HAuCl_4 \cdot 3H_2O$ aqueous solution. After drying at ambient temperature, the resulting solid was mixed with metal salts and calcined at a certain temperature under N_2 atmosphere. According to previous reports, the calcination temperature significantly affects the photocatalytic performance.(*116*) Therefore, the Au-loaded ZnO was first optimised by changing the calcination temperature while maintaining a 1.0% w.t. loading amount. Introducing Au species to the ZnO surface obviously enhance the activity – the yields of glyceraldehyde and H_2O_2 reach 2.71 mM and 3.37 mM, respectively over the sample calcined at 400 °C (**Figure 32b**). With the calcination temperature increasing, the yield of H_2O_2 decreases while reaching stoichiometry. For example, the yields of glyceraldehyde and H_2O_2 are 2.43 mM and 2.48 mM, respectively over the 500 °C-sample. To obtain a stable reaction condition with stoichiometric generation of glyceraldehyde and H_2O_2 (Equation 1), the following preparation of Au/ZnO was conducted at 500 °C.

To further optimise the Au loading amount, Au/ZnO photocatalysts with different loading amounts were prepared *via* the same method (denoted as xAu/ZnO-y, in which x represents the weight content of Au to ZnO and y

represents the calcination temperature). When the loading amount of Au is less than 0.5%, the yield of glyceraldehyde increases with the loading amount, such as from 1.73 mM over 0.1Au/ZnO to 3.37 mM for 0.5Au/ZnO (**Figure 32a**). In the meantime, the generation of H_2O_2 decreases from 3.37 mM over 0.1Au/ZnO to 2.21 mM when the loading amount is 0.5%. When the Au loading amount reaches 1.0%, the yield of glyceraldehyde decreases to 2.43 mM while the H_2O_2 yield slightly increases to 2.48 mM. Like the consideration during the optimisation of calcination temperature, 0.3% was chosen as the optimum Au loading amount for the following experiments (2.71 mM of glyceraldehyde and 2.48 mM of H_2O_2) as it yields the close-to-stoichiometric products of glyceraldehyde and H_2O_2, It should be noted that though the introduction of Au could intensify the photocatalytic activity, the selectivity toward glyceraldehyde decreases from 78.8% over pristine ZnO to 70.6% over 0.3Au/ZnO, meanwhile the yield of formic acid increases to 0.2mM, indicating the in part destruction of the C-C structure. Thus, to restore the selectivity and further enhance the generation of H_2O_2, Ag as a secondary metal cocatalyst was loaded on 0.3Au/ZnO by a photodeposition method (denoted as 0.3AuzAg/ZnO, in which z represents the weight content of Ag to ZnO). Both the yields of glyceraldehyde and H_2O_2 increase until the Ag loading to 0.2% (3.86 mM of glyceraldehyde and 4.64 mM of H_2O_2), after which the glyceraldehyde keeps increasing and H_2O_2 starts to decrease (**Figure 32c**). The generation rates of glyceraldehyde and H_2O_2 reach 3.86 $mmol \cdot g^{-1} \cdot h^{-1}$ and 4.64 $mmol \cdot g^{-1} \cdot h^{-1}$, respectively over the optimised catalyst 0.3Au0.2Ag/ZnO, nearly 6 times higher glyceraldehyde yield and 13 times higher H_2O_2 yield than pristine ZnO. In the meantime, the selectivity toward glyceraldehyde is enhanced to 75.9% over 0.3Au0.2Ag/ZnO,

which is mainly due to the inhibited generation of formic acid. More importantly, the apparent quantum yield (AQY) of H_2O_2 generation reaches 25.0%, which is higher than most metal-oxide-based photocatalysts.(*164*)

The temporal production of different products over 0.3Au0.2Ag/ZnO indicates that the yield ratio between glyceraldehyde and hydrogen peroxide keeps around 1 (following equation 1) during the whole reaction process while other oxidation products remain low yields (**Figure 32d**). Control experiments were then conducted and are shown in **Figure 32e**. Without O_2, photocatalyst or under dark conditions, either oxidation products or H_2O_2 cannot be detected, highlighting the importance of oxygen for the reaction, and confirming that all the products are generated from glycerol oxidation in the presence of light and oxygen over 0.3Au0.2Ag/ZnO. Without the presence of glycerol, only a trace amount of H_2O_2 is yielded, excluding the major pathway of water-oxidation-induced H_2O_2 generation. In short, it is unambiguous that the photocatalysis process over 0.3Au0.2Ag/ZnO is the only contributor to glycerol oxidation, and H_2O_2 is mainly generated *via* oxygen reduction. **Figure 32f** shows the stability of the best 0.3Au0.2Ag/ZnO catalyst. The catalyst shows similar glyceraldehyde and H_2O_2 yields across six 3h-runs, suggesting the outstanding stability of the catalyst during the photocatalytic reaction.

5.3.2 Materials characterisation

To clarify the mechanism behind the excellent performance of 0.3Au0.2Ag/ZnO, the crystal structure, light-harvesting property, and morphology of these samples were revealed. XRD patterns of 0.3Au/ZnO show

little difference compared with pristine ZnO after the molten-salt loading process (**Figure 33**).

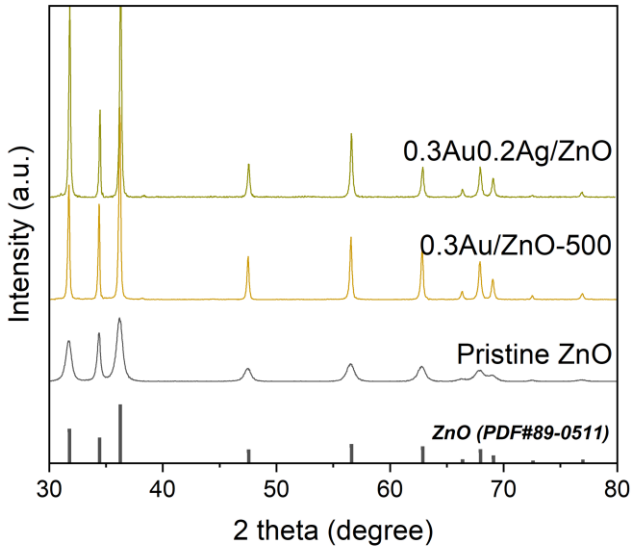

Figure 33. XRD patterns of ZnO, 0.3Au/ZnO and 0.3Au0.2Ag/ZnO.

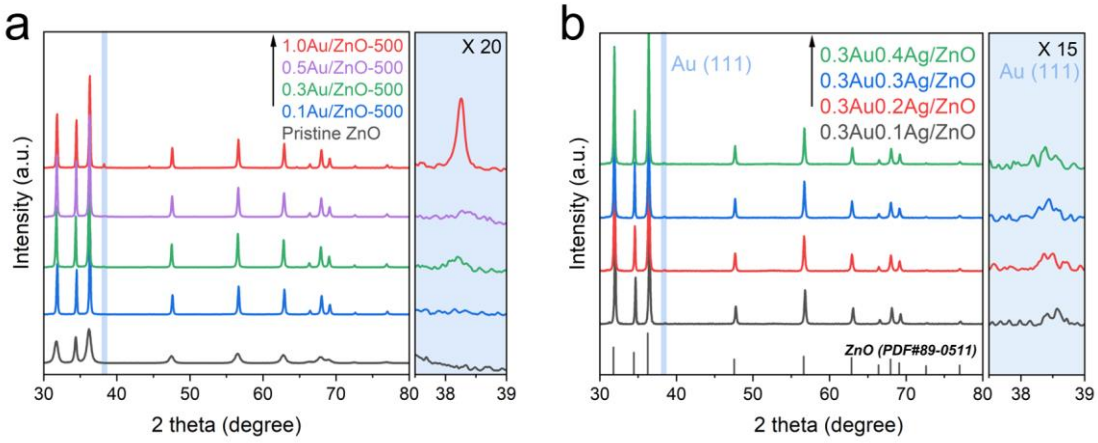

Figure 34. (**a**) XRD patterns of Au/ZnO with different Au loading amounts. (**b**) XRD patterns of 0.3AuAg/ZnO with different Ag loading amounts.

Moreover, there is no obvious Au peak or Ag peak until increasing the loading amount to 0.5% or 0.4%, which is probably due to the high dispersion (**Figure 34**). ICP-AES measurements show a similar actual loading amount

compared with the nominal amount for both Au and Ag species (**Table 6**). All the photocatalysts were washed with a large amount of water after the molten-salt and photodeposition process before use, the salt residues were almost eliminated as indicated by XPS spectra (**Figure 35**).

Table 6. Results of ICP-AES analysis on different ZnO samples.

Samples	Au nominal loading amount (wt %)	Au actual loading amount (wt %)	Ag actual loading amount (wt %)
1.0Au/ZnO-400	1.0	0.75	-
1.0Au/ZnO-500	1.0	0.72	-
1.0Au/ZnO-600	1.0	0.72	-
0.1Au/ZnO-500	0.1	0.08	-
0.3Au/ZnO-500	0.3	0.22	-
0.5Au/ZnO-500	0.5	0.35	-
0.3Au0.2Ag/ZnO	0.3	0.22	0.17

The UV−vis spectra of the prepared samples present the characteristic absorption band with an onset edge at around 388 nm, suggesting a bandgap of around 3.2 eV, consistent with the previously reported value (**Figure 36**).(*164*) After loading metal species, the light absorption of the photocatalysts enhances in the visible region (400-700 nm), while the onset edge remains the same. The absorption peak around 560 nm appears because of the loading of Au nanoparticles, while the peak around 455 nm could be ascribed to the formation of AuAg alloy.(*165*) As the Ag species were photodeposited onto the photocatalyst surface, the formation of AuAg alloy should be attributed to the homogeneous distribution of Ag atoms over Au nanoparticles. As this process

was conducted at room temperature, Ag atoms were unlikely to be doped into Au nanoparticles. Therefore, a core-shell structure could be formed with Au nanoparticle as the core and AuAg mixture as the shell, which will be proved later. On the other hand, it should be noted that the enhanced absorption of visible light could not affect the photocatalytic activity due to a 365 nm light source being used for this study.

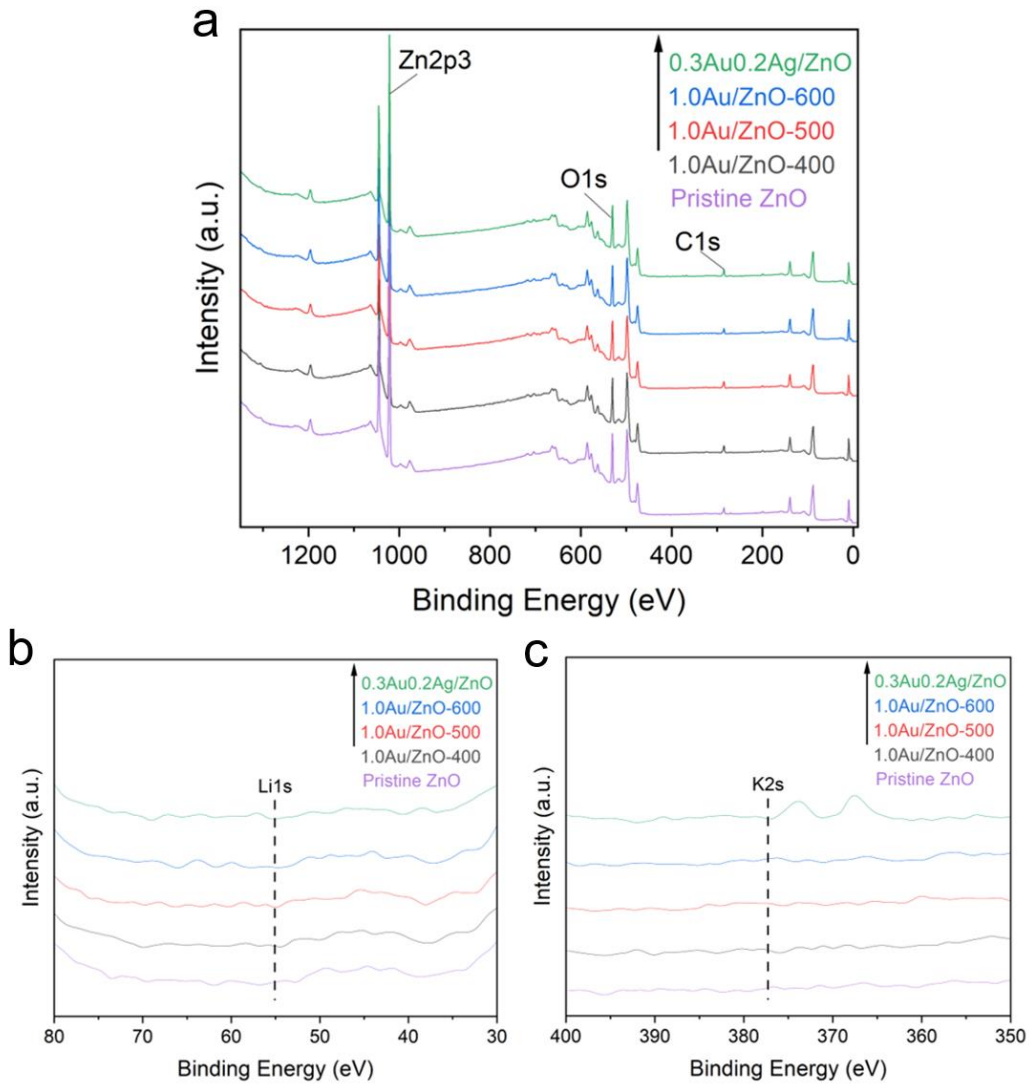

Figure 35. (**a**) XPS survey of different catalysts. (**b**) Li 1s XPS spectra of different catalysts. (**c**) K 2s XPS spectra of different catalysts.

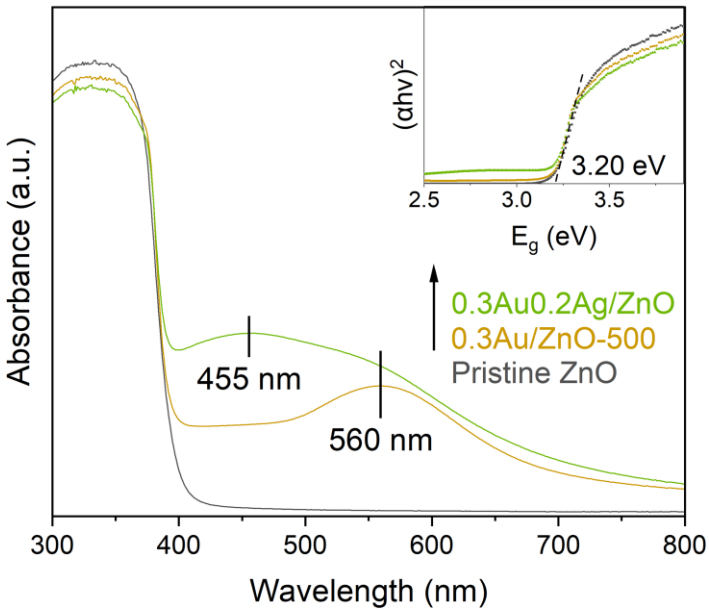

Figure 36. UV-vis spectra of ZnO, 0.3Au/ZnO and 0.3Au0.2Ag/ZnO.

Thereafter, sub-Ångström-resolution aberration-corrected high-angle annual dark-filed scanning transmission electron microscopy (AC-HAADF-STEM) was employed to reveal the structure of the loaded cocatalysts. AC-HAADF-STEM images of 0.3Au/ZnO show the particle size of Au nanoparticles is around 10 nm (**Figure 37a, b**). Apart from the Au nanoparticle with the (200) crystalline fringes could be observed, some bright dots (smaller than 0.2 nm) appear over ZnO surface after the loading of Ag species (**Figure 37c**). The absence of these bright dots over 0.3Au/ZnO indicates that these dots should be Ag single atoms. The line scan also indicates the homogeneous dispersion of Ag species over Au nanoparticles (**Figure 37d**). EDS mapping further confirms Ag species are distributed on the surface of Au nanoparticles (**Figure 37e**). It could be therefore concluded that when using the molten-salt method to load Au species, Au nanoparticles form over the ZnO surface. When using

photodeposition method to load Ag species, Ag atoms not only homogeneously anchor on the surface of Au nanoparticles, thereby constructing a AuAg architecture, but also deposit on the ZnO surface forming single atomic sites.

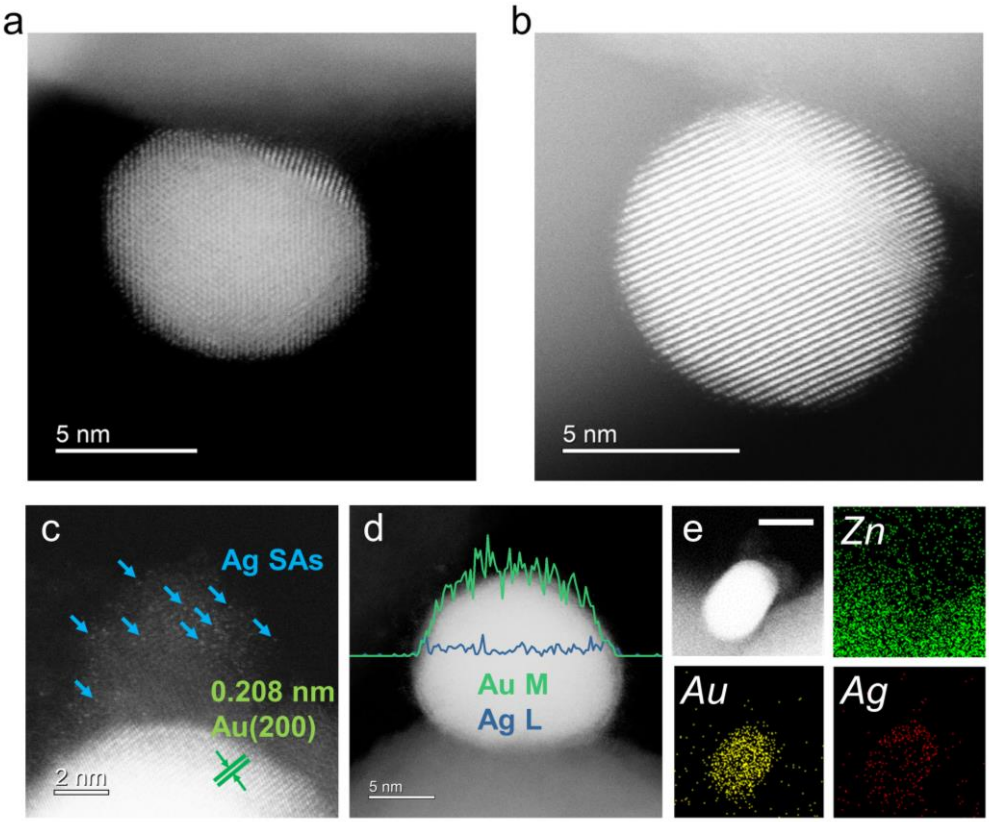

Figure 37. (**a**) and (**b**) Two typical AC-HAADF-STEM images of 0.3Au/ZnO. (**c**) AC-HAADF-STEM image and (**d**) EDX line scan of 0.3Au0.2Ag/ZnO. (**e**) EDX mapping results of 0.3Au0.2Ag/ZnO.

Following the morphology characterisation, the chemical states of gold and silver species of 0.3Au0.2Ag/ZnO were characterised by XPS. For the XPS spectra of Au/ZnO, the dominant peak at 91.3 and 88.5 eV are attributed to the $Zn3p_{1/2}$ and $Zn3p_{3/2}$, respectively (**Figure 38**).(*166*) $Au4f_{7/2}$ is located at around 83.3 eV, which is increasingly visible when the Au loading amount increases. $Au4f_{5/2}$ peak overlaps with $Zn3p_{3/2}$ at around 86.9 eV. In Ag3d XPS spectra, the peaks located at around 368 eV and 374 eV are associated with the $Ag3d_{5/2}$

and $Ag3d_{3/2}$, respectively (**Figure 39a**).(*167*) Ag $3d_{5/2}$ is dominated by the peak at 367.6 eV that corresponds to $Ag^{\delta+}$, indicating most Ag species are slightly oxidised. The partial oxidised Ag species is consistent with the atomically distributed Ag, as Ag is anchored on the surface of ZnO via Ag-O bond. A minor peak at 368.2 eV is ascribed to Ag^0, suggesting that there is a small amount of Ag species that remain in the metallic state.

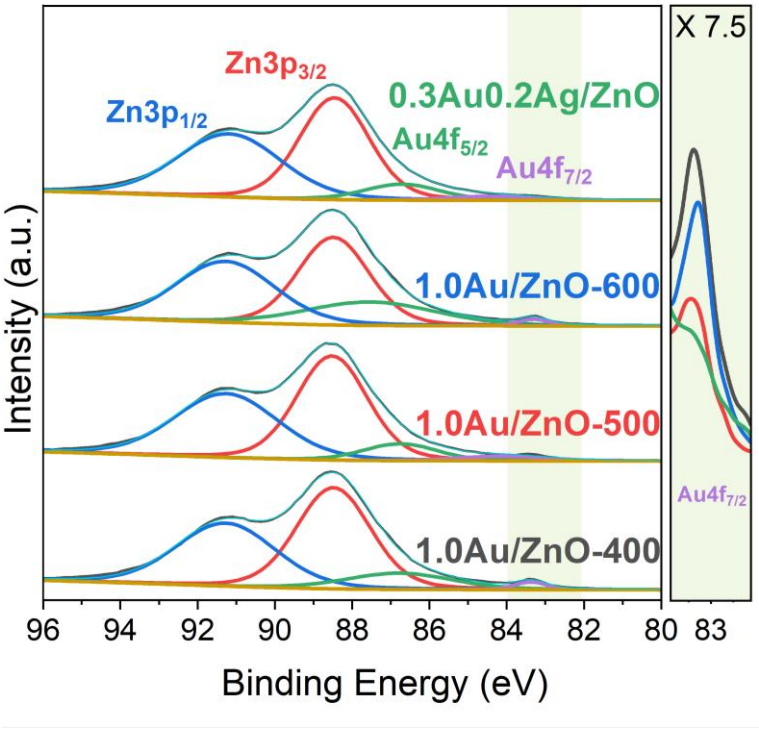

Figure 38. Zn 3p and Au 4f XPS spectra of different catalysts.

In the meantime, high-resolution O 1s XPS spectra were also measured (**Figure 39b**). There are two peaks in the O 1s core-level: one peak at 531.3 eV is ascribed to the oxygen vacancy (O_V), while the other one located at 529.5 eV is attributed to lattice oxygen (O_L) from ZnO lattice.(*116*) The O_V/O_L ratio in 1.0Au/ZnO-500 is 36/64, which is similar with that of pristine ZnO (35/65). After the photodeposition of Ag species, 0.3Au0.2Ag/ZnO sample shows a slightly

decreased content of O_V (30/70), which may result from the Ag-O loading during the photodeposition process.(*164*)

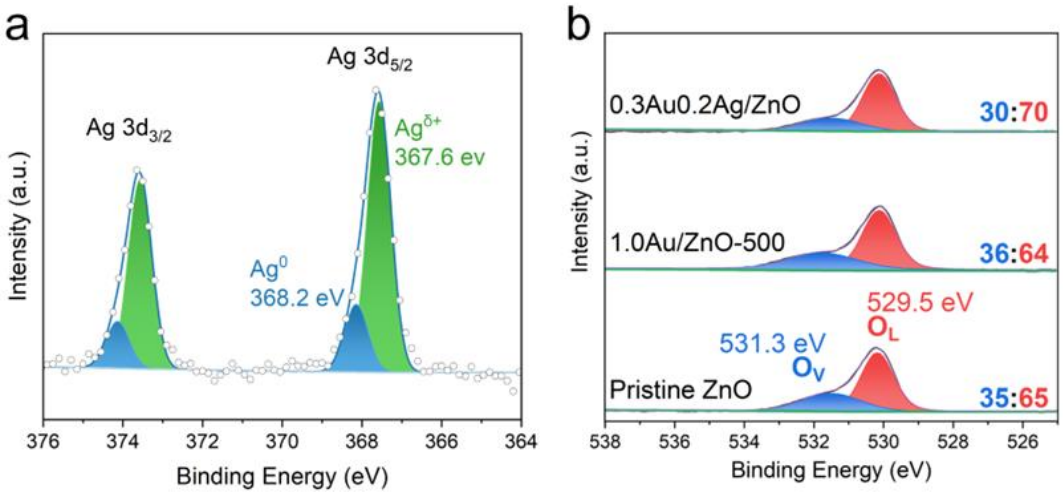

Figure 39. (**a**) Ag 3d XPS spectra of 0.3Au0.2Ag/ZnO. (**b**) O1s XPS spectra of different catalysts.

5.3.3 Mechanism investigation

To further study the nature of oxygen vacancies, *in-situ* electron paramagnetic resonance (EPR) tests were carried out. For pristine ZnO under dark conditions, there is a small peak at g = 1.959, which is attributed to the singly ionised oxygen vacancies (**Figure 40a**).(*168*) UV illumination greatly enhances this peak, indicating that these oxygen vacancies can accept electrons from ZnO when excited by light. 0.3Au/ZnO-500 and 0.3Au0.2Ag/ZnO samples present a different g = 1.957 peak and another g = 2.002 peak, both could be ascribed to neutral oxygen vacancies. Notably, their intensities do not change under UV illumination. According to XPS results, pristine ZnO has a similar amount of oxygen vacancies to 0.3Au/ZnO-500, while it has a lower response under dark conditions in EPR results. The different g values between pristine ZnO and other samples indicate O_V properties are different. In pristine

ZnO, the g = 1.959 peak means the oxygen vacancies are positively charged.

As the EPR is only sensitive to the unpaired electrons, the positively charged oxygen vacancies only have a weak response to the magnetic field. The

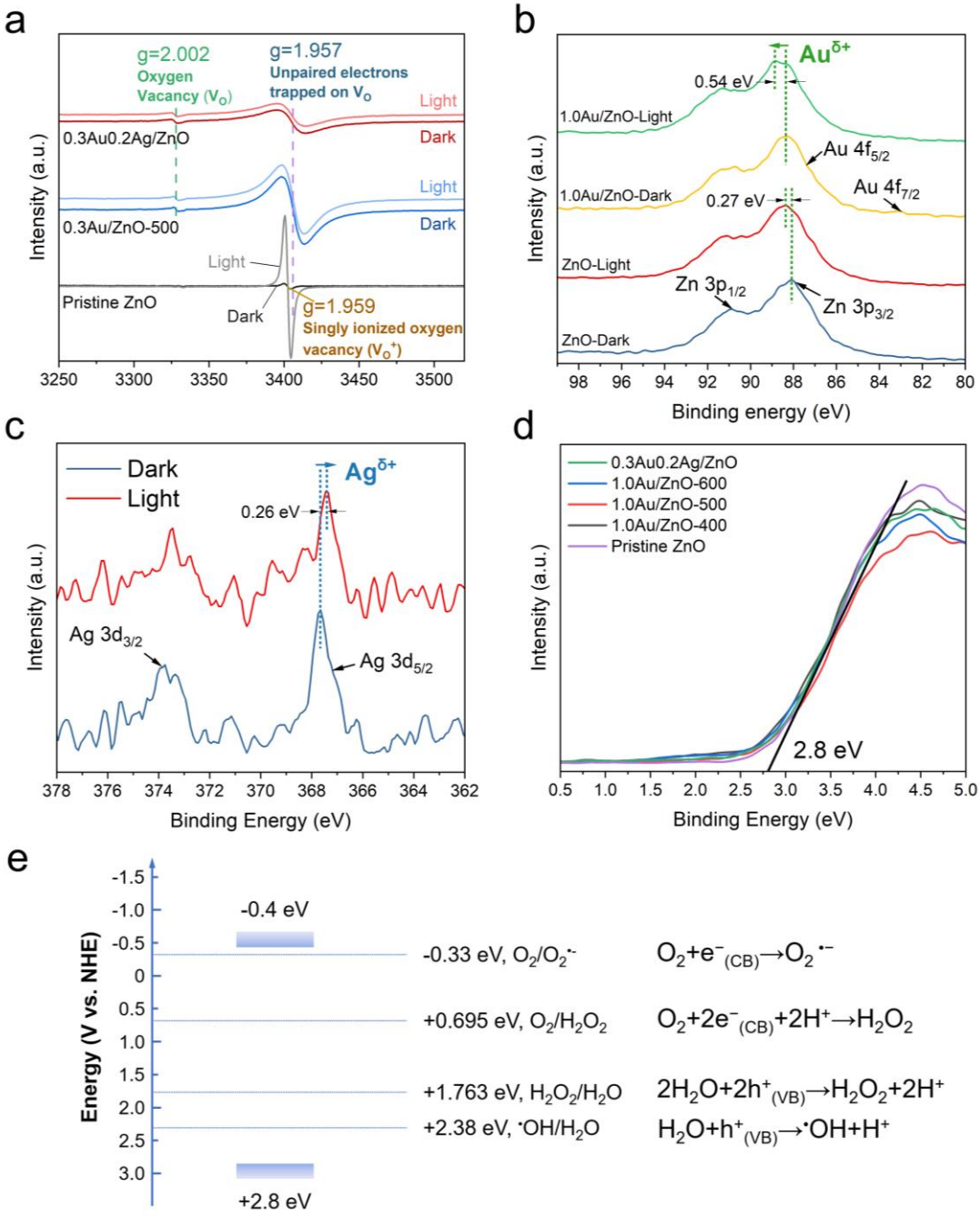

Figure 40. (**a**) *In-situ* ESR spectra of different catalysts under dark and UV illumination conditions. (**b**) *In-situ* Au4f XPS spectra of ZnO and 1.0Au/ZnO in the dark and under UV light irradiation. (**c**) *In-situ* Ag3d XPS spectra of 0.3Au0.2Ag/ZnO in the dark and under UV light irradiation. (**d**) Valence scan of different catalysts. (**e**) The band position of the prepared catalysts and redox potentials of reactive oxygen species.

increased response under light irradiation confirms this point, as photogenerated electrons are trapped to neutralise the O_v. For the other two samples, the g value are 1.957 and 2.002, suggesting the oxygen vacancies are neutralised by electrons from cocatalysts and thus have a strong response to the magnetic field. Therefore, although they have similar oxygen vacancy amounts, the characteristics of the O_v are different, and so are the EPR spectra. Moreover, the decreased intensity of O_v signals in 0.3Au0.2Ag/ZnO EPR sample well agrees with the O1s XPS results, in which a decreased content of O_V is observed after loading Ag species.

Subsequently, *in-situ* XPS study on Au4f and Ag3d spectra of different samples was conducted under light irradiation to clarify the role of cocatalyst species over ZnO surface. As shown in **Figure 40b**, the dominant peaks of pristine ZnO under dark conditions are at 90.9 eV and 88.1 eV, which should be attributed to $Zn3p_{1/2}$ and $Zn3p_{3/2}$, respectively. For the XPS spectra of 1.0Au/ZnO, $Au4f_{7/2}$ peak at around 83.3 eV is very weak due to the low loading amount, while $Au4f_{5/2}$ peak at around 86.9 eV overlaps with $Zn3p_{3/2}$ peak. This makes the characterisation of Au XPS signals change under light irradiation very difficult. However, comparing the shift extent of pristine ZnO and 1.0Au/ZnO reveals the contribution from Au species. Under light irradiation, $Zn3p_{3/2}$ peak of pristine ZnO shows a 0.27 eV shift to the left, which is attributed to the vacancy driven Zn^{2+} to O_v charge transfer.(*164*) 1.0Au/ZnO shows a doubled left shift for $Zn3p_{3/2}$-$Au4f_{7/2}$ peak, indicating the presence of Au species contributes to extra 0.27 eV shift. Such a shift to higher binding energy suggests Au species could serve as the hole acceptors under light irradiation. On the other hand, the slightly-oxidised Ag species over 0.3Au0.2Ag/ZnO shift to lower

binding energy (0.26 eV, **Figure 40c**). Unlike Au element that oxidised states present a higher binding energy than the metal state, Ag element shows the opposite trend – its metal state has a higher binding energy than oxidised states.(*167*) Thus, its shift to lower binding energy suggests atomic dispersed Ag species are further oxidised and thereby also act as the hole acceptors. In short, Au and Ag species both can act as hole acceptors under light irradiation, and this may greatly affect the activity and selectivity of the oxidation reaction, as the holes may directly react with glycerol, which will be analysed later.

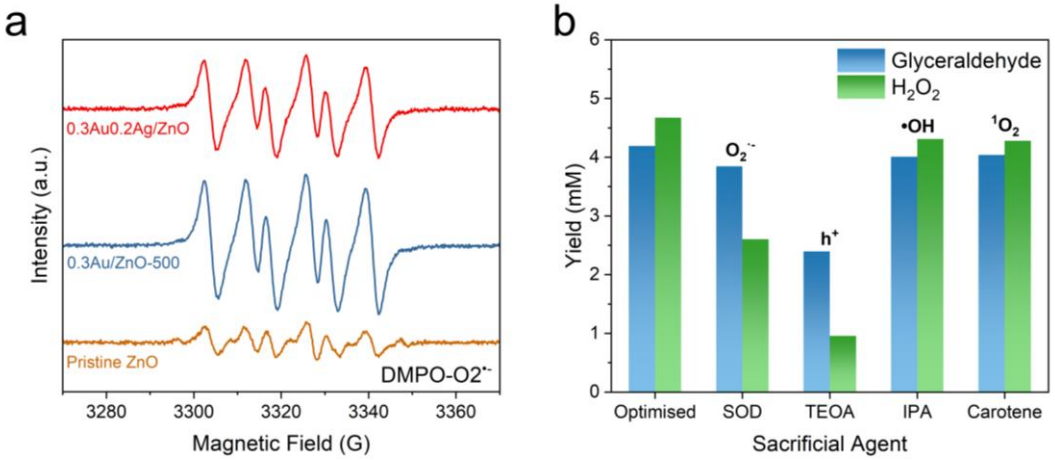

Figure 41. (**a**) ESR spectra for the detection of $O_2^{\bullet-}$ on different catalysts under air atmosphere. (**b**) Glyceraldehyde and hydrogen peroxide yields on 0.3Au0.2Ag/ZnO with the presence of different scavengers.

Combined with the valance electron scan (**Figure 40d**), UV-vis spectra and the reported valence band position of ZnO,(*164*) the band positions of the catalysts could be plotted (**Figure 40e**). The results show the photocatalyst has the ability to generate $O_2^{\bullet-}$ radicals. Electron spin resonance (EPR) tests were then carried out to evaluate this aspect under air atmosphere using 5,5-dimethyl-1-pyrroline-N-oxide (DMPO) as the spin-trap agent. As illustrated in

Figure 41a, pristine ZnO shows a weak signal (a spin derivative of DMPO−$O_2^{\bullet-}$) associated with DMPO−OOH under photoirradiation. Over 0.3Au/ZnO and 0.3Au0.2Ag/ZnO, both have a strong signal of DMPO−OOH, showing a strong ability to generate $O_2^{\cdot-}$ radicals. As $O_2^{\cdot-}$ is an important intermediate for H_2O_2 generation, it could be thus inferred that the loading of Au species could enhance the generation of H_2O_2 and Ag does not reduce this yield.

Considering that several reactive species, including superoxide ($O_2^{\bullet-}$), photogenerated holes (h^+), hydroxyl radicals (•OH), and singlet oxygen ($^1O_2$), could be involved in the glycerol oxidation process, determination of the role of each reactive species is the key to clarify the reaction mechanism. For this purpose, superoxide dismutase (SOD), triethanolamine (TEOA), isopropyl alcohol (IPA), and carotene were selected as the scavengers for $O_2^{\bullet-}$, h^+, •OH, and $^1O_2$, respectively. When adding SOD, the yield of H_2O_2 dramatically decreases, indicating that $O_2^{\cdot-}$ is an important intermediate for H_2O_2 generation. In other words, stepwise single-electron oxygen reduction ($O_2 + e^- \rightarrow O_2^{\bullet-}$; $O_2^{\bullet-} + 2H^+ + e^- \rightarrow H_2O_2$) is the major route of the generation of H_2O_2, consistent with the control experiment (**Figure 32e**). When introducing TEOA, both the yields of glyceraldehyde and H_2O_2 are decreased, indicating the oxidation of glycerol is *via* the direct involvement of h^+ (**Figure 41b**). In the meantime, without the release of the proton (H^+), the formation of H_2O_2 is also affected. On the other hand, the introduction of IPA or carotene does not have a significant effect on the generation of glyceraldehyde and H_2O_2. All these results confirm that H_2O_2 is generated *via* single-electron oxygen reduction, while glyceraldehyde is converted from glycerol *via* the direct oxidation of photogenerated holes.

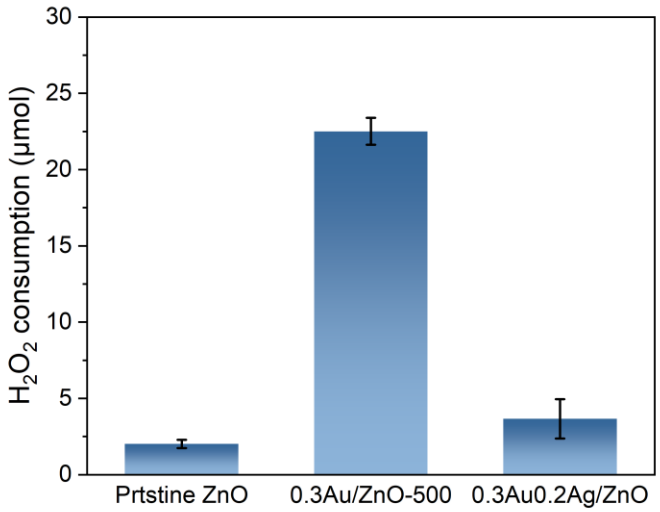

Figure 42. H_2O_2 decomposition over different catalysts. Reaction conditions: 10 mg catalyst, 30 mL of 10 mM H_2O_2 aqueous solution, 25 °C, O_2 at atmospheric pressure, 365 nm light irradiation, 1h reaction time.

As Au nanoparticles or AuAg cocatalysts serve as the hole acceptors, and the generation of H_2O_2 is now confirmed via oxygen reduction by photogenerated electrons, it is reasonable to believe that the oxygen reduction takes place over the ZnO surface. The enhancement of H_2O_2 yield after loading Au species is thus mainly due to the improved charge separation, as photogenerated holes are trapped by cocatalysts, leaving electrons over the ZnO surface to react with oxygen molecules. However, the introduction of Ag does not facilitate the $O_2^{\bullet-}$ generation (as indicated by the analysis of $O_2^{\bullet-}$ in **Figure 41a**) while H_2O_2 yield increases. Considering that H_2O_2 decomposition is another main factor affecting the H_2O_2 yield, the effect of cocatalysts on H_2O_2 decomposition was then studied. In the H_2O_2 decomposition experiment, different photocatalysts were dispersed in the H_2O_2 aqueous solution under light irradiation (**Figure 42**). H_2O_2 decomposition rate over pristine ZnO is low

(2.0 μmol·h^{-1}), loading Au nanoparticles greatly increases the decomposition rate (22.5 μmol·h^{-1}), consistent with the reported and may be attributed to the strong adsorption of H_2O_2.(*154*) After loading Ag species, the H_2O_2 decomposition rate drops back to about 3.7 μmol·h^{-1}, suggesting Ag species can exceptionally prevent the decomposition of H_2O_2. As the formation of H_2O_2 takes place over the ZnO surface, and the decomposition mainly initiated by electrons($H_2O_2 + e^- \rightarrow \bullet OH + OH^-$) (*153, 154*), it should be the Ag single atoms anchored on the ZnO surface that prevent H_2O_2 decomposition. Finally, the used 0.3Au0.2Ag/ZnO were characterised by XRD and XPS, and both show great stability in terms of the structure and chemical state of the optimised photocatalyst (**Figure 43**).

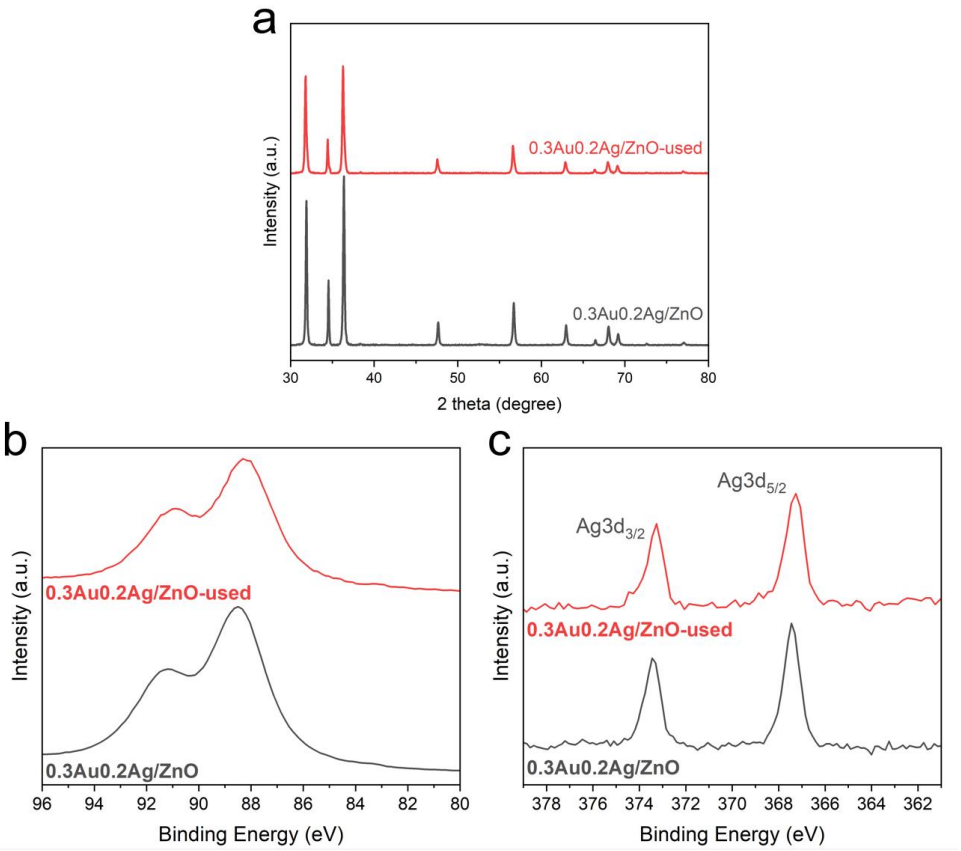

Figure 43. The comparation on (**a**) XRD patterns. (**b**) Au 4f XPS spectra and (**c**) Ag 3d XPS spectra of as-prepared and used 0.3Au0.2Ag/ZnO.

Based on the above analysis, a mechanism is proposed for glycerol oxidation over AuAg co-modified ZnO (**Figure 44**). The AuAg alloy over ZnO could attract photogenerated holes and preferentially react with the terminal –OH group of glycerol, yielding glyceraldehyde with a relatively high selectivity. On the other hand, H_2O_2 is generated *via* stepwise single-electron oxygen reduction over the ZnO surface, the AuAg alloy improve the charge separation and thus facilitate the H_2O_2 formation. The introduction of Ag single atoms to the ZnO surface can prevent the decomposition of H_2O_2 and thus further enhance the H_2O_2 yield. Producing every glyceraldehyde molecule releases 2 H^+ that has been used for generating one H_2O_2 molecule as indicated by the nearly stoichiometric chemistry observed. In the meantime, yielding one glyceraldehyde molecule and one H_2O_2 molecule will consume 2 photogenerated holes and 2 photogenerated electrons, respectively.(*169*) Overall. considering a near stoichiometric generation of glyceraldehyde and H_2O_2 and equal consumption of electrons and holes, this reaction achieves 100%-atom-economy and high charge utilisation.

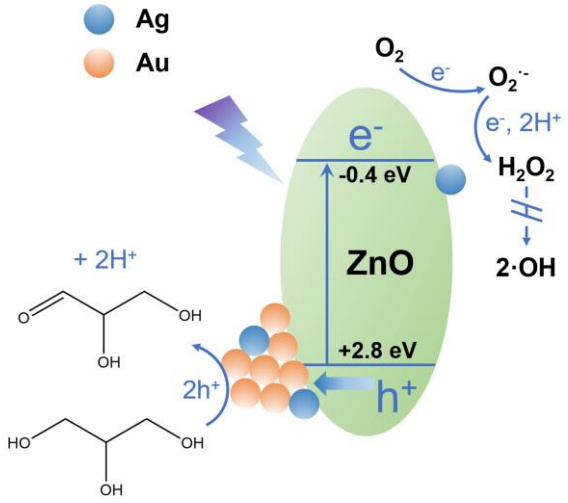

Figure 44. Proposed reaction mechanism of glycerol oxidation on AuAg co-modified ZnO.

5.4 Conclusion

In summary, a strategy for the highly reactive and selective conversion of glycerol and oxygen to both high-value products glyceraldehyde and hydrogen peroxide (H_2O_2) has been achieved under ambient conditions driven by light irradiation. Highly dispersed Ag species over both Au nanoparticles and ZnO surface present intriguing catalytic performance. The optimised catalyst shows 3.86 $mmol \cdot g^{-1} \cdot h^{-1}$ yield to glyceraldehyde with a high selectivity of over 75%, which is nearly 6 times higher than pristine ZnO. Simultaneously H_2O_2 is produced at 4.64 $mmol \cdot g^{-1} \cdot h^{-1}$, 13 times higher than ZnO, together with a AQY of 25.0%. Nearly 100% atom economy and high charge utilisation have also been achieved. Recycling tests indicate the excellent stability of the optimised catalysts. The *in-situ* XPS indicated that Ag-decorated Au nanoparticles can effectively act as hole acceptors under light irradiation, improving the charge transfer and thus facilitating both oxidative half-reaction and reductive half-reaction. Based on structural analysis, spectroscopic measurements, and scavenging experiments, it has been found that the photogenerated holes are directly involved in the glycerol oxidation, Ag atoms dispersed over Au nanoparticles improve the selectivity to glyceraldehyde. In the meantime, $O_2^{\bullet-}$ radicals are facilely formed over Ag-decorated ZnO by photogenerated electrons and further reduced to H_2O_2. During this process, Ag single atoms over the ZnO surface can prevent the H_2O_2 decomposition and thus enhance the H_2O_2 yield. Such multifunctional species over a photocatalyst provide insights into heterogeneous single-atom photocatalysis and could be extensively applied as a design protocol for photocatalytic organic synthesis with improved activity and controlled selectivity.

6. Converting Glycerol into Valuable Trioses by $Cu^{\delta+}$-Decorated WO_3 under Visible Light

The past two chapters both were conducted under UV irradiation (365 nm), to extend the photocatalyst absorption to the visible light region could greatly improve the utilisation efficiency of solar energy, thus making the conversion more energy-efficient. In this chapter, two valuable trioses, i.e. glyceraldehyde and dihydroxyacetone, have been synthesised from glycerol over $Cu^{\delta+}$-decorated WO_3 photocatalyst with a five-fold enhancement in conversion (14.52 $mmol \cdot g^{-1}$) and a total selectivity of 84% compared with pristine WO_3. X-ray photoelectron spectroscopy measurements in the presence and absence of visible light irradiation, electron spin resonance spectroscopies, and isotopic analysis confirm the function of Cu^+ species, which efficiently serve as hole acceptors, enhancing charge transfer which in turn improving the photocatalytic activity.

6.1 Introduction

As pointed out in the previous chapters, glycerol has many oxidation derivatives, which gives it vast potential for transformation into other valuable chemicals, but also makes selectivity control quite difficult.(*170*) Among the various derivatives, two trioses, glyceraldehyde and dihydroxyacetone, are the two most valuable chemicals.(*171, 172*) Realising the conversion from glycerol to glyceraldehyde and dihydroxyacetone would thus create a large and profitable market. Such conversion could be achieved through thermocatalytic or electrocatalytic oxidation over noble metal catalysts (e.g., Au, Ag, Pt or Pd),

which are not only costly but also generate target products at very low rates with limited selectivity.(*173-177*) Light-driven photocatalytic glycerol oxidation provides an alternative approach to upgrading biowaste into building-block chemicals using solar energy.(*109*) Most pioneering studies focused on classic TiO_2-based photocatalysts, in which pH values, reactant concentration, and surface modification of the catalyst were systematically investigated.(*148*) The introduction of noble metals (such as Pt and Au) represents another strategy to improve catalytic activity toward hydrogen production through enhancing charge separation, while the selectivity toward valuable partial-oxidised products was compromised at the same time.(*178, 179*) Recently, a detailed catalytic mechanism of the transformation of glycerol was explored by analysing formed intermediates as a function of glycerol concentration over TiO_2 powders. All these works significantly push forward our understanding of glycerol photocatalytic oxidation over metal-oxide photocatalysts. However, although TiO_2 often presents outstanding performance when absorbing light in the UV region, it lacks the ability to harvest visible light. This constrains its application under sunlight, as UV energy only accounts for about 3-5% of the total solar energy at the Earth's surface.(*7*) Thus, it is of great importance to expanding the light absorption of photocatalytic glycerol oxidation into the visible region.

WO_3 is an excellent metal-oxide photocatalyst with an excellent visible light response. Although it has been extensively studied for pollutant degradation,(*180*) hydrogen production,(*181*) and energy storage,(*182*) its application for glycerol oxidation is rather rare. Moreover, it shows good selectivity towards C3 products but a moderate conversion rate.(*150*) This chapter tends to improve the WO_3 catalytic activity toward glyceraldehyde and

dihydroxyacetone production under visible light without compromising the selectivity. First, earth-abundant Cu species were highly dispersed over the WO_3 surface by a facile impregnation method. Under visible light irradiation (>420 nm), the optimised photocatalyst can efficiently convert glycerol into glyceraldehyde and dihydroxyacetone with high selectivity (with a conversion rate of 14.52 $mmol \cdot g^{-1}$ and a total selectivity of 84%). Diverse *in-situ* spectroscopies, together with scavenging and isotopic experiments, reveal that Cu species serve as hole acceptors, facilitating charge transfer which in turn enhances the photocatalytic activity. Meanwhile, it is found that the glycerol oxidation over $Cu^{\delta+}$-decorated WO_3 proceeds *via* the activation by photogenerated holes, followed by the coupling with •OH, and finally dehydrated into the target products.

6.2 Experimental

6.2.1 Material synthesis

Cu-loaded WO_3 (Cu/WO_3) was prepared by a facile impregnation method. A certain amount of $Cu(NO_3)_2 \cdot 3H_2O$ (for example, 4.75 mg for $0.25Cu/WO_3$) was first dissolved in 0.5 ml of DI water and dropwise added into 0.5 g of WO_3 nanoparticles with continuous stirring (600 rpm). The mixture was then dried at 60 °C under 500 rpm stirring. After evaporating all the water, the solid was transferred into a capped alumina crucible and calcined in a muffle furnace at 400 °C for 2 h under the air atmosphere. After naturally cooling down to room temperature in the furnace, the obtained sample was washed with water three times by centrifugation, dried at 60 °C overnight and stored for subsequent studies.

6.2.2 Catalyst characterisation

X-ray diffraction (XRD) characterisation was carried on using a PANalytical X' pert diffractometer with a Cu–Kα radiation source. The diffractometer was operated at 40 kV and 40 mA with a continuous mode in the 2θ range from 10° to 70°. X-ray photoelectron spectroscopy (XPS) was conducted on a Thermo ESCALAB 250Xi spectrometer. The spectrometer was equipped with an Al anode (Al Kα = 1846.6 eV) and was operated at 15 kV and 10.8 mA. *In-situ* XPS measurements were conducted using the same setup, using a Xe-lamp with a >420 nm filter as the light source. The Cu loading amounts were determined by ICP-AES on an IRIS Intrepid II XSP instrument (Thermo Electron Corp.). CasaXPS software was used to process XPS data. Ultraviolet-visible (UV-Vis) absorption spectra were recorded on a PerkinElmer Lambda 950 UV-Vis-NIR spectrophotometer with a reflection mode. Barium sulphate powder was used as the reference. The obtained results were converted to the absorption spectra using the Kubelka–Mulk transformation.

To prepare the samples for transmission electron microscopy (TEM) examination, ~2 mg sample was homogeneously dispersed in 3 ml ethanol through sonification for 20 min. Afterwards, 1-2 droplets of the mixture were added onto the surface of a copper TEM grid covered with a thin carbon film. TEM observation was conducted on a JEOL JEM-2100F microscope with an operating voltage of 200 kV. EDX mapping was carried out on the same instrument using an Oxford Instruments ISIS/INCA EDS system with an Oxford Pentafet UTW Detector. Electron spin resonance (ESR) spectroscopy was carried out using a Bruker A200 electron spin resonance spectrometer at room temperature (20 °C). To detect •OH radicals, 100 μL of 5,5-dimethyl-1pyrroline-

N-oxide (DMPO, 50 mM) solution was added into 100 μL of the aqueous suspension of tested samples (4 g L^{-1}). After being irradiated by visible light (>420 nm) for 2 min, the mixture was characterised using the spectrometer.

6.2.3 Photocatalytic activity test

The photocatalytic performance of glycerol oxidation was investigated in a PerfectLight PCX50A Discover multichannel system with 5W white light sources (using >420 nm filter, light intensity 10 mW/cm^2). Benefiting from a cooling fan, the reaction temperature was maintained to be about 25 °C. In a typical test, 10 mg catalyst sample was first added into 30 ml 25 mM glycerol aqueous solution with 25 mM H_2O_2, in which the pH was adjusted to the required value by diluted H_2SO_4. The mixture was sealed and sonicated for 3 min to form a homogeneous dispersion. Argon gas was then purged for 30 min. The solution was stirred at 400 rpm during the reaction. After the reaction, the photocatalyst was removed by filtration. The liquid was then analysed by high-performance liquid chromatography (HPLC, Shimadzu LC-20AB). The chromatography was equipped with a Rezex ROA-Organic Acid H+ (8%) column, a diode array detector (Shimadzu SPD-M20A), and a refractive index detector (Shimadzu RID-20A), using 5 mM H_2SO_4 aqueous solution as the mobile phase. All the products were identified by the retention times and absorption spectra, using the commercially available standard chemicals as references. The concentrations of different products were determined by an external calibration method. Glycerol conversion was calculated based on:

$$Conversion = \frac{c_{DHA} + c_{GAD} + 0.33c_{FA} + 0.66c_{GLAD}}{c_{initial}}$$

where $c_{initial}$, c_{DHA}, c_{GAD}, c_{FA}, c_{GLAD} are the initial concentration of glycerol, the product concentration of dihydroxyacetone, glyceraldehyde, formic acid, and glycolaldehyde, respectively. The selectivity of dihydroxyacetone was calculated based on:

$$Selectivity = \frac{c_{DHA}}{c_{DHA} + c_{GAD} + 0.33c_{FA} + 0.66c_{GLAD}}$$

The selectivity of glyceraldehyde was calculated based on:

$$Selectivity = \frac{c_{GAD}}{c_{DHA} + c_{GAD} + 0.33c_{FA} + 0.66c_{GLAD}}$$

Scavenger tests were conducted by the same experimental setup while adding a certain amount of scavengers (e.g. IPA, 300 mM, 500 μL; SOD, 3 kU/mL, 500 μL; TEOA, 300 mM, 500 μL). The isotopic experiment was performed by the same experimental setup while using vol. 3.3% of $H_2{}^{18}O$ aqueous solution as the reaction medium. The reacted solution were analysed by gas chromatography-mass spectrometry (GC-MS, Agilent 8890GC 7250 Q-TOF) equipped with a DB-WAX column.

6.3 Results and discussions

6.3.1 Photocatalyst characterisation

The structures of the pristine WO_3 and Cu-loaded WO_3 were first investigated by X-ray diffraction (XRD), as shown in **Figure 45a**. After loading Cu species, WO_3 retains the monoclinic structure while the diffraction peaks associated with Cu or copper oxides are not observed, suggesting that the Cu species are highly dispersed on the WO_3 surface.

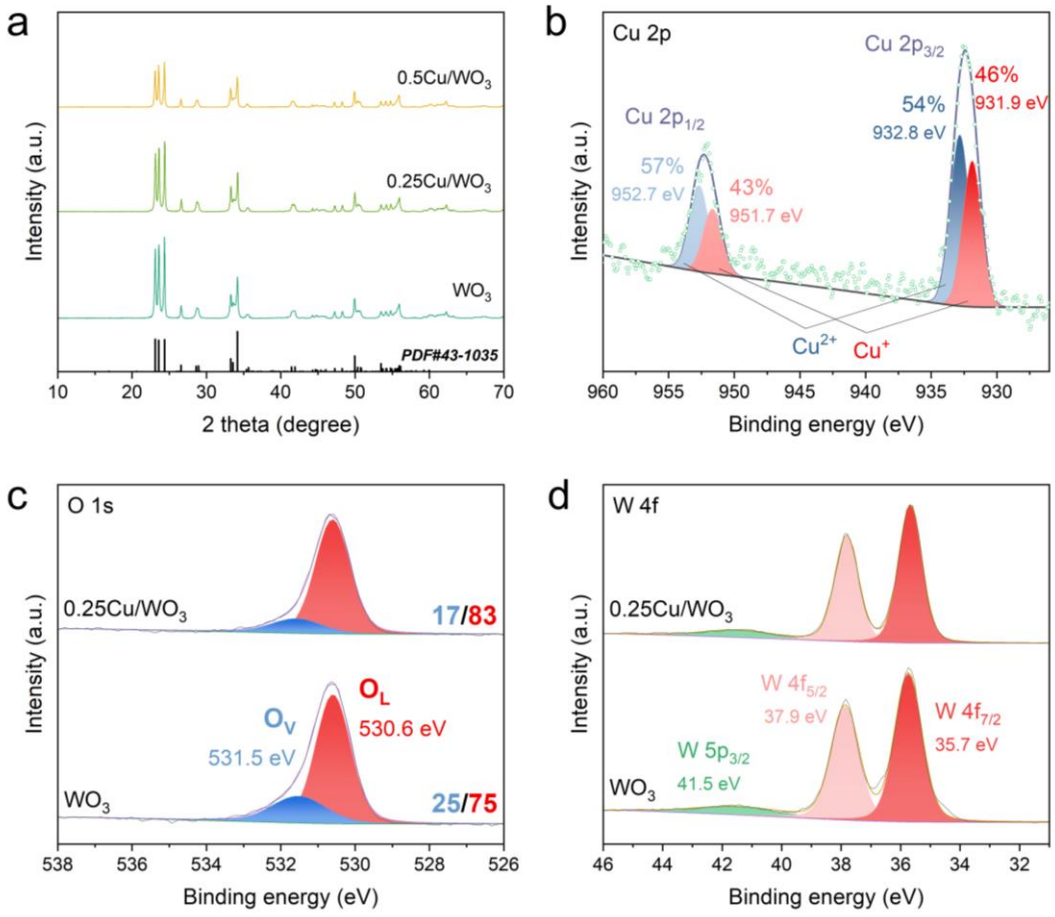

Figure 45. (**a**) XRD patterns of WO_3, 0.25Cu/WO_3 and 0.5Cu/WO_3. (**b**) Cu 2p XPS spectra of 0.25Cu/WO_3. (**c**). O 1s XPS spectra of WO_3 and 0.25Cu/WO_3. (**d**) W 4f XPS spectra of WO_3 and 0.25Cu/WO_3.

The chemical states of loaded Cu species were then investigated by X-ray photoelectron spectroscopy (XPS). The peak at around 932 eV could be ascribed to Cu $2p_{3/2}$, while another peak at around 952 eV is associated with Cu $2p_{1/2}$ (**Figure 45b**).(*183*) Both peaks could be resolved into two components, which correspond to Cu^+ and Cu^{2+} respectively. The amount of Cu^{2+} (54%) is slightly higher than that of Cu^+ (46%). In the meantime, O 1s spectra suggest the amount of oxygen vacancies decreases after loading the Cu species (**Figure 45c**).(*184*) W 4f spectra of both WO_3 and 0.25 Cu/WO_3 are consist of

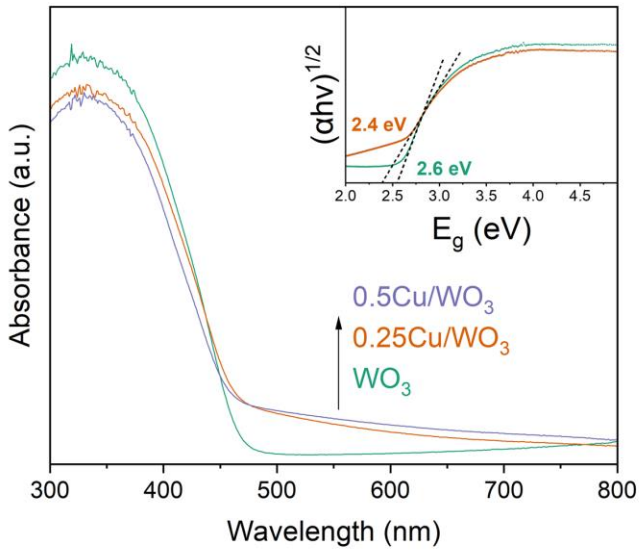

Figure 46. UV-vis spectra of WO_3, 0.25Cu/WO_3 and 0.5Cu/WO_3.

three peaks at 41.5 eV, 37.9 eV and 35.7 eV, which could be ascribed to W^{6+} (**Figure 45d**).(*185*)

The loading amount of Cu was determined by inductively coupled plasma atomic emission spectrometry (ICP-AES) measurements and shows a similar actual loading amount referring to the nominal amount (**Table 7**). The ultraviolet-visible (UV-Vis) spectrum of WO_3 shows a characteristic absorption band with an onset edge of ~460 nm, indicating a bandgap of about 2.6 eV (**Figure 46**), consistent with the widely reported value.(*150*) The spectrum of 0.25Cu/WO_3 catalyst presents an enhanced light absorption in the visible region, which is attributed to the d-d transition of the Cu^{2+} state.(*186*) The morphology of 0.25Cu/WO_3 was then observed by transmission electron microscopy (TEM), as shown in **Figure 47a**. The WO_3 particles have an average diameter of around 150 nm. Under a higher resolution (**Figure 47b**), the (200) crystalline fringes of WO_3 could be observed. Importantly, there are

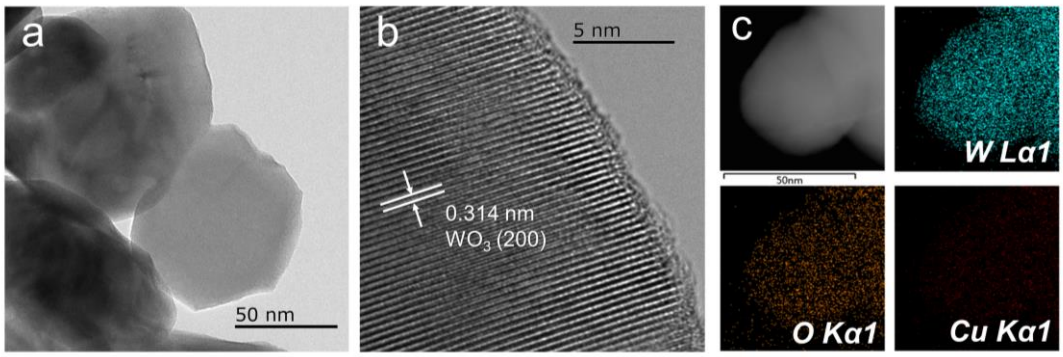

Figure 47. (**a**) TEM image, (**b**) high-resolution TEM image and (**c**) EDX elemental mapping of 0.25Cu/WO_3.

no obvious particles of Cu species on 0.25Cu/WO_3, while EDX mapping shows a homogeneous distribution of Cu species (**Figure 47c**), indicating that Cu species are highly dispersed over the WO_3 surface.

Table 7. Results of ICP-AES analysis on different WO_3 samples.

Sample	Nominal loading amount of Cu (wt %)	Actual loading amount of Cu (wt %)
0.25Cu/WO_3	0.25	0.30
0.5Cu/WO_3	0.5	0.43
0.25Cu/WO_3-used	0.25	0.10

6.3.2 Photocatalytic performance

Pristine WO_3 samples and those loaded with Cu species were then used for glycerol photocatalytic oxidation with hydrogen peroxide (H_2O_2) as an oxidant (glycerol:H_2O_2 = 1:1). Pristine WO_3 shows a selectivity of 55% to glyceraldehyde and 36% to dihydroxyacetone, but with a low conversion of 2.75 mmol·g^{-1} (**Figure 48a**). The other two liquid products, formic acid and

glycolaldehyde, are generated in small amounts. The introduction of Cu species has an obvious impact on the WO_3 catalytic performance. Even only adding 0.01% of Cu species, the conversion increases by 2.6 times to 7.19 $mmol \cdot g^{-1}$, with a selectivity of 59% to glyceraldehyde and 33% to dihydroxyacetone. The optimised catalyst ($0.25Cu/WO_3$) exhibits a five-fold enhancement in conversion (14.52 $mmol \cdot g^{-1}$) and a total selectivity of 84% toward valuable trioses (49% to glyceraldehyde and 35% to dihydroxyacetone) compared with the pristine WO_3. Further increasing the Cu loading amount would slightly decrease the liquid product yields.

The temporal production of different products over $0.25Cu/WO_3$ was then recorded to investigate the oxidation process (**Figure 48b**). All four products are generated at a relatively high rate during the first hour, but the conversion slows down in the next three hours. Notably, the product distribution does not alter when the conversion rate changes, with glyceraldehyde and dihydroxyacetone, two very valuable chemicals, representing the major products. Moreover, the H_2O_2 concentration is important for enhancing the conversion rate, as shown in **Figure 48c**. Without the presence of H_2O_2, no glycerol could be converted. Increasing the H_2O_2 concentration would improve the glycerol conversion, while the selectivity to glyceraldehyde and dihydroxyacetone slightly decreases. Additionally, the glycerol conversion increases obviously when increasing the glycerol concentration (**Figure 48d**).

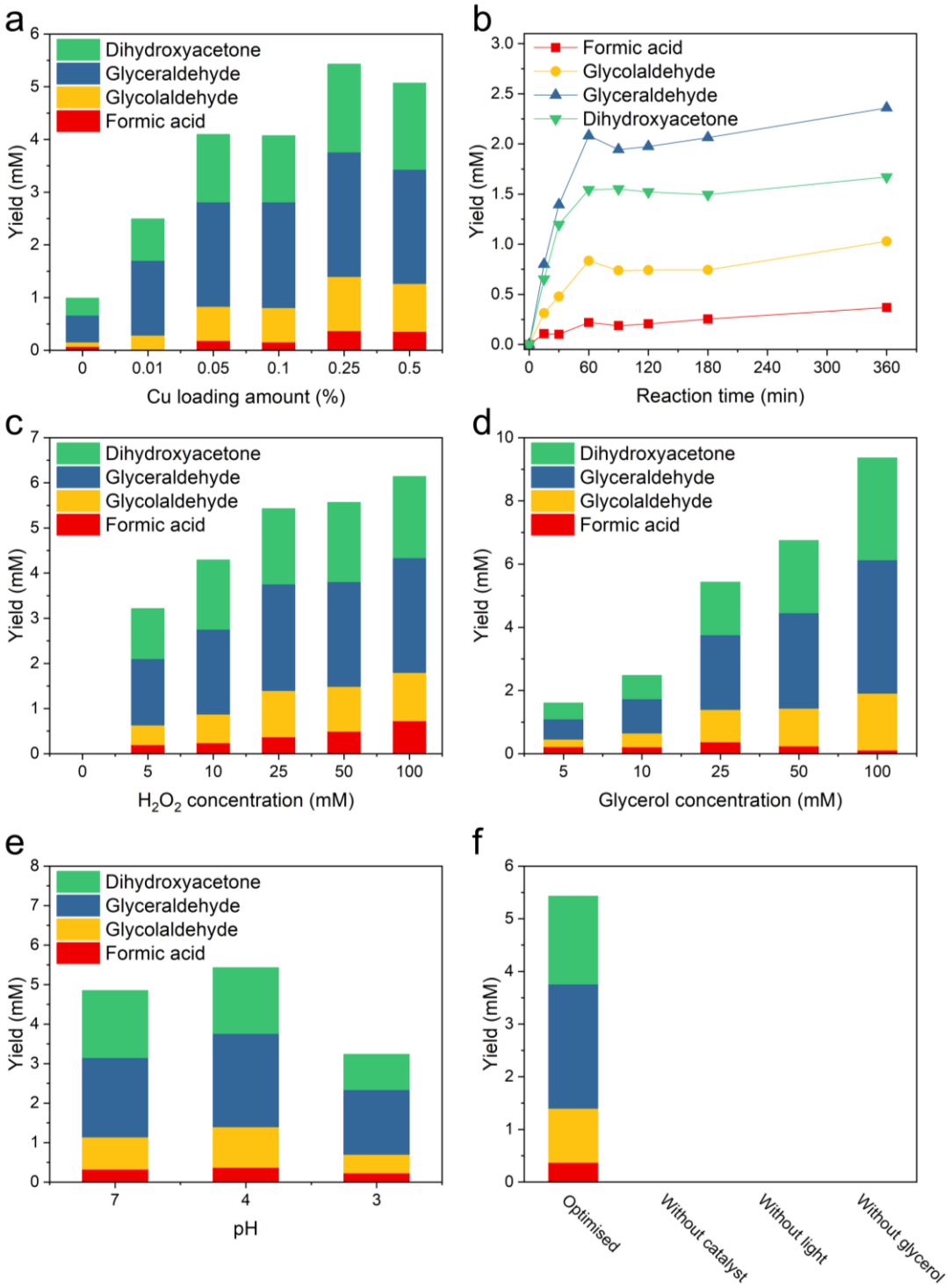

Figure 48. (**a**) The product distribution over Cu/WO_3 with different Cu loading amounts. (**b**) The temporal synthesis of different products over 0.25Cu/WO_3. (**c**) The product distribution over 0.25Cu/WO_3 with different H_2O_2 concentration. (**d**) The product distribution over 0.25Cu/WO_3 with different glycerol concentration. (**e**) The product distribution over 0.25Cu/WO_3 with different pH values of solvent. (**f**) Product yields from a series of control experiments. Reaction conditions: 10 mg catalyst, 30 mL of 25 mM glycerol aqueous solution with 25 mM H_2O_2, 25 °C, argon at atmospheric pressure, visible light irradiation (>420 nm), pH=4 and 4h reaction time unless specifically stated otherwise.

The pH value of the reaction medium was also optimised. When decreasing the pH value from 7 to 4 by adding diluted H_2SO_4 solution, the conversion increases from 13.09 $mmol \cdot g^{-1}$ to 14.52 $mmol \cdot g^{-1}$, indicating protons could promote the reaction (**Figure 48e**). But further decreasing the pH value to 3 would dramatically decrease the conversion to 8.77 $mmol \cdot g^{-1}$. This is rather understandable as WO_3 has an isoelectric point at about pH 2.(*187*) When the pH value approaches this point, the aggregation would become increasingly severe and thus disrupt the dispersion stability. Control experiments are shown in **Figure 48f**. Under dark conditions, no products could be detected, indicating that H_2O_2 and glycerol cannot react over 0.25Cu/WO_3 without light irradiation. When the catalyst or glycerol is absent, no products can be observed either. Thus, it is concluded that it is a photocatalysis process for glycerol conversion. To determine the stability of the photocatalyst, the 0.25Cu/WO_3 was used for 16 h and it is found that the activity drops by about 54% (**Figure 49**).

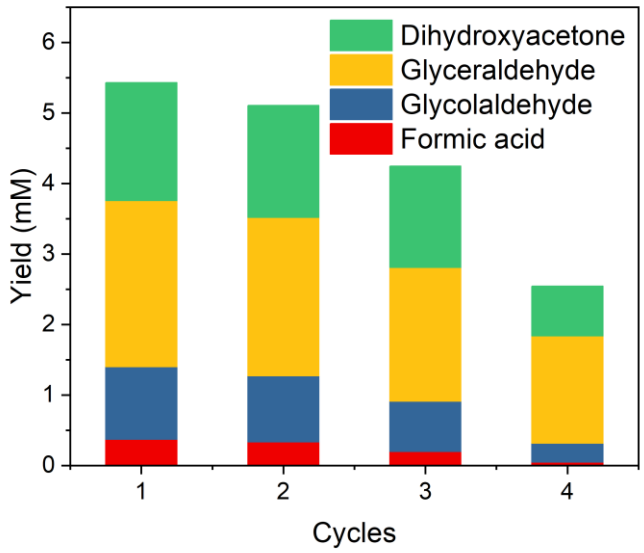

Figure 49. Stability experiment of 0.25Cu/WO_3 for 4 cycles reaction.

6.3.3 Mechanism Analysis

To investigate the mechanism behind the high conversion rate and selectivity to two valuable products glyceraldehyde and dihydroxyacetone over $Cu^{\delta+}$-decorated WO_3, *in-situ* W 4f and Cu 2p XPS spectra were recorded under dark and visible light conditions. Under dark conditions, the *in-situ* W 4f XPS spectrum presents three peaks at 41.5 eV, 37.9 eV and 35.7 eV, corresponding to the W $5p_{3/2}$, W $4f_{5/2}$ and W $4f_{7/2}$, respectively (**Figure 50a**). All these peaks could be assigned to W^{6+}, indicating WO_3 is dominated by the W^{6+} species. Under visible light irradiation (λ >420 nm), new peaks corresponding to W^{5+} and W^{4+} appear, suggesting a part of W^{6+} species are reduced to lower oxidation states. Such results are consistent with the reported observations, in which the amount of W^{5+} in WO_3 increased under light irradiation.(*188*) For Cu species under visible light illumination, both peaks in Cu 2p core level positively shift by about 0.4 eV, suggesting some Cu species are further oxidised (**Figure 50b**). Quantitively analysing the peak areas could provide more detail – the percentage of Cu^{2+} increases from 54% to 69% in Cu $2p_{3/2}$. Combining the *in-situ* W 4f and Cu 2p XPS results, the spatial separation of charge carriers could be unambiguously revealed – photogenerated electrons are trapped by $W^{\delta+}$ in WO_3 and in the meanwhile, holes are transferred into Cu^{+} species.

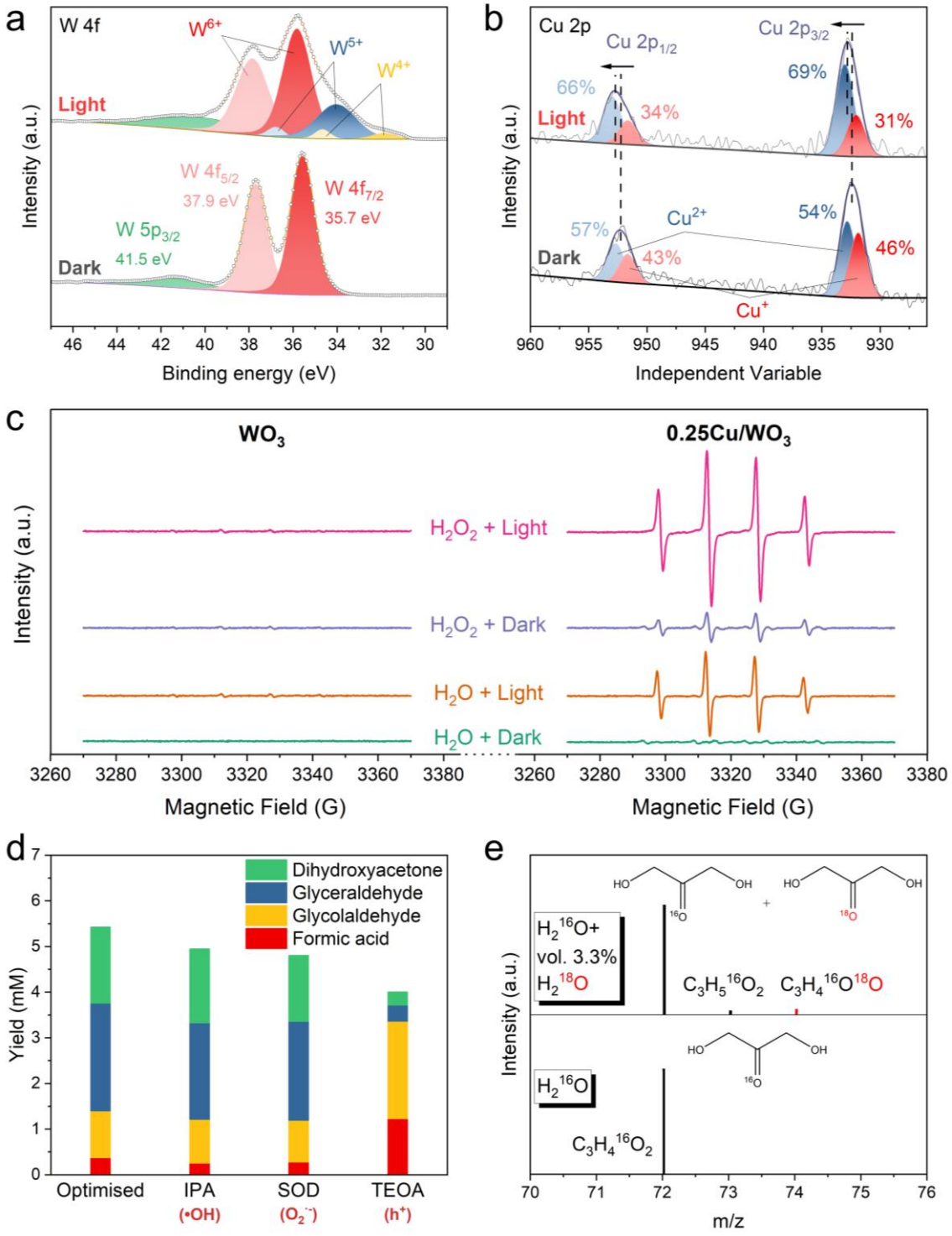

Figure 50. (**a**) *In-situ* W 4f XPS spectra of 0.25Cu/WO_3 in the dark and under visible light irradiation. (**b**) *In-situ* Cu 2p XPS spectra of 0.25Cu/WO_3 in the dark and under UV light irradiation. (**c**) ESR spectra for the detection of •OH on WO_3 and 0.25Cu/WO_3 under different conditions. **(d)** Product yields on 0.25Cu/WO_3 with the presence of different scavengers. (**e**) Isotope-labelled mass spectrum (m/z = 70-76) of liquid products under the same conditions using $H_2{}^{16}O$ or 3.3% vol. $H_2{}^{18}O$ in $H_2{}^{16}O$ as the reaction medium.

As H_2O_2 has been introduced into the system as the oxidant, to investigate its function could clarify the glycerol oxidation mechanism over Cu/WO_3. H_2O_2 can serve as an electron scavenger by being reduced (decomposed) into •OH radicals, which can involve in glycerol oxidation. Therefore, electron spin resonance (ESR) spectroscopy was then conducted to detect the generated •OH over WO_3 and 0.25Cu/WO_3. Over pristine WO_3, ESR results show that there is no obvious signal associated with •OH either in the absence or in the presence of H_2O_2 under dark or visible light conditions (**Figure 50c**). This suggests that pristine WO_3 lacks the ability to oxidise H_2O or reduce (decompose) H_2O_2 into •OH even under light irradiation. For 0.25Cu/WO_3, adding H_2O_2 into the system would result in a 1:2:2:1 quartet ESR signals even under dark conditions, suggesting the facile generation of •OH. The decomposition of H_2O_2 into •OH radicals can more readily take place with the catalysis of Cu species.(*189*) Under dark conditions, no oxidation products could be detected even in the presence of H_2O_2, indicating •OH radicals are not responsible for glycerol oxidation (**Figure 48f**). Under light irradiation, 0.25Cu/WO_3 shows strong •OH-derived ESR signals, indicating the facilitated charge transfer could increase the rate of oxidative reaction. After adding H_2O_2, the •OH-derived ESR signal becomes even stronger, validating the improved charge separation and the role of H_2O_2 as the electron scavenger.

To confirm whether photogenerated holes directly react with glycerol, scavenging experiments were then carried out. In these experiments, the function of various reaction species potentially involved in the reaction can be identified. To selectively remove •OH, $O_2^{\bullet-}$, and h^+, isopropyl alcohol (IPA), superoxide dismutase (SOD), and triethanolamine (TEOA) were added into the

reaction solution, respectively. As shown in **Figure 50d**, IPA and SOD turn out little impact on glycerol oxidation, while TEOA greatly alters the product distribution, formic acid and glycolaldehyde instead of glyceraldehyde and dihydroxyacetone account to the major products. This result can confirm that the glycerol oxidation towards glyceraldehyde and dihydroxyacetone is directly initiated by photogenerated holes. When scavenging these holes, C-C cleavage becomes the major reaction route, possibly due to the strong oxidative ability of •OH radicals. The reaction route of glycerol oxidation over 0.25Cu/WO_3 was further investigated through the isotopic experiments with $H_2{}^{18}O$ and $H_2{}^{16}O$ mixture, as shown in **Figure 50e**. When the reaction medium contains $H_2{}^{18}O$ (vol. 3.3%), gas chromatography–mass spectrometry results show that the detected dihydroxyacetone is composed of 4.0% $C_3H_6{}^{16}O_2{}^{18}O$ and 96.0% $C_3H_6{}^{16}O_3$, indicating that H_2O is the major oxygen source of C=O bond in dihydroxyacetone.

As mentioned in the photocatalytic performance section, the activity of optimised catalyst (0.25Cu/WO_3) drops by about 54% after using for 16 h. To clarify the deactivation, the used catalyst was analysed by ICP-AES, XRD, UV-vis and XPS spectroscopy (**Table 7** and **Figure 51, 52**). ICP-AES results show that there was a 66.7% loss of Cu species from the catalyst to the reaction solution. This may have resulted from the oxidation and dissolution of $Cu^{\delta+}$ species.(*190*) UV-vis and XPS spectra show little change except for the weakened Cu 2p XPS intensity. These results indicate the loss of activity is mainly due to the loss of the loaded cocatalyst, a general problem encountered in photocatalysis.

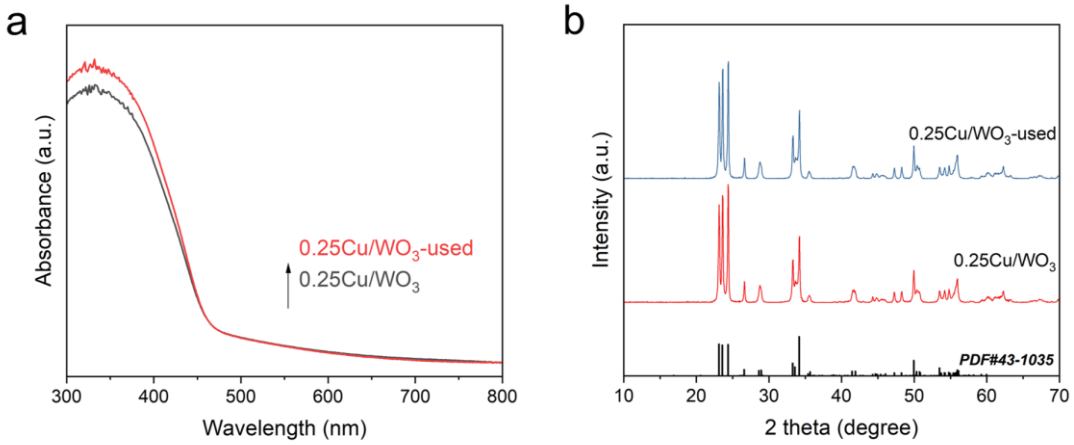

Figure 51. (**a**) UV-vis spectra and (**b**) XRD patterns of as-prepared 0.25Cu/WO_3 and used 0.25Cu/WO_3.

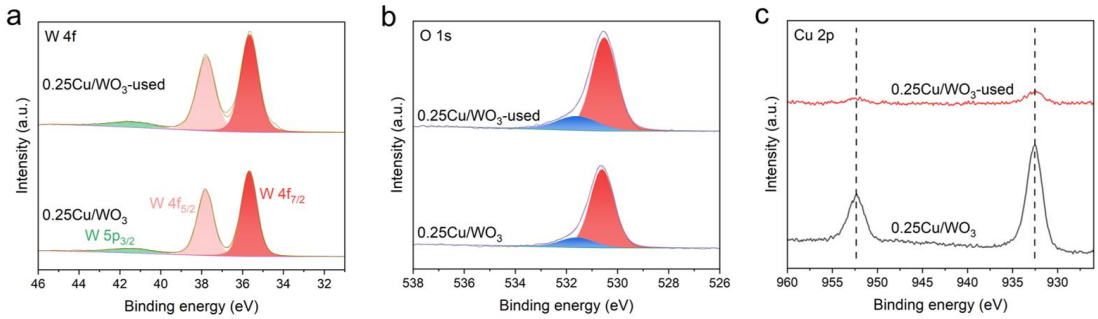

Figure 52. (**a**) W 4f, (**b**) O 1s and (**c**) Cu 2p XPS spectra of as-prepared 0.25Cu/WO_3 and used 0.25Cu/WO_3.

Based on the above results, a reaction mechanism is proposed for the selective glycerol oxidation into glyceraldehyde and dihydroxyacetone over 0.25Cu/WO_3 (**Figure 53**). Incident light first excites electrons from the WO_3 valence band to its conduction band, as indicated by the *in-situ* W 4f XPS spectra under dark and visible light conditions. Photogenerated holes then transfer to Cu^+ atoms, oxidising them into Cu^{2+} species (as shown in the *in-situ* Cu 2p XPS spectra). Electrons on WO_3 are then scavenged by adsorbed H_2O_2, forming OH^- and •OH radicals. In parallel, glycerol molecules react with holes on Cu^+ species to form corresponding radicals (A). Such carbon radicals then react with •OH radicals to form gem-diol intermediates (B), which are unstable

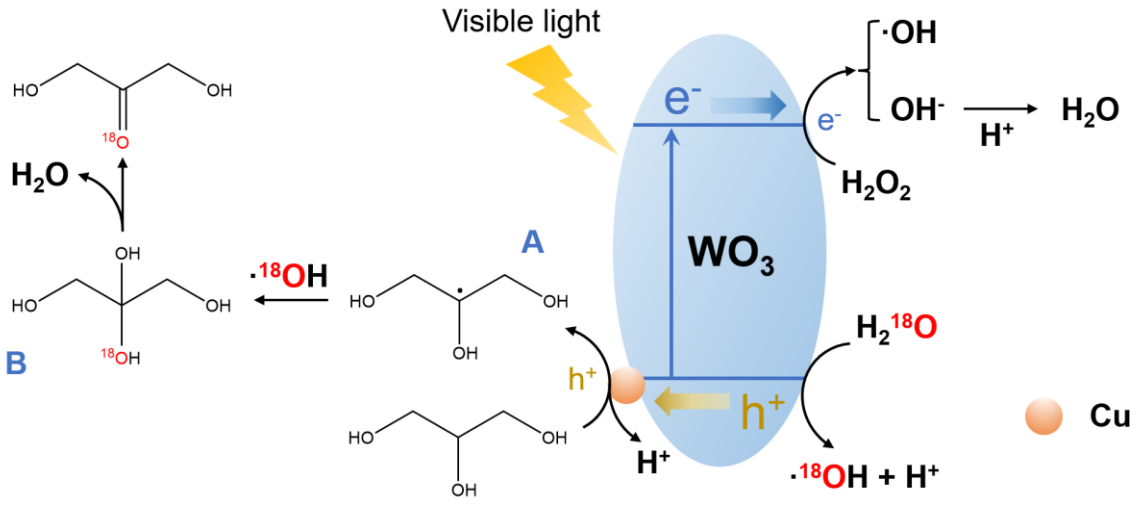

Figure 53. Proposed reaction mechanism of glycerol oxidation on Cu-modified WO_3.

in an acidic environment and would be dehydrated to dihydroxyacetone.(*169*) This process also applies to the formation of glyceraldehyde when holes activate the terminal carbon of glycerol.

6.4 Conclusion

In summary, an effective strategy to enhance the WO_3 photocatalytic activity for glycerol selective oxidation is presented, in which WO_3 loaded with highly dispersed $Cu^{\delta+}$ species is used as a photocatalyst. Under visible light (>420 nm), the catalyst can efficiently convert glycerol into valuable trioses, namely glyceraldehyde and dihydroxyacetone, with a high conversion rate of 14.52 $mmol \cdot g^{-1}$ and a total selectivity of 84%. Based on diverse *in-situ* spectroscopies, scavenging experiments and isotopic analysis, it has been found that Cu^{+} species can efficiently serve as hole acceptors, thus improving the charge transfer and in turn the photocatalytic activity. Following the activation by

photogenerated holes over Cu^{+} species, glycerol molecules are converted into corresponding carbon radicals, which couple with •OH radicals and finally are dehydrated into the target products. The activity of optimised catalyst drops by about 54% after using for 16 h, which is mainly due to the loss of the loaded Cu, a general problem encountered in photocatalysis.

7. Overall conclusions and future work

7.1 Overall conclusions

Glycerol is a versatile molecule because of its three OH groups and can be transformed into various value-added chemicals. Due to the rapid expansion of biodiesel production, its by-product glycerol is often discarded as a waste. Converting glycerol into valuable chemicals under benign conditions has thus been long sought after. However, despite many research efforts have been devoted to this area, it is still a significant challenge to transform glycerol into a specific product with high selectivity and activity. Therefore, glycerol transformation is not only of great scientific significance but also a promising route to utilise biowaste. Metal-oxide-based photocatalysts have been proven as promising catalysts in glycerol conversion under very mild conditions. However, the rapid charge recombination and limited adsorption of reactants constrain their selectivity and activity when used for glycerol oxidation. More importantly, the effects of metal nanoparticles that are often used as cocatalysts are still unclear and sometimes controversial. Therefore, my PhD research is designed to address the above challenges for metal-oxide-based photocatalysts and provide an insightful understanding of cocatalysts in photocatalysis.

In my project, several photocatalysts have been developed, in which metal cocatalysts are highly dispersed over the substrates. Through loading these metal species, the photocatalysts show superior activity and selectively when used for glycerol conversion. Further, the effects of these single atoms on charge transfer, adsorption/desorption abilities, and ROS generation have been

thoroughly studied. The reaction pathways have also been clarified to provide design protocols for photocatalytic organic synthesis.

1) First, an effective strategy has been presented for the highly selective C-C cleavage of biowaste glycerol to produce valuable product glycolaldehyde under ambient conditions driven by light irradiation. Atomically dispersed Ni species, anchored by the novel molten-salt method, present distinctively catalytic performance compared with nickel oxide nanoparticles loaded by the impregnation method. Unlike little catalysis observed on NiO_x/TiO_2, the optimised single atom photocatalyst $0.5Ni/TiO_2$-MS results in a 2-fold increase in glycolaldehyde evolution rate (1058 $\mu mol \cdot g^{-1} \cdot h^{-1}$) and more importantly a *c.a*. 2-fold enhancement in selectivity (60.1%) compared with NiO_x/TiO_2, leading to a turnover number of 50 moles of glycolaldehyde per mole of Ni single atoms. Recycling experiments indicate the excellent stability of the nickel species-decorated catalysts. Through *operando* XANES, the facile electron flow from TiO_2 to Ni single atoms under light illumination has been clearly observed, overshadowing NiO_x nanoparticles which cannot either receive or donate electrons. Based on structural analysis and spectroscopic measurements, the superior activity of the catalyst towards selective C-C cleavage of glycerol under ambient conditions can be ascribed to the weakly chemical adsorption of oxygen on Ni single atoms and effective electron transfer from TiO_2 to Ni single atoms, thus efficient generation of superoxide radicals that would shift selectivity to glycolaldehyde.

2) A two-step modification strategy has next been presented for the highly reactive and selective conversion of glycerol and oxygen to two high-value products glyceraldehyde and hydrogen peroxide under ambient conditions.

Atomically dispersed Ag species over both Au nanoparticles and ZnO surface present intriguing catalytic performance. The optimised catalyst shows a selectivity of over 75% to glyceraldehyde, resulting in nearly 6 times higher glyceraldehyde yield (3.86 $mmol \cdot g^{-1} \cdot h^{-1}$) and 13 times higher H_2O_2 yield (4.64 $mmol \cdot g^{-1} \cdot h^{-1}$) than pristine ZnO, and nearly 100%-atom-economy and high charge utilisation are achieved. Recycling experiments indicate the excellent stability of the optimised catalysts. Through *in-situ* XPS, Ag-decorated Au nanoparticles can effectively act as hole acceptors under light irradiation, improving the charge transfer and thus facilitating both oxidative half-reaction and reductive half-reaction. Based on structural analysis, spectroscopic measurements, and scavenging experiments, it has been found that the photogenerated holes are directly involved in the glycerol oxidation, Ag atoms dispersed over Au nanoparticles improve the selectivity to glyceraldehyde. In the meantime, $O_2^{\bullet-}$ radicals are facilely formed over Ag-decorated ZnO by photogenerated electrons and further reduced to H_2O_2. During this process, Ag single atoms over the ZnO surface can prevent the H_2O_2 decomposition and thus enhance the H_2O_2 yield.

3) Finally to extend the glycerol oxidation into the visible region, an effective strategy to enhance the WO_3 photocatalytic activity for glycerol selective oxidation has been presented, in which WO_3 loaded with highly dispersed $Cu^{\delta+}$ species is used as a photocatalyst. Under visible light (>420 nm), the catalyst can efficiently convert glycerol into valuable trioses, namely glyceraldehyde and dihydroxyacetone, with a high conversion rate of 14.52 $mmol \cdot g^{-1}$ and a total selectivity of 84%. Based on diverse *in-situ* spectroscopies, scavenging experiments and isotopic analysis, the function of Cu^+ species, which efficiently

serve as hole acceptors, so the enhanced conversion rate and high selectivity under visible light and ambient environment can be ascribed to the Cu^+ species which can effectively attract holes, thus improving the charge transfer and in turn the photocatalytic activity. Following the activation by photogenerated holes over Cu^+ species, glycerol molecules are converted into corresponding carbon radicals, which couple with •OH radicals and finally are dehydrated into the target products.

7.2 Future work

The proposed future work includes the following aspects based on the outcomes achieved during my PhD research:

1) Better understanding the roles played by ROS. At present, the modification of photocatalysts to improve selectivity for a specific oxidation reaction relies on the tentative optimisation case by case, since there are many knowledge gaps among the surface characteristics of a catalyst, properties of ROS and specific substrate molecules. A precise and in-depth understanding of the roles played by each ROS in different reactions is extremely important. To this end, by virtue of valid characterization techniques such as ESR, various ROS involved in photocatalytic oxidation reactions have preliminarily been identified and their pivotal roles for photocatalytic activity improvement have in part been proposed. However, the existing techniques can only indicate the existence of ROS, which can hardly clarify the specific role of various ROS. In this sense, the precise characterization of ROS and clarification of their functions in photocatalytic processes remain challenging. Laser-induced fluorescence, chemiluminescence reaction, and direct light absorption or

emission are all reliable techniques to detect ROS generation. Combined with the *in-situ* investigation of charge performance by time-resolved transient absorption spectroscopy, complex roles played by ROS in photocatalytic reactions could be unveiled.

2) Comprehensive understanding of the function of single atom catalysts over photocatalysis. Benefiting from modern characterisation techniques such as X-ray photoelectron spectroscopy and STEM, various single atoms in photocatalytic oxidations have been indicated while their roles for photocatalytic selectivity enhancement were just proposed. Existing techniques can barely reveal the correlation of the concentration and local atomic environment of these single atoms with their activity, which is essential to understand their roles in diverse reactions. To establish more advanced characterisation techniques such as *in-situ* STEM/liquid TEM is therefore critical to clarify the functions of added single atoms and to reduce their negative effects on the selective oxidation.

3) *In-situ* observation of reaction mechanism, including the characterisation of active sites and the transformation of intermediates during photocatalytic reactions. Although theoretical calculation is a powerful method for the study of surface properties and reaction routes of a catalyst, the ideal models used in the simulation are to some extent hard to reflect the real environment and complexity of the reaction and adsorption-desorption behaviour. Emerging techniques should be developed to characterise the active sites and analyse the catalytic mechanism, which is of great value for designing efficient photocatalysts. *Operando* characterisations, a series of cutting-edge techniques for revealing the catalytic reaction mechanism and the dynamic

intermediates evolution under real conditions, should also be widely used in photocatalytic oxidations. It has received a substantial push in recent years, and unsurprisingly, generating a library of exciting results. For instance, coupling time-resolved IR and Raman spectroscopy with mass spectrometry could online identify species adsorbed on the photocatalyst surface, species in the gas phase and subtle surface change of catalysts under “true” reaction conditions, leading to further clarification of the photooxidation mechanisms. Such techniques have already been used in photocatalytic air purification and are expected to bring more insights into photocatalytic organic synthesis (*191*). Based on these solid experimental results generated from advanced characterisation techniques, strong collaboration with modelling work is crucial to validate the model and predict the effective strategy for material modification in a quasi-real condition.

4) Rational design of more efficient photocatalysts. Further improving selectivity in photocatalytic oxidation raises a higher demand for catalyst synthesis. In this context, advanced methods for tailoring the electronic and chemical structures of photocatalysts should be developed. Specifically, single atomic-site catalysts (SACs) or atomic clusters, which could bring exclusively high activity and selectivity in photocatalytic organic synthesis, are still scarcely studied, probably because of difficulties in controlling SACs loading and their distinct characterisation. Despite the extensive studies made to prepare single atomic-site photocatalysts, the synthesis of such SAC with a high content (>10 wt %) is still a major challenge. On the other hand, the selectivity of the most available SACs is unsatisfactory because the single atoms are too active, readily reacting with surrounding reactants and thereafter forming undesired

species. For these reasons, it is significant to seek and develop new strategies to synthesise SACs with high metal content but with a controlled circumstance.

8. Appendix

In this work, the typical HPLC analysis spectra are shown in **Figure S1**. The standard curves of the observed substances are shown in **Figure S2**.

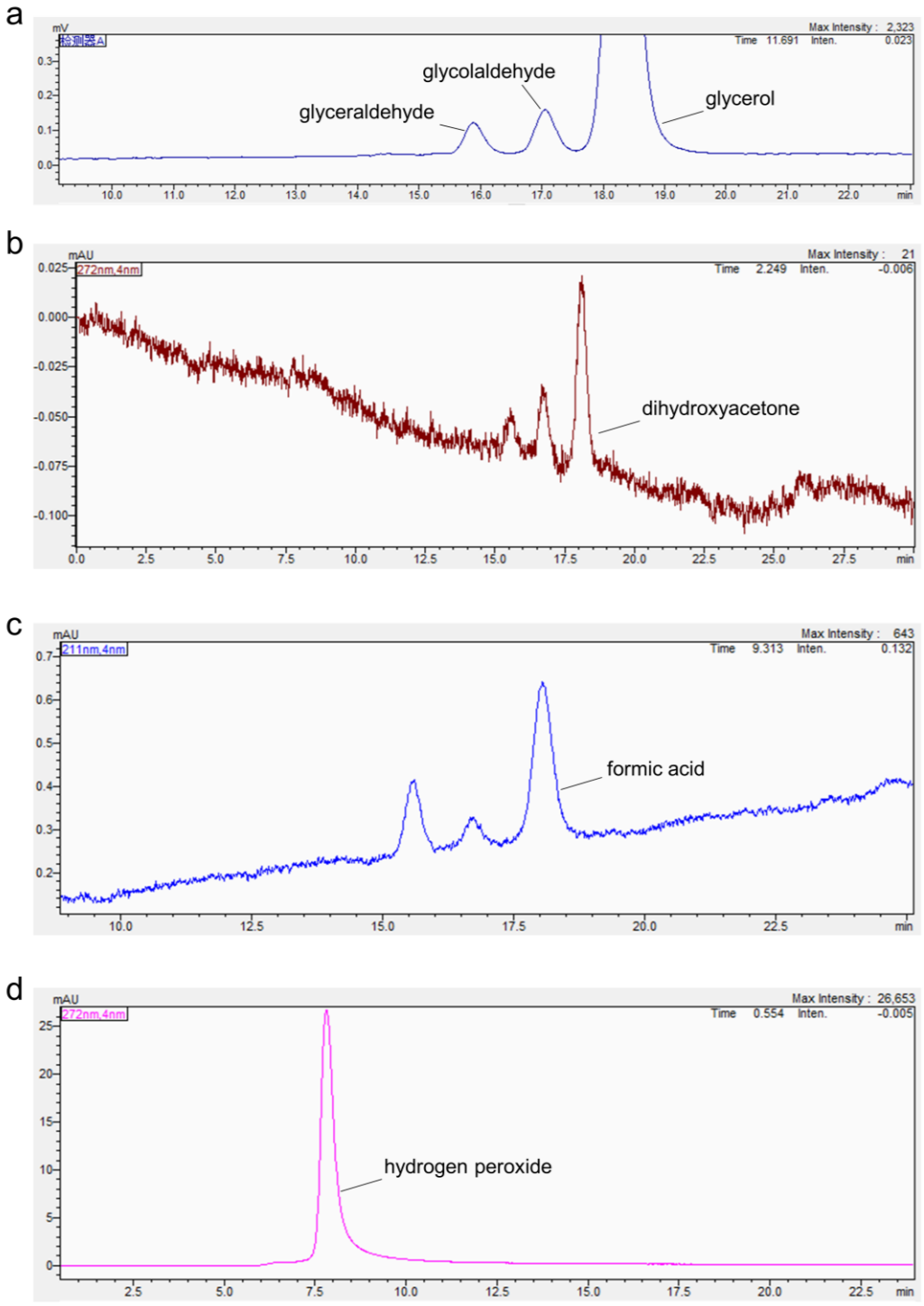

Figure S1. Typical HPLC analysis spectra of glycerol oxidation products.

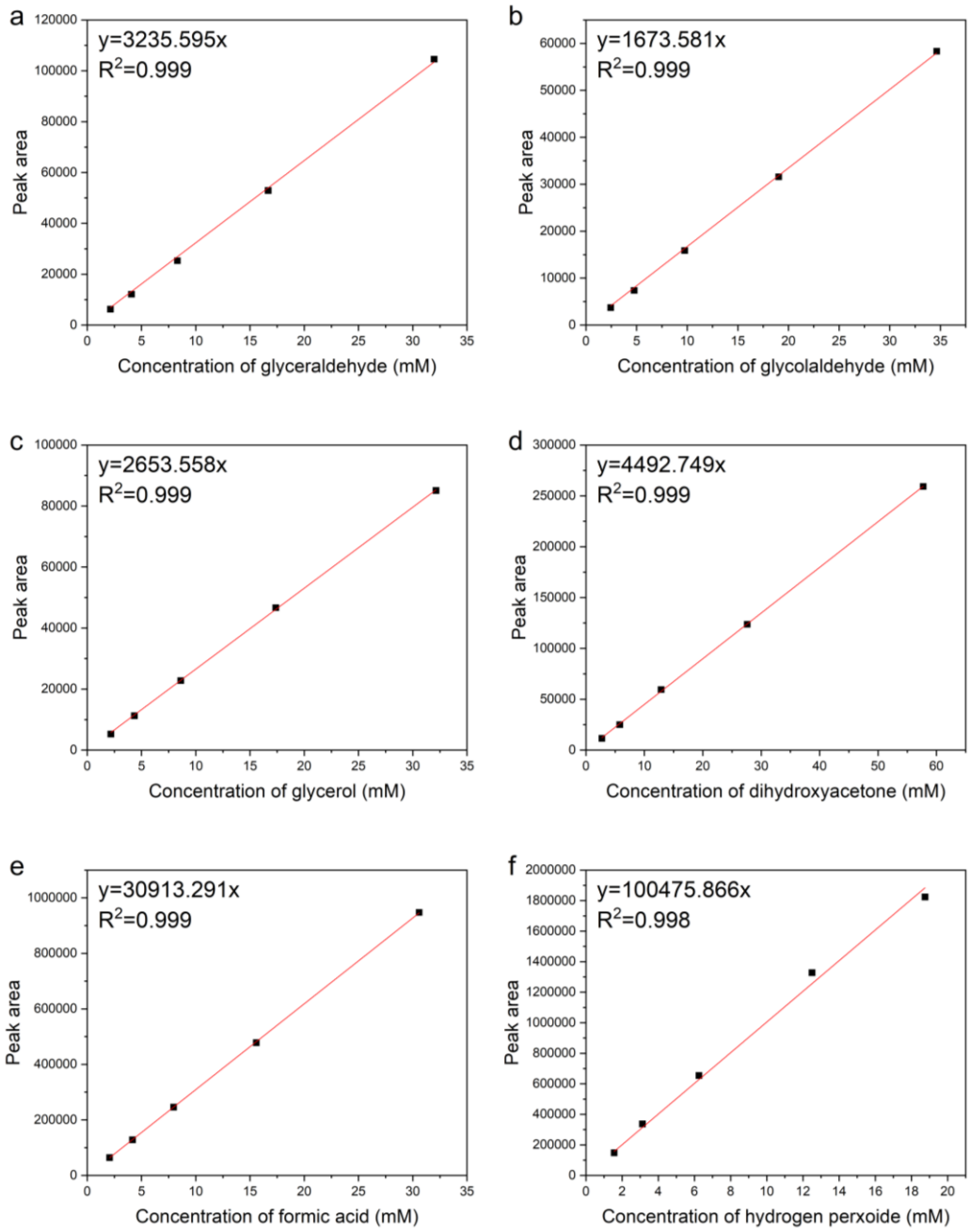

Figure S1. Standard curves of glycerol and oxidation products determined by HPLC. (**a**) glyceraldehyde, (**b**) glycolaldehyde, (**c**) glycerol, (**d**) dihydroxyacetone, (**e**) formic acid and (**f**) hydrogen peroxide.

9. Bibliography

1. J. Li *et al.*, Photoelectrochemical performance enhanced by a nickel oxide–hematite p–n junction photoanode. *Chem Commun* **48**, 8213-8215 (2012).
2. A. Iwaszuk, M. Nolan, Q. Jin, M. Fujishima, H. Tada, Origin of the Visible-Light Response of Nickel(II) Oxide Cluster Surface Modified Titanium(IV) Dioxide. *J. Phys. Chem. C* **117**, 2709-2718 (2013).
3. F. Wöhler, Ueber künstliche Bildung des Harnstoffs. *Annalen der Physik* **87**, 253-256 (1828).
4. G. Ciamician, THE PHOTOCHEMISTRY OF THE FUTURE. *Science* **36**, 385 (1912).
5. A. Fujishima, K. Honda, Electrochemical Photolysis of Water at a Semiconductor Electrode. *Nature* **238**, 37-38 (1972).
6. S. J. A. Moniz, S. A. Shevlin, D. J. Martin, Z.-X. Guo, J. Tang, Visible-light driven heterojunction photocatalysts for water splitting – a critical review. *Energy Environ. Sci.* **8**, 731-759 (2015).
7. Y. Wang *et al.*, Mimicking Natural Photosynthesis: Solar to Renewable H2 Fuel Synthesis by Z-Scheme Water Splitting Systems. *Chem. Rev.* **118**, 5201-5241 (2018).
8. J. Albero, Y. Peng, H. García, Photocatalytic CO2 Reduction to C2+ Products. *ACS Catal.* **10**, 5734-5749 (2020).
9. M. R. Hoffmann, S. T. Martin, W. Choi, D. W. Bahnemann, Environmental Applications of Semiconductor Photocatalysis. *Chem. Rev.* **95**, 69-96 (1995).
10. C. Byrne, G. Subramanian, S. C. Pillai, Recent advances in photocatalysis for environmental applications. *J. Environ. Chem. Eng.* **6**, 3531-3555 (2018).
11. Y. Shiraishi, T. Hirai, Titanium Oxide-based Photocatalysts for Selective Organic Transformations. *J. Japan Pet. Inst.* **55**, 287-298 (2012).
12. C. Joyce-Pruden, J. K. Pross, Y. Li, Photoinduced reduction of aldehydes on titanium dioxide. *J. Org. Chem.* **57**, 5087-5091 (1992).
13. G. Palmisano *et al.*, Selectivity of hydroxyl radical in the partial oxidation of aromatic compounds in heterogeneous photocatalysis. *Catal. Today* **122**, 118-127 (2007).
14. H. Yoshida *et al.*, Photocatalytic hydroxylation of aromatic ring by using water as an oxidant. *ChemComm*, 4634-4636 (2008).
15. X. Lang, H. Ji, C. Chen, W. Ma, J. Zhao, Selective Formation of Imines by Aerobic Photocatalytic Oxidation of Amines on TiO2. *Angew. Chem. Int. Ed.* **50**, 3934-3937 (2011).
16. M. Bellardita *et al.*, Photocatalytic green synthesis of piperonal in aqueous TiO2 suspension. *Appl. Catal. B* **144**, 607-613 (2014).
17. A. M. Thayer, Catalyst Suppliers Face Changing Industry. *Chem. Eng. News* **70**, 27-49 (1992).
18. Y. Nosaka, A. Y. Nosaka, Generation and Detection of Reactive Oxygen Species in Photocatalysis. *Chem. Rev.* **117**, 11302-11336 (2017).

19. D. Wang, L. Zhao, H. Ma, H. Zhang, L.-H. Guo, Quantitative Analysis of Reactive Oxygen Species Photogenerated on Metal Oxide Nanoparticles and Their Bacteria Toxicity: The Role of Superoxide Radicals. *Environ. Sci. Technol.* **51**, 10137-10145 (2017).
20. F. Su *et al.*, mpg-C3N4-Catalyzed Selective Oxidation of Alcohols Using O2 and Visible Light. *J. Am. Chem. Soc.* **132**, 16299-16301 (2010).
21. X. Ye, Y. Cui, X. Qiu, X. Wang, Selective oxidation of benzene to phenol by Fe-CN/TS-1 catalysts under visible light irradiation. *Appl. Catal. B* **152-153**, 383-389 (2014).
22. M. Mrowetz, W. Balcerski, A. J. Colussi, M. R. Hoffmann, Oxidative Power of Nitrogen-Doped TiO2 Photocatalysts under Visible Illumination. *J. Phys. Chem. B* **108**, 17269-17273 (2004).
23. T. Hirakawa, Y. Nosaka, Selective Production of Superoxide Ions and Hydrogen Peroxide over Nitrogen- and Sulfur-Doped TiO2 Photocatalysts with Visible Light in Aqueous Suspension Systems. *J. Phys. Chem. C* **112**, 15818-15823 (2008).
24. M. Okuda, T. Tsuruta, K. Katayama, Lifetime and diffusion coefficient of active oxygen species generated in TiO2 sol solutions. *Phys. Chem. Chem. Phys.* **11**, 2287-2292 (2009).
25. Y.-Z. Chen *et al.*, Singlet Oxygen-Engaged Selective Photo-Oxidation over Pt Nanocrystals/Porphyrinic MOF: The Roles of Photothermal Effect and Pt Electronic State. *J. Am. Chem. Soc.* **139**, 2035-2044 (2017).
26. T. Mallat, A. Baiker, Oxidation of Alcohols with Molecular Oxygen on Solid Catalysts. *Chem. Rev.* **104**, 3037-3058 (2004).
27. X. Xiao, J. Jiang, L. Zhang, Selective oxidation of benzyl alcohol into benzaldehyde over semiconductors under visible light: The case of Bi12O17Cl2 nanobelts. *Appl. Catal. B* **142-143**, 487-493 (2013).
28. H. Li *et al.*, New Reaction Pathway Induced by Plasmon for Selective Benzyl Alcohol Oxidation on BiOCl Possessing Oxygen Vacancies. *J. Am. Chem. Soc.* **139**, 3513-3521 (2017).
29. X. Sun *et al.*, Enhanced Superoxide Generation on Defective Surfaces for Selective Photooxidation. *J. Am. Chem. Soc.* (2019).
30. H. Rezala *et al.*, Photocatalysis with Ti-pillared clays for the oxofunctionalization of alkylaromatics by O2. *Appl. Catal. A-Gen* **352**, 234-242 (2009).
31. Y. Liu *et al.*, A green and efficient photocatalytic route for the highly-selective oxidation of saturated alpha-carbon C–H bonds in aromatic alkanes over flower-like Bi2WO6. *ChemComm* **52**, 1274-1277 (2016).
32. Y. Shiraishi *et al.*, Titanium Dioxide/Reduced Graphene Oxide Hybrid Photocatalysts for Efficient and Selective Partial Oxidation of Cyclohexane. *ACS Catal.* **7**, 293-300 (2017).
33. X. Cao *et al.*, A photochromic composite with enhanced carrier separation for the photocatalytic activation of benzylic C–H bonds in toluene. *Nat. Catal.* **1**, 704-710 (2018).
34. Z. Zhang *et al.*, Revealing the A-Site Effect of Lead-Free A3Sb2Br9 Perovskite in Photocatalytic C(sp3)−H Bond Activation. *Angew. Chem. Int. Ed.* **n/a**, (2020).

35. C. A. Antonyraj, K. Srinivasan, One-Step Hydroxylation of Benzene to Phenol Over Layered Double Hydroxides and their Derived Forms. *Catal. Surv. from Asia* **17**, 47-70 (2013).
36. P. B. Merkel, P. Luo, J. P. Dinnocenzo, S. Farid, Accurate Oxidation Potentials of Benzene and Biphenyl Derivatives via Electron-Transfer Equilibria and Transient Kinetics. *J. Org. Chem.* **74**, 5163-5173 (2009).
37. T. D. Bui, A. Kimura, S. Ikeda, M. Matsumura, Determination of Oxygen Sources for Oxidation of Benzene on TiO2 Photocatalysts in Aqueous Solutions Containing Molecular Oxygen. *J. Am. Chem. Soc.* **132**, 8453-8458 (2010).
38. R. Su *et al.*, Selective photocatalytic oxidation of benzene for the synthesis of phenol using engineered Au–Pd alloy nanoparticles supported on titanium dioxide. *ChemComm* **50**, 12612-12614 (2014).
39. O. Tomita, B. Ohtani, R. Abe, Highly selective phenol production from benzene on a platinum-loaded tungsten oxide photocatalyst with water and molecular oxygen: selective oxidation of water by holes for generating hydroxyl radical as the predominant source of the hydroxyl group. *Catal. Sci. Technol.* **4**, 3850-3860 (2014).
40. D. Wang, M. Wang, Z. Li, Fe-Based Metal–Organic Frameworks for Highly Selective Photocatalytic Benzene Hydroxylation to Phenol. *ACS Catal.* **5**, 6852-6857 (2015).
41. X.-J. Yang *et al.*, Photocatalytic organic transformation by layered double hydroxides: highly efficient and selective oxidation of primary aromatic amines to their imines under ambient aerobic conditions. *ChemComm* **50**, 6664-6667 (2014).
42. Y. Zhang, N. Zhang, Z.-R. Tang, Y.-J. Xu, Graphene Transforms Wide Band Gap ZnS to a Visible Light Photocatalyst. The New Role of Graphene as a Macromolecular Photosensitizer. *ACS Nano.* **6**, 9777-9789 (2012).
43. D. Shen *et al.*, Photocatalytic Asymmetric Epoxidation of Terminal Olefins Using Water as an Oxygen Source in the Presence of a Mononuclear Non-Heme Chiral Manganese Complex. *J. Am. Chem. Soc.* **138**, 15857-15860 (2016).
44. B. Chandra, K. K. Singh, S. S. Gupta, Selective photocatalytic hydroxylation and epoxidation reactions by an iron complex using water as the oxygen source. *Chem. Sci.* **8**, 7545-7551 (2017).
45. Y. Huang *et al.*, Stable Copper Nanoparticle Photocatalysts for Selective Epoxidation of Alkenes with Visible Light. *ACS Catal.* **7**, 4975-4985 (2017).
46. C. B. Almquist, P. Biswas, The photo-oxidation of cyclohexane on titanium dioxide: an investigation of competitive adsorption and its effects on product formation and selectivity. *Appl. Catal. A-Gen* **214**, 259-271 (2001).
47. S. Farhadi, M. Zaidi, Polyoxometalate–zirconia (POM/ZrO2) nanocomposite prepared by sol–gel process: A green and recyclable photocatalyst for efficient and selective aerobic oxidation of alcohols into aldehydes and ketones. *Appl. Catal. A-Gen* **354**, 119-126 (2009).
48. W. Mu, J.-M. Herrmann, P. Pichat, Room temperature photocatalytic oxidation of liquid cyclohexane into cyclohexanone over neat and modified TiO2. *Catal. Lett.* **3**, 73-84 (1989).

49. M. Zhang *et al.*, Oxygen Atom Transfer in the Photocatalytic Oxidation of Alcohols by TiO2: Oxygen Isotope Studies. *Angew. Chem. Int. Ed.* **48**, 6081-6084 (2009).
50. J. Tripathy, K. Lee, P. Schmuki, Tuning the Selectivity of Photocatalytic Synthetic Reactions Using Modified TiO2 Nanotubes. *Angew. Chem. Int. Ed.* **53**, 12605-12608 (2014).
51. Z. Yu *et al.*, Dual modification of TiNb2O7 with nitrogen dopants and oxygen vacancies for selective aerobic oxidation of benzylamine to imine under green light. *J. Phys. Chem. A* **5**, 4607-4615 (2017).
52. J. Gascon *et al.*, Isoreticular MOFs as Efficient Photocatalysts with Tunable Band Gap: An Operando FTIR Study of the Photoinduced Oxidation of Propylene. *ChemSusChem* **1**, 981-983 (2008).
53. M. Dan-Hardi *et al.*, A New Photoactive Crystalline Highly Porous Titanium(IV) Dicarboxylate. *J. Am. Chem. Soc.* **131**, 10857-10859 (2009).
54. Y. Fu *et al.*, An Amine-Functionalized Titanium Metal–Organic Framework Photocatalyst with Visible-Light-Induced Activity for CO2 Reduction. *Angew. Chem. Int. Ed.* **51**, 3364-3367 (2012).
55. D. Sun, L. Ye, Z. Li, Visible-light-assisted aerobic photocatalytic oxidation of amines to imines over NH2-MIL-125(Ti). *Appl. Catal. B* **164**, 428-432 (2015).
56. C. Xu *et al.*, Turning on Visible-Light Photocatalytic C−H Oxidation over Metal–Organic Frameworks by Introducing Metal-to-Cluster Charge Transfer. *J. Am. Chem. Soc.* **141**, 19110-19117 (2019).
57. S. Linic, P. Christopher, D. B. Ingram, Plasmonic-metal nanostructures for efficient conversion of solar to chemical energy. *Nat. Mater.* **10**, 911-921 (2011).
58. X. Lang, X. Chen, J. Zhao, Heterogeneous visible light photocatalysis for selective organic transformations. *Chem. Soc. Rev.* **43**, 473-486 (2014).
59. A. Tanaka, K. Hashimoto, H. Kominami, Preparation of Au/CeO2 Exhibiting Strong Surface Plasmon Resonance Effective for Selective or Chemoselective Oxidation of Alcohols to Aldehydes or Ketones in Aqueous Suspensions under Irradiation by Green Light. *J. Am. Chem. Soc.* **134**, 14526-14533 (2012).
60. K. Kimura, S.-i. Naya, Y. Jin-nouchi, H. Tada, TiO2 Crystal Form-Dependence of the Au/TiO2 Plasmon Photocatalyst's Activity. *J. Phys. Chem. C* **116**, 7111-7117 (2012).
61. S.-i. Naya, K. Kimura, H. Tada, One-Step Selective Aerobic Oxidation of Amines to Imines by Gold Nanoparticle-Loaded Rutile Titanium(IV) Oxide Plasmon Photocatalyst. *ACS Catal.* **3**, 10-13 (2013).
62. P. Devaraji, N. K. Sathu, C. S. Gopinath, Ambient Oxidation of Benzene to Phenol by Photocatalysis on Au/Ti0.98V0.02O2: Role of Holes. *ACS Catal.* **4**, 2844-2853 (2014).
63. Y. Shiraishi *et al.*, Platinum Nanoparticles Supported on Anatase Titanium Dioxide as Highly Active Catalysts for Aerobic Oxidation under Visible Light Irradiation. *ACS Catal.* **2**, 1984-1992 (2012).
64. T. Uchihara, M. Matsumura, A. Yamamoto, H. Tsubomura, Effect of platinum loading on the photocatalytic activity and luminescence of cadmium sulfide powder. *J. Phys. Chem. A* **93**, 5870-5874 (1989).

65. Y. Shiraishi, K. Fujiwara, Y. Sugano, S. Ichikawa, T. Hirai, N-Monoalkylation of Amines with Alcohols by Tandem Photocatalytic and Catalytic Reactions on TiO2 Loaded with Pd Nanoparticles. *ACS Catal.* **3**, 312-320 (2013).
66. Y. Huang *et al.*, Photoimmobilized Ni Clusters Boost Photodehydrogenative Coupling of Amines to Imines via Enhanced Hydrogen Evolution Kinetics. *ACS Catal.* **10**, 3904-3910 (2020).
67. D. Tsukamoto *et al.*, Photocatalytic H2O2 Production from Ethanol/O2 System Using TiO2 Loaded with Au–Ag Bimetallic Alloy Nanoparticles. *ACS Catal.* **2**, 599-603 (2012).
68. S.-i. Naya, M. Teranishi, K. Kimura, H. Tada, A strong support-effect on the catalytic activity of gold nanoparticles for hydrogen peroxide decomposition. *ChemComm* **47**, 3230-3232 (2011).
69. C. Feng *et al.*, Dual interfacial synergism in Au-Pd/ZnIn2S4 for promoting photocatalytic selective oxidation of aromatic alcohol. *Appl. Surf. Sci.* **501**, 144018 (2020).
70. Y. Sugano *et al.*, Supported Au–Cu Bimetallic Alloy Nanoparticles: An Aerobic Oxidation Catalyst with Regenerable Activity by Visible-Light Irradiation. *Angew. Chem. Int. Ed.* **52**, 5295-5299 (2013).
71. B. Qiao *et al.*, Single-atom catalysis of CO oxidation using Pt1/FeOx. *Nat. Chem.* **3**, 634 (2011).
72. W. Wu *et al.*, Involving Single-Atom Silver(0) in Selective Dehalogenation by AgF under Visible-Light Irradiation. *ACS Catal.* **9**, 6335-6341 (2019).
73. C. Gao *et al.*, Heterogeneous Single-Atom Photocatalysts: Fundamentals and Applications. *Chem. Rev.* **120**, 12175–12216 (2020).
74. C. G. Silva, J. L. Faria, Photocatalytic oxidation of benzene derivatives in aqueous suspensions: Synergic effect induced by the introduction of carbon nanotubes in a TiO2 matrix. *Appl. Catal. B* **101**, 81-89 (2010).
75. D. Tsukamoto *et al.*, Selective Photocatalytic Oxidation of Alcohols to Aldehydes in Water by TiO2 Partially Coated with WO3. *Chem. Eur. J.* **17**, 9816-9824 (2011).
76. D. Yang *et al.*, Enhancing Photoactivity of TiO2(B)/Anatase Core–Shell Nanofibers by Selectively Doping Cerium Ions into the TiO2(B) Core. *Chem. Eur. J.* **19**, 5113-5119 (2013).
77. P. Zhang, Y. Liu, B. Tian, Y. Luo, J. Zhang, Synthesis of core-shell structured CdS@CeO2 and CdS@TiO2 composites and comparison of their photocatalytic activities for the selective oxidation of benzyl alcohol to benzaldehyde. *Catal. Today* **281**, 181-188 (2017).
78. J. He *et al.*, Facile fabrication of novel Cd3(C3N3S3)2/CdS porous composites and their photocatalytic performance for toluene selective oxidation under visible light irradiation. *Appl. Catal. B* **233**, 243-249 (2018).
79. Y.-H. Li, F. Zhang, Y. Chen, J.-Y. Li, Y.-J. Xu, Photoredox-catalyzed biomass intermediate conversion integrated with H2 production over Ti3C2Tx/CdS composites. *Green Chem.* **22**, 163-169 (2020).
80. H. Wang *et al.*, Covalent organic framework photocatalysts: structures and applications. *Chem. Soc. Rev.* **49**, 4135-4165 (2020).

81. Z. Liu *et al.*, A hydrophilic covalent organic framework for photocatalytic oxidation of benzylamine in water. *ChemComm* **56**, 766-769 (2020).
82. G. Lu *et al.*, Covalently integrated core-shell MOF@COF hybrids as efficient visible-light-driven photocatalysts for selective oxidation of alcohols. *J. Energy Chem.* **43**, 8-15 (2020).
83. N. Zhang *et al.*, Oxide Defect Engineering Enables to Couple Solar Energy into Oxygen Activation. *J. Am. Chem. Soc.* **138**, 8928-8935 (2016).
84. H. Wang *et al.*, Boosting Hot-Electron Generation: Exciton Dissociation at the Order–Disorder Interfaces in Polymeric Photocatalysts. *J. Am. Chem. Soc.* **139**, 2468-2473 (2017).
85. L. Zhang *et al.*, Solar-Light-Driven Pure Water Splitting with Ultrathin BiOCl Nanosheets. *Eur. J. Chem.* **21**, 18089-18094 (2015).
86. H. Huang *et al.*, Subsurface Defect Engineering in Single-Unit-Cell Bi2WO6 Monolayers Boosts Solar-Driven Photocatalytic Performance. *ACS Catal.* **10**, 1439-1443 (2020).
87. J. Ding *et al.*, Nitrogen vacancy engineered graphitic C3N4-based polymers for photocatalytic oxidation of aromatic alcohols to aldehydes. *Appl. Catal. B* **221**, 626-634 (2018).
88. J. Li *et al.*, Photocatalytic selective oxidation of benzene to phenol in water over layered double hydroxide: A thermodynamic and kinetic perspective. *Chem. Eng. J.* **388**, 124248 (2020).
89. J. Chen *et al.*, Ultrathin HNb3O8 nanosheets with oxygen vacancies for enhanced photocatalytic oxidation of amines under visible light irradiation. *J. Phys. Chem. A* **7**, 5493-5503 (2019).
90. L. Guo *et al.*, Ultrafine Au nanoparticles anchored on Bi2MoO6 with abundant surface oxygen vacancies for efficient oxygen molecule activation. *Catal. Sci. Technol.* **9**, 3193-3202 (2019).
91. Y. Shiraishi, N. Saito, T. Hirai, Adsorption-Driven Photocatalytic Activity of Mesoporous Titanium Dioxide. *J. Am. Chem. Soc.* **127**, 12820-12822 (2005).
92. Y. Shiraishi, D. Tsukamoto, T. Hirai, Selective Photocatalytic Transformations on Microporous Titanosilicate ETS-10 Driven by Size and Polarity of Molecules. *Langmuir* **24**, 12658-12663 (2008).
93. Y. Zhang, N. Zhang, Z.-R. Tang, Y.-J. Xu, Transforming CdS into an efficient visible light photocatalyst for selective oxidation of saturated primary C–H bonds under ambient conditions. *Chem. Sci.* **3**, 2812-2822 (2012).
94. Y. Wu *et al.*, Well-defined BiOCl colloidal ultrathin nanosheets: synthesis, characterization, and application in photocatalytic aerobic oxidation of secondary amines. *Chem. Sci.* **6**, 1873-1878 (2015).
95. H. Wang *et al.*, Optically Switchable Photocatalysis in Ultrathin Black Phosphorus Nanosheets. *J. Am. Chem. Soc.* **140**, 3474-3480 (2018).
96. W. Ren *et al.*, Optimizing the crystallization process of conjugated polymer photocatalysts to promote electron transfer and molecular oxygen activation. *J. Catal.* **389**, 636-645 (2020).
97. V. Augugliaro *et al.*, Oxidation of Aromatic Alcohols in Irradiated Aqueous Suspensions of Commercial and Home-Prepared Rutile TiO2: A Selectivity Study. *Chem. Eur. J.* **14**, 4640-4646 (2008).

98. A. R. Almeida, J. T. Carneiro, J. A. Moulijn, G. Mul, Improved performance of TiO2 in the selective photo-catalytic oxidation of cyclohexane by increasing the rate of desorption through surface silylation. *J. Catal.* **273**, 116-124 (2010).
99. Q. Wang, M. Zhang, C. Chen, W. Ma, J. Zhao, Photocatalytic Aerobic Oxidation of Alcohols on TiO2: The Acceleration Effect of a Brønsted Acid. *Angew. Chem. Int. Ed.* **49**, 7976-7979 (2010).
100. K. Tamai *et al.*, Visible-Light Selective Photooxidation of Aromatic Hydrocarbons via Ligand-to-Metal Charge Transfer Transition on Nb2O5. *J. Phys. Chem. C* **121**, 22854-22861 (2017).
101. H. Wang *et al.*, Enhanced Singlet Oxygen Generation in Oxidized Graphitic Carbon Nitride for Organic Synthesis. *Adv. Mater.* **28**, 6940-6945 (2016).
102. D. Zhang *et al.*, Promoting effect of cyano groups attached on g-C3N4 nanosheets towards molecular oxygen activation for visible light-driven aerobic coupling of amines to imines. *J. Catal.* **366**, 237-244 (2018).
103. B. Ravel, M. Newville, ATHENA, ARTEMIS, HEPHAESTUS: data analysis for X-ray absorption spectroscopy using IFEFFIT. *J. Synchrotron Radiat.* **12**, 537-541 (2005).
104. C.-H. Zhou, J. N. Beltramini, Y.-X. Fan, G. Q. Lu, Chemoselective catalytic conversion of glycerol as a biorenewable source to valuable commodity chemicals. *Chem. Soc. Rev.* **37**, 527-549 (2008).
105. K. E. Sanwald, T. F. Berto, W. Eisenreich, O. Y. Gutiérrez, J. A. Lercher, Catalytic routes and oxidation mechanisms in photoreforming of polyols. *J. Catal.* **344**, 806-816 (2016).
106. Y. Wan, J.-M. Lee, Toward Value-Added Dicarboxylic Acids from Biomass Derivatives via Thermocatalytic Conversion. *ACS Catal.* **11**, 2524-2560 (2021).
107. S.-H. Shi, Y. Liang, N. Jiao, Electrochemical Oxidation Induced Selective C–C Bond Cleavage. *Chem. Rev.* **121**, 485-505 (2021).
108. J. J. Bozell, G. R. Petersen, Technology development for the production of biobased products from biorefinery carbohydrates—the US Department of Energy's "Top 10" revisited. *Green Chem.* **12**, 539 (2010).
109. L. Xiong, J. Tang, Strategies and Challenges on Selectivity of Photocatalytic Oxidation of Organic Substances. *Adv. Energy Mater.* **11**, 2003216 (2021).
110. R. Chong *et al.*, Selective photocatalytic conversion of glycerol to hydroxyacetaldehyde in aqueous solution on facet tuned TiO2-based catalysts. *Chem Commun* **50**, 165-167 (2014).
111. X. Jin *et al.*, Photocatalytic CC bond cleavage in ethylene glycol on TiO2: A molecular level picture and the effect of metal nanoparticles. *J. Catal.* **354**, 37-45 (2017).
112. C. Li *et al.*, In-situ probing photocatalytic CC bond cleavage in ethylene glycol under ambient conditions and the effect of metal cocatalyst. *J. Catal.* **365**, 313-319 (2018).
113. V. Augugliaro *et al.*, Partial photocatalytic oxidation of glycerol in TiO2 water suspensions. *Catal Today* **151**, 21-28 (2010).
114. S. Yurdakal, G. Palmisano, V. Loddo, V. Augugliaro, L. Palmisano, Nanostructured Rutile TiO2 for Selective Photocatalytic Oxidation of

Aromatic Alcohols to Aldehydes in Water. *J. Am. Chem. Soc.* **130**, 1568-1569 (2008).
115. Z.-H. Xue, D. Luan, H. Zhang, X. W. Lou, Single-atom catalysts for photocatalytic energy conversion. *Joule*, (2022).
116. M. Xiao *et al.*, Molten-Salt-Mediated Synthesis of an Atomic Nickel Co-catalyst on TiO2 for Improved Photocatalytic H2 Evolution. *Angew. Chem., Int. Ed.* **59**, 7230-7234 (2020).
117. S. Shen *et al.*, Titanium dioxide nanostructures for photoelectrochemical applications. *Prog. Mater. Sci.* **98**, 299-385 (2018).
118. C. Zhao *et al.*, Solid-Diffusion Synthesis of Single-Atom Catalysts Directly from Bulk Metal for Efficient CO2 Reduction. *Joule* **3**, 584-594 (2019).
119. C. A. Tolman, W. M. Riggs, W. J. Linn, C. M. King, R. C. Wendt, Electron spectroscopy for chemical analysis of nickel compounds. *Inorg. Chem.* **12**, 2770-2778 (1973).
120. H. W. Nesbitt, D. Legrand, G. M. Bancroft, Interpretation of Ni2p XPS spectra of Ni conductors and Ni insulators. *Phys. Chem. Miner.* **27**, 357-366 (2000).
121. Y. S. Chen *et al.*, Microscopic mechanism for unipolar resistive switching behaviour of nickel oxides. *J. Phys. D: Appl. Phys.* **45**, 065303 (2012).
122. H. Qi *et al.*, Highly selective and robust single-atom catalyst Ru1/NC for reductive amination of aldehydes/ketones. *Nat. Commun.* **12**, 3295 (2021).
123. W. Liu *et al.*, A Durable Nickel Single-Atom Catalyst for Hydrogenation Reactions and Cellulose Valorization under Harsh Conditions. *Angew. Chem., Int. Ed.* **57**, 7071-7075 (2018).
124. W. Ren *et al.*, Electronic Regulation of Nickel Single Atoms by Confined Nickel Nanoparticles for Energy-Efficient CO2 Electroreduction. *Angew. Chem., Int. Ed.* **61**, e202203335 (2022).
125. Z. Wang *et al.*, Understanding the Roles of Oxygen Vacancies in Hematite-Based Photoelectrochemical Processes. *Angew. Chem., Int. Ed.* **58**, 1030-1034 (2019).
126. P. Doggali *et al.*, Combustion of volatile organic compounds over Cu–Mn based mixed oxide type catalysts supported on mesoporous Al2O3, TiO2 and ZrO2. *J. Mol. Catal. A Chem.* **358**, 23-30 (2012).
127. J. M. McKay, V. E. Henrich, Summary Abstract: Adsorption and interaction of O2, H2O, and CO on the NiO(100) surface. *J. Vac. Sci. Technol. A* **5**, 722-723 (1987).
128. H. Gu *et al.*, Adjacent single-atom irons boosting molecular oxygen activation on MnO2. *Nat. Commun.* **12**, 5422 (2021).
129. W. Gu *et al.*, Modulating Oxygen Reduction Behaviors on Nickel Single-Atom Catalysts to Probe the Electrochemiluminescence Mechanism at the Atomic Level. *Anal. Chem.* **93**, 8663-8670 (2021).
130. M. Setvín *et al.*, Reaction of O2 with Subsurface Oxygen Vacancies on TiO2 Anatase (101). *Science* **341**, 988-991 (2013).
131. P. Krishnan *et al.*, Characterization of photocatalytic TiO(2) powder under varied environments using near ambient pressure X-ray photoelectron spectroscopy. *Sci Rep* **7**, 43298 (2017).

132. M. E. Simonsen, Z. Li, E. G. Søgaard, Influence of the OH groups on the photocatalytic activity and photoinduced hydrophilicity of microwave assisted sol–gel TiO2 film. *Appl. Surf. Sci.* **255**, 8054-8062 (2009).
133. D. Irwin Michael, D. B. Buchholz, W. Hains Alexander, P. H. Chang Robert, J. Marks Tobin, p-Type semiconducting nickel oxide as an efficiency-enhancing anode interfacial layer in polymer bulk-heterojunction solar cells. *PNAS* **105**, 2783-2787 (2008).
134. M. Wang *et al.*, TiO2/NiO hybrid shells: p–n junction photocatalysts with enhanced activity under visible light. *J Mater Chem A* **3**, 20727-20735 (2015).
135. C.-J. Chen, C.-H. Liao, K.-C. Hsu, Y.-T. Wu, J. C. S. Wu, P–N junction mechanism on improved NiO/TiO2 photocatalyst. *Catal. Commun.* **12**, 1307-1310 (2011).
136. Q. Jin, T. Ikeda, M. Fujishima, H. Tada, Nickel(ii) oxide surface-modified titanium(iv) dioxide as a visible-light-active photocatalyst. *Chem Commun* **47**, 8814-8816 (2011).
137. Z. Babaei, A. Najafi Chermahini, M. Dinari, Glycerol adsorption and mechanism of dehydration to acrolein over TiO2 surface: A density functional theory study. *J. Colloid Interface Sci.* **563**, 1-7 (2020).
138. N. Tasinato, G. Ceselin, P. Stoppa, A. Pietropolli Charmet, S. Giorgianni, A Bit of Sugar on TiO2: Quantum Chemical Insights on the Interfacial Interaction of Glycolaldehyde over Titanium Dioxide. *J. Phys. Chem. C* **122**, 6041-6051 (2018).
139. P. Yang *et al.*, Insight into the Role of Unsaturated Coordination O2c-Ti5c-O2c Sites on Selective Glycerol Oxidation over AuPt/TiO2 Catalysts. *ACS Catal.* **9**, 188-199 (2019).
140. J. Lei, X. Duan, G. Qian, X. Zhou, D. Chen, Size Effects of Pt Nanoparticles Supported on Carbon Nanotubes for Selective Oxidation of Glycerol in a Base-Free Condition. *Ind. Eng. Chem.* **53**, 16309-16315 (2014).
141. C. Xu, Y. Du, C. Li, J. Yang, G. Yang, Insight into effect of acid/base nature of supports on selectivity of glycerol oxidation over supported Au-Pt bimetallic catalysts. *Appl. Catal. B* **164**, 334-343 (2015).
142. S. E. Davis, M. S. Ide, R. J. Davis, Selective oxidation of alcohols and aldehydes over supported metal nanoparticles. *Green Chem.* **15**, 17-45 (2013).
143. W. C. Ketchie, M. Murayama, R. J. Davis, Promotional effect of hydroxyl on the aqueous phase oxidation of carbon monoxide and glycerol over supported Au catalysts. *Top Catal.* **44**, 307-317 (2007).
144. A. Villa *et al.*, Tailoring the selectivity of glycerol oxidation by tuning the acid–base properties of Au catalysts. *Catal. Sci. Technol.* **5**, 1126-1132 (2015).
145. Y. Shen *et al.*, Promotion Mechanisms of Au Supported on TiO2 in Thermal- and Photocatalytic Glycerol Conversion. *J. Phys. Chem. C* **123**, 19734-19741 (2019).
146. L. Abis, N. Dimitritatos, M. Sankar, S. J. Freakley, G. J. Hutchings, Plasmonic oxidation of glycerol using AuPd/TiO2 catalysts. *Catal. Sci. Technol.* **9**, 5686-5691 (2019).
147. G. Dodekatos, H. Tüysüz, Plasmonic Au/TiO2 nanostructures for glycerol oxidation. *Catal. Sci. Technol.* **6**, 7307-7315 (2016).

148. V. Maurino *et al.*, in *J. Adv. Oxid. Technol.* (2008), vol. 11, pp. 184.
149. J. Payormhorm, R. Idem, Synthesis of C-doped TiO2 by sol-microwave method for photocatalytic conversion of glycerol to value-added chemicals under visible light. *Appl. Catal. A* **590**, 117362 (2020).
150. J. Yu *et al.*, Glyceraldehyde production by photocatalytic oxidation of glycerol on WO3-based materials. *Appl. Catal. B* **299**, 120616 (2021).
151. H. Cheng, J. Cheng, L. Wang, H. Xu, Reaction Pathways toward Sustainable Photosynthesis of Hydrogen Peroxide by Polymer Photocatalysts. *Chem. Mater.* **34**, 4259-4273 (2022).
152. M. Teranishi, S.-i. Naya, H. Tada, In Situ Liquid Phase Synthesis of Hydrogen Peroxide from Molecular Oxygen Using Gold Nanoparticle-Loaded Titanium(IV) Dioxide Photocatalyst. *J. Am. Chem. Soc.* **132**, 7850-7851 (2010).
153. M. R. Miah, T. Ohsaka, Cathodic Detection of H2O2 Using Iodide-Modified Gold Electrode in Alkaline Media. *Anal. Chem.* **78**, 1200-1205 (2006).
154. T. Hirakawa, K. Yawata, Y. Nosaka, Photocatalytic reactivity for O2− and OH radical formation in anatase and rutile TiO2 suspension as the effect of H2O2 addition. *Appl. Catal. A* **325**, 105-111 (2007).
155. A. J. Hoffman, E. R. Carraway, M. R. Hoffmann, Photocatalytic Production of H2O2 and Organic Peroxides on Quantum-Sized Semiconductor Colloids. *Environ. Sci. Technol.* **28**, 776-785 (1994).
156. K. Sahel *et al.*, Hydrogen peroxide and photocatalysis. *Appl. Catal. B* **188**, 106-112 (2016).
157. E. S. Jang, J. H. Won, S. J. Hwang, J. H. Choy, Fine Tuning of the Face Orientation of ZnO Crystals to Optimize Their Photocatalytic Activity. *Adv. Mater.* **18**, 3309-3312 (2006).
158. Z. Jiang, Y. Zhang, L. Zhang, B. Cheng, L. Wang, Effect of calcination temperatures on photocatalytic H2O2-production activity of ZnO nanorods. *Chinese J. Catal.* **43**, 226-233 (2022).
159. B. Liu *et al.*, Hierarchically Porous ZnO/g-C3N4 S-Scheme Heterojunction Photocatalyst for Efficient H2O2 Production. *Langmuir* **37**, 14114-14124 (2021).
160. X. Geng *et al.*, H2O2 production and in situ sterilization over a ZnO/g-C3N4 heterojunction photocatalyst. *Chem Eng J* **420**, 129722 (2021).
161. Y. Zhang *et al.*, ZnO/COF S-scheme heterojunction for improved photocatalytic H2O2 production performance. *Chem Eng J* **444**, 136584 (2022).
162. N. A. Hermes, A. Corsetti, M. A. Lansarin, Comparative Study on the Photocatalytic Oxidation of Glycerol Using ZnO and TiO2. *Chem. Lett.* **43**, 143-145 (2014).
163. B. Pal, M. Sharon, Photocatalytic formation of hydrogen peroxide over highly porous illuminated ZnO and TiO2thin film. *Toxicol. Environ. Chem.* **78**, 233-241 (2000).
164. L. Wang *et al.*, Inorganic Metal-Oxide Photocatalyst for H2O2 Production. *Small* **18**, 2104561 (2022).
165. R. Kuladeep, L. Jyothi, K. S. Alee, K. L. N. Deepak, D. N. Rao, Laser-assisted synthesis of Au-Ag alloy nanoparticles with tunable surface plasmon resonance frequency. *Opt. Mater. Express* **2**, 161-172 (2012).

166. L. Luo *et al.*, Binary Au–Cu Reaction Sites Decorated ZnO for Selective Methane Oxidation to C1 Oxygenates with Nearly 100% Selectivity at Room Temperature. *J. Am. Chem. Soc.* (2021).
167. N. J. Firet *et al.*, Operando EXAFS study reveals presence of oxygen in oxide-derived silver catalysts for electrochemical CO2 reduction. *J Mater Chem A* **7**, 2597-2607 (2019).
168. Y. Liang, S. Wicker, X. Wang, E. S. Erichsen, F. Fu, Organozinc Precursor-Derived Crystalline ZnO Nanoparticles: Synthesis, Characterization and Their Spectroscopic Properties. *Nanomaterials (Basel)*. 2018 (10.3390/nano8010022).
169. L. Luo *et al.*, Selective Photoelectrocatalytic Glycerol Oxidation to Dihydroxyacetone via Enhanced Middle Hydroxyl Adsorption over a Bi2O3-Incorporated Catalyst. *J. Am. Chem. Soc.* **144**, 7720-7730 (2022).
170. S. T. Wu, Q. M. She, R. Tesser, M. D. Serio, C. H. Zhou, Catalytic glycerol dehydration-oxidation to acrylic acid. *Catal. Rev*. 1-43 (2020).
171. D. Liu *et al.*, Selective photoelectrochemical oxidation of glycerol to high value-added dihydroxyacetone. *Nat. Commu.* **10**, 1779 (2019).
172. A. Behr, J. Eilting, K. Irawadi, J. Leschinski, F. Lindner, Improved utilisation of renewable resources: New important derivatives of glycerol. *Green Chem.* **10**, 13-30 (2008).
173. R. Ciriminna, G. Palmisano, C. D. Pina, M. Rossi, M. Pagliaro, One-pot electrocatalytic oxidation of glycerol to DHA. *Tetrahedron Lett.* **47**, 6993-6995 (2006).
174. X. Ning *et al.*, Promoting role of bismuth and antimony on Pt catalysts for the selective oxidation of glycerol to dihydroxyacetone. *J. Catal.* **335**, 95-104 (2016).
175. Y. Kwon, Y. Birdja, I. Spanos, P. Rodriguez, M. T. M. Koper, Highly Selective Electro-Oxidation of Glycerol to Dihydroxyacetone on Platinum in the Presence of Bismuth. *ACS Catal.* **2**, 759-764 (2012).
176. S. Schünemann, G. Dodekatos, H. Tüysüz, Mesoporous Silica Supported Au and AuCu Nanoparticles for Surface Plasmon Driven Glycerol Oxidation. *Chem. Mater.* **27**, 7743-7750 (2015).
177. A. C. Garcia *et al.*, Strong Impact of Platinum Surface Structure on Primary and Secondary Alcohol Oxidation during Electro-Oxidation of Glycerol. *ACS Catal.* **6**, 4491-4500 (2016).
178. P. Panagiotopoulou, E. E. Karamerou, D. I. Kondarides, Kinetics and mechanism of glycerol photo-oxidation and photo-reforming reactions in aqueous TiO2 and Pt/TiO2 suspensions. *Catal Today* **209**, 91-98 (2013).
179. M. de Oliveira Melo, L. A. Silva, Visible light-induced hydrogen production from glycerol aqueous solution on hybrid Pt–CdS–TiO2 photocatalysts. *J. Photochem. Photobiol. A* **226**, 36-41 (2011).
180. X. Liu *et al.*, Synthesis of a WO3 photocatalyst with high photocatalytic activity and stability using synergetic internal Fe3+ doping and superficial Pt loading for ethylene degradation under visible-light irradiation. *Catal. Sci. Technol.* **9**, 652-658 (2019).
181. M. Stelmachowski, M. Marchwicka, E. Grabowska, M. Diak, The Photocatalytic Conversion of (Biodiesel Derived) Glycerol to Hydrogen

- A Short Review and Preliminary Experimental Results Part 1: A Review. **17**, 167-178 (2014).
182. Z. Chen *et al.*, Hierarchical Nanostructured WO3 with Biomimetic Proton Channels and Mixed Ionic-Electronic Conductivity for Electrochemical Energy Storage. *Nano Lett.* **15**, 6802-6808 (2015).
183. Z. H. Zhang, P. Wang, Highly stable copper oxide composite as an effective photocathode for water splitting via a facile electrochemical synthesis strategy. *J Mater Chem* **22**, 2456-2464 (2012).
184. L. Xiong *et al.*, Highly Selective Transformation of Biomass Derivatives to Valuable Chemicals by Single-Atom Photocatalyst Ni/TiO2. *Adv. Mater.* **n/a**, 2209646 (2023).
185. L. Yang, Y. Jiang, Z. Zhu, Z. Hou, Selective oxidation of glycerol over different shaped WO3 supported Pt NPs. *Mol. Catal.* 111545 (2021).
186. Y. Zhang *et al.*, Single-atom Cu anchored catalysts for photocatalytic renewable H2 production with a quantum efficiency of 56%. *Nat. Commu.* **13**, 58 (2022).
187. C.-J. Chen, D.-H. Chen, Preparation and near-infrared photothermal conversion property of cesium tungsten oxide nanoparticles. *Nanoscale Res. Lett.* **8**, 57 (2013).
188. Y. Liu *et al.*, An in situ assembled WO3–TiO2 vertical heterojunction for enhanced Z-scheme photocatalytic activity. *Nanoscale* **12**, 8775-8784 (2020).
189. P. Pędziwiatr, F. Mikołajczyk, D. Zawadzki, K. Mikołajczyk, A. Bedka, Decomposition of hydrogen peroxide - kinetics and review of chosen catalysts. *Acta Innov*. 45-52 (2018).
190. I. M. Pateli, A. P. Abbott, G. R. T. Jenkin, J. M. Hartley, Electrochemical oxidation as alternative for dissolution of metal oxides in deep eutectic solvents. *Green Chem.* **22**, 8360-8368 (2020).
191. M. El-Roz, M. Kus, P. Cool, F. Thibault-Starzyk, New Operando IR Technique to Study the Photocatalytic Activity and Selectivity of TiO2 Nanotubes in Air Purification: Influence of Temperature, UV Intensity, and VOC Concentration. *J. Phys. Chem. C* **116**, 13252-13263 (2012).